Nell'ambito della borsa di dottorato del

Programma Operativo Nazionale Ricerca e Innovazione 2014-2020

(CCI 2014IT16M2OP005)

risorse FSE REACT-EU, Azione IV.5 “Dottorati su tematiche Green”

UNIVERSITA’ DEGLI STUDI DELL’AQUILA

Dipartimento di Scienze Fisiche e Chimiche

Curriculum in Chimica

Dottorato di Ricerca in

Scienze Fisiche e Chimiche

CICLO XXXVII

Con il contributo di

MIUR FONDI PON R&I FSE REACT-EU 2014-2020

Titolo

Development of functional membranes based on nanomaterials for sustainable water-energy nexus: advancing solar radiation-promoted seawater distillation and mineral recovery from the sea

SSD – CHIM/07

Dottoranda

Jessica Occhiuzzi

Coordinatore del Corso

Prof. Massimiliano Aschi

Tutor

Prof. Antonio Politano

Prof. Efrem Curcio

a.a. 2024/2025

Table of contents

Chapter 1 5

Introduction 5

Chapter 2 23

Dimethyl 2-Methylglutarate (Iris): A Green Platform for Efficient Liquid-Phase Exfoliation of 2D Materials Keywords: 2D Materials; Green Chemistry; Iris; Liquid-phase Exfoliations 23

Chapter 3 40

The Quest for Green Solvents for the Sustainable Production of Nanosheets of Two-Dimensional (2D) Materials, a Key Issue in the Roadmap for the Ecology Transition in the Flatland Keywords: Cyrene; Polarclean; Iris; green chemistry; 2D materials; liquid-phase exfoliation 40

Chapter 4 59

NiSe and CoSe Topological Nodal-Line Semimetals: A Sustainable Platform for Efficient Thermoplasmonics and Solar-Driven Photothermal Membrane Distillation Keywords: Solar membrane distillation; thermoplasmonics; topological materials; optical anisotropy; nodal-line semimetals 59

Chapter 5 79

Lithium recovery through WS_2 nanofillers-promoted solar photothermal membrane crystallization of LiCl Keywords: Photothermal membrane crystallization; Photothermal nanosheets; Lithium recovery; Water-energy-raw materials nexus; Energy transition 79

Chapter 6 104

Green photocatalytic mixed matrix membranes for simultaneous arsenic photo-oxidation and water recovery via membrane distillation Keywords: Arsenic; Green Solvent; Membrane Distillation; Photocatalytic Membranes; Photo-oxidation 104

Conclusions 131

List of publications 133

Acknowledgements 134

Abstract

The increasing pressure exerted by the climate crisis, combined with the ongoing expansion of human activities, has made the development of innovative technologies for the sustainable management of water and energy resources urgent. In this context, photothermal membranes integrated with advanced nanomaterials emerge as a promising response to challenges related to desalination, wastewater treatment, and the recovery of strategic resources such as lithium. This thesis explores the integration of two-dimensional materials, materials made up of individual atomic layers that impart extraordinary physical and chemical properties, such as high specific surface area, thermal conductivity and light absorption capacity, including WS2, NiSe, CoSe, TiO2, In_2Se_3, and InS, to improve the performance of membrane distillation (MD) and membrane crystallization (MCr) processes, while addressing the limitations of existing technologies.

The research focuses on improving the energy efficiency and sustainability of thermal separation processes. Membrane distillation, augmented by photothermal nanomaterials such as NiSe and CoSe, has shown a significant increase in efficiency by reducing thermal polarization and optimizing the use of solar energy. Experimental results indicate a 30% improvement in overall process efficiency, highlighting the crucial role of thermoplasmonic nanomaterials in overcoming the main limitations of this technology. Simultaneously, membrane crystallization was employed for the selective recovery of lithium from concentrated brines, with WS_2 integrated as a key nanofiller to improve selectivity and control crystal nucleation. This application holds strategic importance in supporting the energy transition, where lithium is an essential material.

A central aspect of this thesis is the development of a sustainable approach for the synthesis of two-dimensional (2D) nanomaterials by liquid exfoliation method. The use of dimethyl 2-methylglutarate (Rhodiasolv$^{(R)}$ Iris) as a green solvent makes it possible to produce high-quality nanosheets with reduced environmental impact, meeting the growing regulatory and industrial demands for sustainability. The liquid exfoliation method not only minimizes the use of toxic substances but also ensures high yield and optimal structural quality of the 2D materials. The resulting nanomaterials, including In_2Se_3 and InS, exhibited superior chemical and thermal stability, making them ideal for applications in complex operational environments.

Further research developments included the application of photothermal membranes for the treatment of industrial wastewater. Membranes enriched with TiO_2 exhibited effective capabilities in removing complex contaminants such as arsenic and other toxic substances. This approach combines advanced photocatalysis with membrane separation technologies, underscoring the potential of these membranes for water purification and environmental compliance. The overall results of this thesis demonstrate that the integration of advanced nanomaterials into photothermal

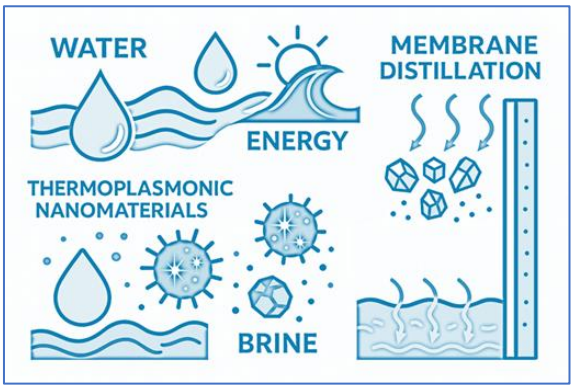
membranes offers scalable, sustainable, and efficient solutions to address some of the most pressing challenges in water and energy resource management. The proposed technologies not only represent significant improvement over traditional methods but also introduce new paradigms for the recovery of critical resources and the responsible management of wastewater. Looking ahead, the work emphasizes the need for further studies on optimizing fabrication techniques, ensuring sustainable industrial scalability, and expanding these technologies to new sectors, such as residual brine management and energy production from salinity gradients.

This thesis, therefore, not only provides a scientific response to current challenges but also lays the groundwork for industrial and environmental development aimed at a sustainable transition, offering innovative and responsible technological solutions for the future.

Chapter 1

Introduction

GRAPHICAL ABSTRACT



Contents

Abstract

1.1 The Global Energy Crisis and Water Scarcity

1.2 Transition Towards Sustainable Energy Systems

1.3 Challenges in Water Resource Management

1.4 Blue energy generation from brines

1.5 Trends and Innovations in the Desalination Industry

1.6 The Synergy Between Renewable Energy and Desalination

1.7 Brine: Transforming Waste into a Resource

1.8 Membrane Distillation and Crystallization: a dual-purpose approach

1.9 Power generation with Photothermal Nanomaterials

1.10 Goals and scope of the PhD Project

References

Abstract

One of the primary objectives of this PhD thesis was to produce nanostructured functional membranes for water desalination, recovery of minerals from seawater and energy production through sunlight-driven membrane operations. Water vapour, produced from the evaporation of seawater or brackish water, permeates through hydrophobic and microporous polymeric membranes and is subsequently recondensed. This process not only yields clean water but also enables the recovery of salts and/or non-volatile compounds in the form of crystals in the retentate. To increase both the productivity and efficiency of the purification processes, the chemical-physical properties of innovative 2D materials with high photothermal efficiency, confined within polymer matrices, will be exploited. These advanced polymer nanocomposites will be used in membrane distillation (MD) and membrane crystallization (MCr) processes, which are considered 'green' technologies due to their ability to produce clean water and recover mineral salts from seawater.

This chapter reviews the global need for sustainable and renewable energy sources and introduces the basic concepts and principles of salinity gradient energy, membrane desalination processes and modern brine assessment. It then outlines the purpose and structure of this thesis.

1.1 The Global Energy Crisis and Water Scarcity

Water and energy are two of the most critical environmental challenges, deeply interconnected and essential for ensuring a sustainable and secure future for humanity. Given the rising and ongoing demand for water and energy, it is crucial to identify solutions that not only promote sustainability but also respect the environment [1]. The outdated linear economy model, traditionally based on the 'take-make-dispose' system, must be replaced by a circular economy that focuses on reusing and enhancing materials typically discarded during industrial processes.

Regrettably, in recent decades, the availability of drinking water in many countries across the Euro-Mediterranean region has significantly diminished. This unwanted water shortage has been driven by factors such as climate change, the desertification of vast agricultural and forested areas, and the excessive use of water in industrial and agricultural activities. In addition to these physical causes, the impacts of geopolitical instability, population growth, and migration due to economic and environmental pressures are also noteworthy [2][3].

To meet the growing demand for freshwater, seawater desalination has emerged as a viable and increasingly adopted solution, with global capacity reaching 100 million cubic meters of freshwater production per day [4].

The seawater desalination industry is currently dominated by the 'Reverse Osmosis' (SWRO, SeaWater Reverse Osmosis) process. In this technique, solvent molecules (i.e., water) move from the more concentrated solution to the less concentrated one- through a semi-permeable membrane by applying pressure that exceeds the osmotic pressure of the saline solution. As a result, SWRO requires mechanical work to overcome this osmotic pressure [5]. Most SWRO plants have a specific energy consumption of 3-4 kWh/m^3, and the cost of producing drinking water is around \$0.5/m^3, which is significantly lower than conventional thermal evaporation methods. However, the theoretical energy consumption limit for producing 1 m^3 of freshwater from 2 m^3 of saline water is calculated at 1.1 kWh/m^3. Therefore, technological innovations must be introduced to enhance the energy efficiency of the desalination process. Additionally, the CO_2 emissions associated with the thermoelectric energy required for SWRO operations are estimated to be 1.4-1.8 kg/m^3.

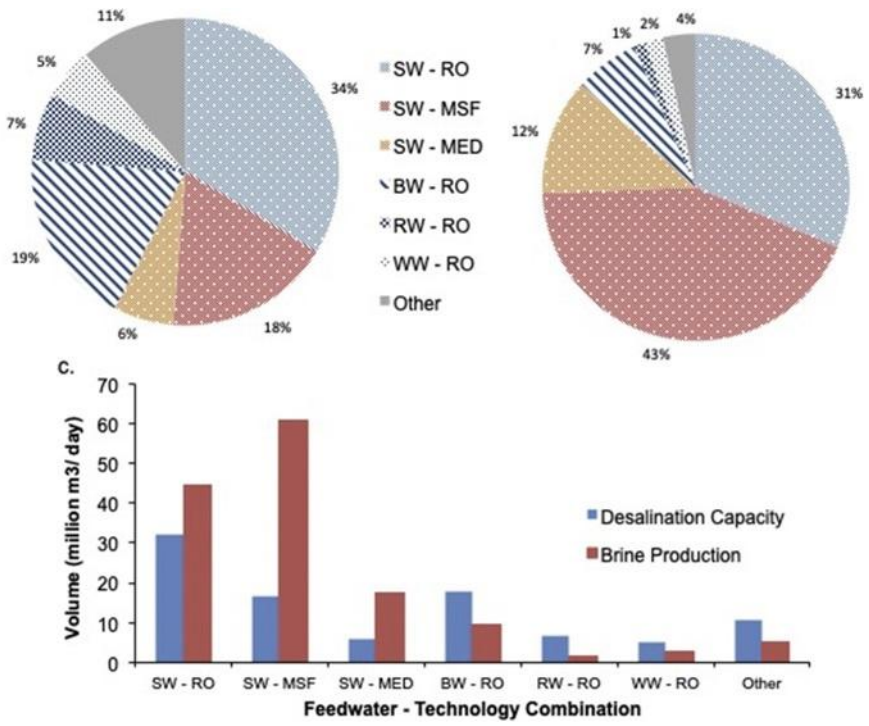


Figure 1.1. *Major desalination feedwater-technology combinations by (a) global share in the desalinated water production (%), (b) global share in brine production (%) and (c) total desalination capacity and volume of brine produced (million m^3/day).* [6]

Additionally, the recovery rate of SWRO is restricted to 50%, due to the effects of concentration polarization and osmotic polarization, which reduce the process's efficiency and generate a large

volume of brine (hyper-saline solution) as a by-product. This brine is typically discharged directly into the sea, causing harmful impacts on coastal and marine ecosystems.

It has been determined that access to drinking water through SWRO plants at affordable prices is largely limited to communities located along the coast with reliable access to fossil fuel energy [7].

Emerging membrane technologies have the potential to open new pathways toward a more sustainable desalination industry by treating brine in line with the principles of the circular economy. In this context, reverse electrodialysis (RED) has been identified as a promising new electromembrane process capable of utilizing SWRO brine to generate renewable energy, thereby addressing the water-energy nexus. RED is a technology that relies on alternating anion and cation exchange membranes between two electrodes to generate electricity from salinity gradients. It takes advantage of the salinity gradient between two solutions with different concentrations (e.g., brine and seawater) to produce what is known as 'Blue Energy' or Salinity Gradient Power (SGP), thus reducing the specific energy consumption of seawater desalination.

Membrane Distillation (MD) has also gained attention as a complementary technology to SWRO. MD can treat SWRO brine and increase the overall water recovery rate above 80%, because it is not affected by the high osmotic pressures that limit SWRO performance [8]. Notably, extending MD operations beyond the solubility limits of dissolved salts, referred to as Membrane Crystallization (MCr), has proven to be effective in recovering valuable minerals from brine.

However, the practical implementation of both MD and MCr has been hindered by their low thermal efficiency, which compromises their energy viability. The recent introduction of thermoplasmonics into membrane technologies has transformed the approach to heat harvesting in MD/MCr, enabling the use of artificial or natural radiation to drive these processes [9].

This approach relies on the in-situ light-to-heat conversion performed by noble metal nanoparticles integrated into or onto the membranes.

This shift toward thermoplasmonic membrane systems aligns with the broader goals of modernizing traditional desalination methods, minimizing waste, and fostering a circular economy [10].

1.2 Transition Towards Sustainable Energy Systems

The urgent need to reduce dependence on fossil fuels has accelerated the global transition toward sustainable energy systems. Governments and industries worldwide are increasingly adopting renewable energy sources such as solar, wind, and hydropower, driven by climate change concerns

and the depletion of traditional energy resources. In the context of desalination, integrating renewables into water treatment processes can significantly lower the carbon footprint while enhancing energy security.

Solar energy is particularly relevant here, given its abundance and compatibility with membrane-based processes like MD and MCr. Solar-driven desalination systems can operate in remote or off-grid locations, providing clean water to communities without reliable access to conventional energy infrastructure. Moreover, combining solar power with advanced membrane technologies offers the dual benefit of reducing greenhouse gas emissions and lowering operational costs over time, especially as solar panel and photothermal material technologies continue to improve in efficiency.

This shift toward renewable energy not only addresses global energy shortages but also aligns with the principle of the water-energy nexus, where water and energy solutions are interlinked to optimize resource use. By adopting sustainable energy systems for desalination, industries and governments can move closer to a circular economy model, minimize environmental impacts, and ensure the long-term viability of water supplies.

1.3 Challenges in Water Resource Management

In recent years, there has been a surge in global focus on water, the most basic and ubiquitous substance for humans. Referred to as "the new gold", water is now transforming economic paradigms due to: i) its essential role in sustaining life and supporting human activities; ii) the unsustainable and escalating demand, driven by population growth, agricultural intensification, industrial expansion, and inefficient usage practices; iii) the decreasing availability resulting from linear consumption patterns.

Both food and energy, key elements of human existence, are intrinsically linked to water: it is essential for agricultural cultivation and energy production [11]. Traditionally, seen as a common resource, the true significance of water has often been underestimated. Yet, in the 21st century, it has been redefined as an economic asset, becoming central to the policies of various governments. To underscore the gravity of the water crisis, more than one billion people currently lack access to safe drinking water, and 2.7 billion experience water scarcity for at least one month each year.

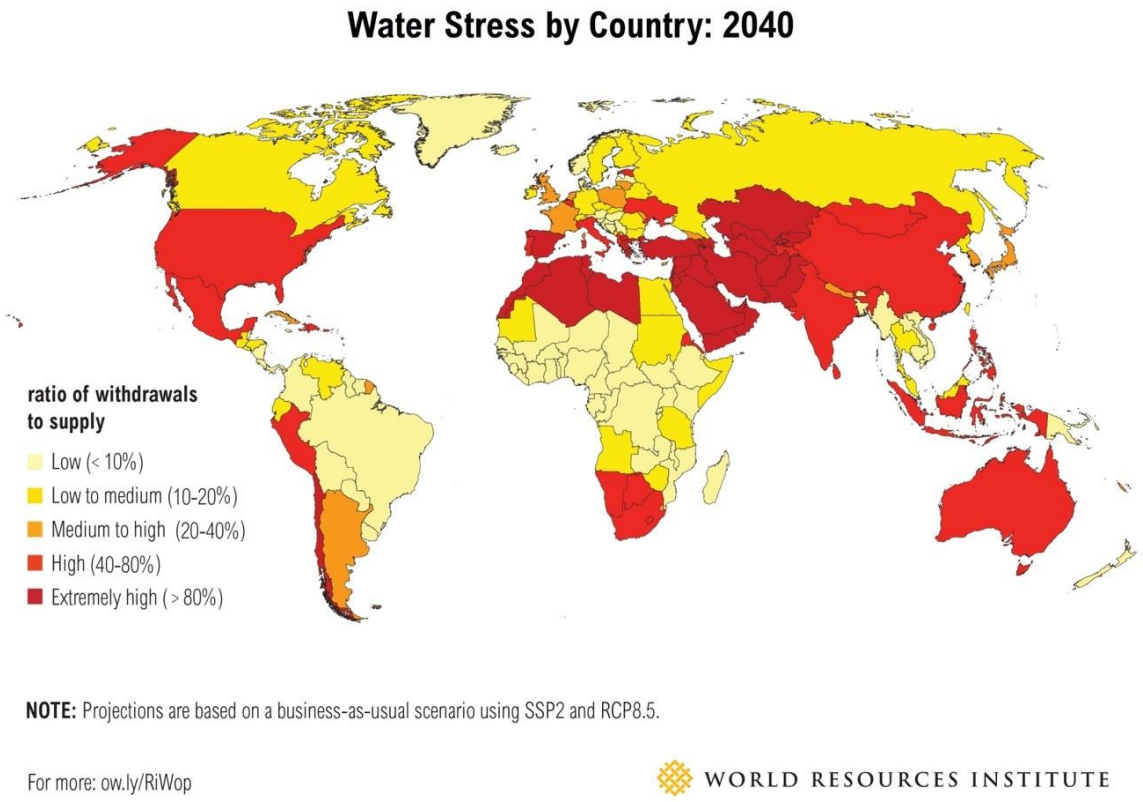


Figure 1.2. *Number of publications related to brine management from 2000 to 2020 [11 a]*

Amidst this challenging context, further complicated by the economic downturn triggered by the pandemic, it is imperative to strategically coordinate large-scale infrastructure investments with anti-pollution initiatives to improve both the quantity and quality of available water [12].

The world faces an urgent water shortage, prompting the search for alternatives that can compete with an economy that commodifies everything essential to human life [13]. Desalination plants and innovative technologies that make seawater potable could offer promising solutions. Achieving significant progress will depend on embracing technological advancements to develop and refine widespread desalination and recycling systems, thereby reducing costs through global implementation [14].

1.4 Blue energy generation from brines

Marine-derived energy is likely the most underutilized and least understood form of renewable energy. Its potential is vast, as seas and oceans cover 75% of the Earth's surface [15]. Various types of energy available in the sea can be converted: ocean currents, waves, tides, tidal currents,

the thermal gradient between the surface and the seabed, and salinity differences [16]. Different technological approaches have been employed to harness marine energy and convert it into electricity. Typically, these methods present lower environmental risks and generate fewer greenhouse gas emissions compared to conventional energy sources throughout their entire life cycle, from infrastructure construction to system installation, management, and maintenance [17]. Currently, it is projected that Blue Energy could meet 10% of the energy needs in EU countries by 2050. Additionally, the global Blue Energy market is anticipated to reach 337 GW of installed capacity by 2050, with one-third of this capacity located in Europe [18]. Within this context, energy production from saline gradients represents one of the most innovative and promising research areas in recent years [19]. Blue Energy is derived from the controlled mixing of aqueous solutions with different salinities, converting this into mechanical or electrochemical energy. Essentially, the flow of ions between streams with varying salinities, such as saltwater (high concentration) and treated wastewater or freshwater (lower concentration), can be harnessed to generate electricity [20]. The mixing process increases system entropy, leading to the dissipation of Gibbs free energy. Literature indicates that mixing seawater (0.513 M NaCl, 30 g/L) with river water (0.017 M NaCl, 1 g/L), each with a flow rate of 1 m^3/s, theoretically yields 1.39 MJ of energy. The amount of extractable energy increases significantly with the salinity of the solutions, making SWRO brines, which are concentrated seawater, particularly attractive [21].

Another notable advantage is the ability to produce energy continuously and reliably, unlike conventional renewable sources (solar, wind, wave, etc.), which are inherently intermittent and subject to hourly or seasonal variations [22].

The RED technology, which utilizes ion exchange membranes, represents a cutting-edge method for generating electricity from saline gradients. In a typical RED setup, cation exchange membranes (CEM) and anion exchange membranes (AEM) are alternately stacked and separated by spacers that form channels through which solutions of different concentrations flow. The orderly movement of ions driven by the concentration gradient causes the segregation of positive and negative charges, thus generating an electric potential [23].

While the prospects for the RED market are very promising, challenges such as the high costs associated with plant construction and management, as well as the difficulty in finding suitable production sites, must be considered [24].

1.5 Trends and innovations in the desalination industry

In recent years, the issue of freshwater scarcity has emerged as a critical concern across civil,

industrial, and agricultural sectors [25]. Currently, there are over 20,000 desalination plants worldwide, collectively producing around 90 million cubic meters of fresh water daily [26].

The Middle East leads this growth, with desalination increasing by up to 28%, while the United States is also seeing a 25% rise. In Europe, there are 2,352 desalination plants, with 84% utilizing Reverse Osmosis (RO) technology. Although only 8% of these plants are large-scale, they account for 69% of the total desalinated water produced in Europe. Spain is the leading European country in desalination (68%), grappling with a significant water crisis and heavily investing in a circular water economy. The remaining plants are primarily situated in Mediterranean countries (Italy 9%, Cyprus 8%, Malta 5%, Greece 3%), with some smaller plants in northern countries such as the UK, Netherlands, Denmark, and Germany, primarily serving industrial needs [27].

RO technology dominates the global desalination market, currently comprising 60% of large-scale installations. Despite its advantages over thermal processes, RO technology has several drawbacks, including high energy consumption, significant maintenance needs, and considerable wastewater production. Specifically, RO technology, while being the most economical and commercially available option, requires approximately 3-5 kWh per cubic meter of desalinated water. This is double the theoretical minimum energy requirement of 1.06 kWh/m^3, assuming a 50% recovery factor [28]. Moreover, the performance of RO processes is heavily dependent on the quality of the feed water and temperature.

The combination of high energy consumption and sensitivity to feedwater conditions significantly affects the cost of desalinated water, making it unaffordable for many developing countries. Conversely, countries such as Saudi Arabia, Kuwait, the United Arab Emirates, Qatar, Oman, Bahrain, Spain, Australia, and parts of North America have adopted RO technology [29]. A global challenge is to reduce the high costs associated with RO desalination, making it more accessible to emerging countries with scarce water resources.

It is also important to note that these desalination plants rely on fossil fuels, raising significant environmental and sustainability concerns. Current plants, with a desalination capacity exceeding 90 million cubic meters per day, represent about 6% of the global freshwater supply [30]. They consume over 850 million liters of fossil fuels annually [31], and this consumption will likely increase as more plants are built. Fluctuations in oil prices directly impact the energy costs of these plants [31]. Beyond economic implications, the heavy reliance on fossil fuels results in the emission of vast quantities of carbon dioxide (CO_2), contributing to air pollution, global warming, and ecosystem degradation. It is estimated that conventional thermal desalination processes emit between 1.5 and 2.9 kg of CO_2 per cubic meter of freshwater produced, depending on the energy source and plant efficiency.

In contrast, alternative technologies integrated with solar thermal energy or photovoltaic systems can significantly reduce or even eliminate direct CO_2 emissions.

Thus, transitioning to renewable-powered desalination not only addresses the economic vulnerability linked to fuel price volatility but also aligns with global climate goals by reducing greenhouse gas emissions and mitigating environmental harm.

This situation underscores the urgent need for more sustainable and energy-efficient technological solutions. Unfortunately, projected economic growth, population increase, rising sea levels, and climate change are expected to drive up the demand for freshwater, potentially hindering the sustainable development of coastal areas in industrialized, emerging, and developing nations [32][33].

1.6 The Synergy Between Renewable Energy and Desalination

Renewable energy sources, such as solar, wind, and hydropower, play a pivotal role in mitigating the effects of the global energy crisis. The integration of renewable energy sources with desalination technologies offers a pathway to reduce the environmental and economic costs of these processes. Solar energy has gained attention due to its abundance and potential to power desalination plants. By harnessing solar energy, the reliance on conventional fossil fuels can be significantly reduced, thereby lowering the environmental impact and improving the sustainability of desalination processes. Although the total energy demand of the process remains unchanged, replacing non-renewable energy sources with solar energy contributes to a more affordable and climate-friendly water production system.

Desalination processes predominantly rely on four main sources: seawater, which constitutes 67% of the feedstock; brackish water, making up 19%; river water at 8%; and wastewater, which contributes 6%. These desalination technologies can be broadly classified based on their separation mechanisms into two main categories: thermal desalination and membrane desalination.

Traditional thermal desalination techniques include multi-effect evaporation (MEE) and multi-effect distillation (MED), both of which involve the use of heat to evaporate water and subsequently condense it to remove salts. Vapor compression (VC) is another thermal method that relies on the compression of vapor to enhance the efficiency of evaporation and condensation processes. Solar desalination, which utilizes solar energy to heat water, is also part of the thermal desalination category.

In contrast, membrane-based desalination processes operate through the use of semi-permeable membranes to separate salts and other impurities from water. RO is the most commonly used

membrane technology, where water is forced through a membrane that filters out salts and other contaminants. Electrodialysis (ED) is another membrane-based technique that uses electrical currents to drive the movement of ions through ion-exchange membranes, thereby purifying the water [23].

Recently, membrane technologies have increasingly supplanted traditional thermal methods such as Multi-Effect Distillation (MED), Multi-Stage Flash (MSF), and Vapor Compression Distillation (VCD) in many regions of the world. This shift is largely attributed to the lower energy consumption associated with membrane processes. For example, membrane distillation (MD), when integrated with RO systems, offers notable energy savings. In addition to their energy efficiency, membrane technologies are favored for their compactness, lightweight design, and high productivity, which make them attractive options for future development.

In contrast, conventional thermal desalination techniques require significant amounts of energy to effectively separate salts from water. It is estimated that the current global desalination capacity consumes approximately 75.2 terawatt-hours (TWh) of energy each year. This level of energy consumption is not compatible with the principles of a circular economy, which emphasizes the importance of integrating sustainable and renewable energy sources. The economic rationale behind adopting renewable energy sources is compelling: while fossil fuels cost between $0.05 and $0.09 per kilowatt-hour (kWh), renewable energy sources such as geothermal, wind, and solar power are priced significantly lower, at $0.007, $0.05, and $0.05 to $0.09 per kWh, respectively [34].

The concept of green desalination, which involves utilizing renewable energy sources to drive desalination processes, is emerging as a promising approach for producing clean water and energy. As the costs of renewable energy technologies continue to decrease, green desalination is expected to become increasingly feasible compared to traditional fossil fuels. Recent advancements have introduced innovative processes such as Membrane Distillation (MD), Reverse Electrodialysis (RED), and Pressure Retarded Osmosis (PRO). These emerging technologies hold the potential to address the complex water-energy nexus and mitigate water scarcity issues in various regions around the globe. The hybridization of these technologies could offer effective solutions for the sustainable production of both water and energy, thereby contributing to global efforts to manage and conserve essential resources [35].

1.7 Brine: Transforming Waste into a Resource

Modern desalination processes generate a by-product known as "brine," which presents significant

challenges in terms of disposal costs and environmental consequences. Brine, a term used to describe the concentrated saline solution produced by these processes, results from treating salty or brackish water. This brine is typically discharged directly into the ocean [36]. For every 100 million cubic meters of fresh water produced, about 50 million cubic meters of this hypersaline brine is released. The exact amount can vary widely based on factors such as the initial salinity of the feed water, the desalination technology employed, and local environmental conditions. Studies have demonstrated that the release of hypersaline brine into marine environments can have severe negative effects on marine life and ecosystems [37].

Current estimates suggest that global brine production reaches approximately 142 million cubic meters per day, representing an increase of around 50% compared to earlier figures. Major contributors include Saudi Arabia, the United Arab Emirates, Kuwait, and Qatar, which together account for 55% of this total. The regions of East Asia-Pacific and North America contribute 18.4% and 11.9% of the world's desalinated water, respectively, with significant outputs from China (7.5%) and the United States (11.2%).

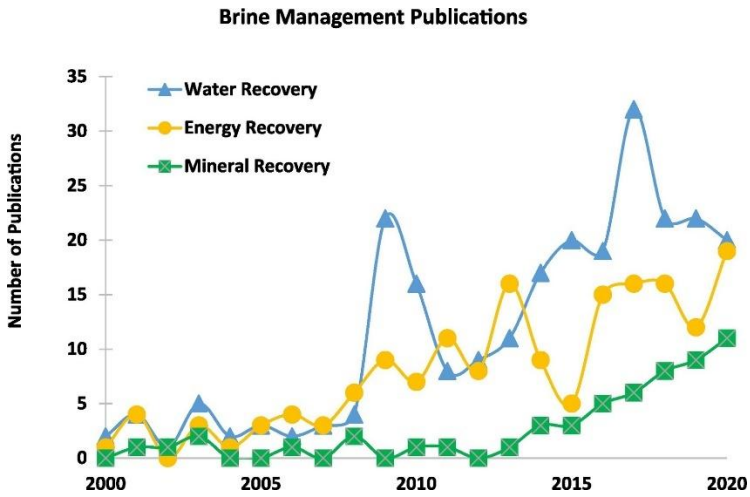


Figure 1.3. *Number of publications related to brine management from 2000 to 2020 (Data obtained from SCOPUS Database using keywords such as "(brine) AND ({water recovery}))", "(brine) AND ({energy recovery}))" and "(brine) AND ({resource recovery} OR {mineral recovery}))") [1].*

With a shift towards a circular economy, the perspective on brine is evolving. Instead of being viewed solely as waste, brine is increasingly recognized as a potential resource. Since brine is primarily composed of water (over 90% by weight), it offers opportunities for additional processing that could enhance the efficiency of the desalination industry. This approach aims to improve the current water recovery rate of around 50% achieved by reverse osmosis (RO). Moreover, brine can be considered a valuable "alternative mine," as it contains a variety of

elements from the periodic table, including minerals that are useful for industrial purposes. In this regard, membrane technologies offer substantial benefits by enabling the recovery of fresh water, energy, and minerals from brine. This not only addresses the challenges of water scarcity and energy consumption but also contributes to the sustainable management of raw materials [38].

1.8 Membrane Distillation and Crystallization: a Dual-Purpose Approach

Membrane distillation (MD) has emerged as a noteworthy hybrid thermal and membrane-based technology within the desalination sector. This method offers notable benefits compared to conventional desalination techniques, such as: i) superior quality of freshwater; ii) a compact and efficient design; iii) reduced vulnerability to osmotic effects and concentration polarization. These advantages have enabled the concentration of saline solutions up to the point of super-saturation, which has led to the advancement of the Membrane Distillation-Crystallization (MD/MCr) approach, aiming at the recovery of essential raw materials from sources like seawater, wastewater, and brine [36].

On the downside, MD/MCr's considerable energy consumption remains a substantial challenge for its broader application. This issue arises primarily from the process's low thermal efficiency, which is caused by temperature polarization (TP), a phenomenon inherently linked to the removal of latent heat during water evaporation, alongside the conduction of heat through the membrane [37].

Nevertheless, the relatively low operational temperature of MD/MCr makes it suitable for integration with renewable energy sources. For instance, solar energy can be transformed into heat via a solar thermal collector, providing the required energy input for the process. In this context, photothermal materials represent a true breakthrough. These materials convert absorbed light into heat, thereby transforming traditional methods of heat collection and expanding the use of natural or artificial radiative energy [38].

The use of photothermal nanomaterials embedded within polymer matrices enables the development of self-heating membranes. These membranes localize heat at the surface, resulting in: i) a natural decrease in energy consumption specific to the process, ii) a substantial improvement in thermal efficiency, and iii) a significant boost in the overall performance of both MD and MCr processes [38].

1.9 Power generation with Photothermal Nanomaterials

The transformation of solar energy into heat is a fundamental aspect of solar power utilization, as it underpins a wide range of applications, including electricity generation, chemical separation, and water purification through desalination [39 - 40 - 41 - 42]. The ability to efficiently convert sunlight into thermal energy has significant implications for renewable energy technologies, as it enables more sustainable and cost-effective solutions for energy and water management.

In traditional solar-to-thermal conversion systems, photothermal materials serve as the primary medium for absorbing light and converting it into heat, enhancing both absorption efficiency and overall energy conversion [43 - 55]. A variety of materials have been explored for this purpose. For instance, metallic nanoparticles (such as gold nanoparticles) can generate heat through surface plasmon resonance, leading to a considerable rise in the local temperature. This plasmonic heating effect has been widely utilized in applications ranging from solar-driven steam generation to liquid-phase separation processes and localized water heating [47- 49].

Beyond metallic nanoparticles, certain organic materials also demonstrate strong photothermal properties. Polypyrrole-based polymers, [50 - 52] along with carbon-derived composite materials, [53 - 55] have exhibited efficient photon-to-thermal conversion due to their broad-spectrum light absorption capabilities. These materials offer an alternative approach to photothermal conversion by leveraging their intrinsic electronic and structural properties to maximize heat generation upon light exposure.

Recent research has turned toward 2D materials (such as transition-metal dichalcogenides (WS_2, MoS_2) and layered metal chalcogenides) for their broad-spectrum light absorption, tunable electronic structure, and high photothermal conversion efficiency [56 - 57]. These materials can be engineered to absorb a wider range of wavelengths, from UV to near-infrared, thus capturing more of the solar spectrum. They also tend to exhibit lower emissivity, which helps minimize radiative heat loss and improves overall energy conversion efficiency.

Moreover, incorporating photothermal 2D materials into membranes can address some of the shortcomings of traditional desalination methods. By localizing heat generation at the membrane surface, these nanofillers help reduce temperature polarization and enhance vapor flux in MD or MCr. As a result, solar-driven MD/MCr systems can operate at lower bulk temperatures while maintaining high evaporation rates. This approach expands the potential for integrating renewable solar power directly into desalination processes.

Further developments focus on ensuring long-term stability, industrial scalability, and environmental safety of these photothermal materials. Ongoing research aims to optimize the synthesis of 2D nanomaterials, improve their dispersion in polymer matrices, and design membrane architectures that fully leverage the light-to-heat conversion without compromising

membrane integrity. Ultimately, photothermal nanomaterials represent a promising frontier for next-generation desalination, power generation, and water-resource management, supporting the broader transition toward sustainable and resilient energy systems.

1.10 Goals and scope of the PhD Project

The primary goal of this PhD project is to develop advanced membrane technologies that leverage renewable energy and nanomaterials for sustainable desalination and resource recovery. The specific objectives include:

- Developing hybrid composite membranes with advanced nanomaterials (such as WS_2, MoS_2, NiSe, CoSe, TiO_2, In_2Se_3, InS) to enhance membrane distillation and crystallization.
- Investigating the potential of nanomaterials for photothermal conversion efficiency in solar-driven desalination.
- Exploring these membranes for the recovery of critical raw materials, like lithium, from brines.
- Evaluating the environmental and economic impact of these technologies.

Hybrid-composite membranes will be prepared by several techniques including ink synthesis of 2D materials and deposition via spray coating, layer-by-layer (LBL), self-assembly of block copolymers (BCPs), and phase separation from ink-polymer blends.

In particular, the technology based on photothermal effects activated by solar radiation will be used within industrial-scale chemical processes such as distillation and crystallization. The photothermal effects activated in nanofillers within polymer matrices, irradiated with solar radiation, will enable the abatement of the adverse effects of temperature polarization in distillation processes, enabling (i) the production of drinking water; (ii) the removal of contaminants from water; (iii) the recovery of valuable minerals from the sea; and (iv) the production of energy by salt concentration gradient.

The electronic and structural properties of the inks and the morphological-structural and chemical-physical properties of the membranes will be characterized as a function of the 2D material used, evaluating confinement effects, productivity efficiency, selectivity, energy conservation, and reusability.

The morphology and physicochemical properties of 2D materials will be investigated with X-ray diffraction (XRD), Atomic Force Microscopy (AFM), Ultraviolet–visible spectrophotometry (UV-VIS), X-ray photoelectron spectroscopy (XPS), Trasmission Electron Microscopy (TEM), and Scanning Electron Microscopy (SEM). The stability of 2D materials confined in polymer

matrix will be investigated by Raman, Infrared spectroscopy (IR), Differential scanning calorimetry (DSC). Morphological-structural parameters of membranes will be analyzed by SEM and AFM, porosimeters, and mechanical tests. The hydrophobicity of the membranes will be evaluated by wettability and liquid water intrusion resistance measurements. The performance of new membranes will be evaluated in MD/MCr processes by considering (i) photothermal effects on transport, selectivity, thermal efficiency, activated by 2D materials with and without irradiation; (iii) structural and electronic correlations of 2D materials and assisted mechanisms of transport, nucleation and selective crystal growth.

The potential market impact of these nanocomposite membranes is significant, especially given the annual growth rate of 7.8% in the desalination sector. While reverse osmosis remains the dominant technology (requiring 3-4 kWh/m³) these novel solar-driven MD/MCr processes could greatly promote the transition towards sustainable and resilient energy system and widen the scope of application, especially in areas lacking a stable energy grid. By addressing both the energy and water challenges, this research aims to foster more sustainable, circular solutions for the global desalination industry.

References

[1] Ogunbiyi, O.; Saththasivam, J.; Al-Masri, D.; Manawi, Y.; Lawler, J.; Zhang, X.; Liu, Z. (2021) Sustainable brine management from the perspectives of water, energy and mineral recovery: A comprehensive review. Desalination, 513, 10.1016/j.desal.2021.115055

[2] K. Burrows and P. L. Kinney, Exploring the Climate Change, Migration and Conflict Nexus, Int. J. Environ. Res. Public Health 2016, 13(4), 443 10.3390/ijerph13040443

[3] L. Chen, G. Msigwa, M. Yang, A. I. Osman, S. Fawzy, D. W. Rooney, Strategies to achieve a carbon neutral society: a review, Environmental Chemistry Letters, Volume 20, pages 2277–2310, (2022), 10.1007/s10311-022-01435-8

[4] Alib, A.; Tufa, R. A.; Macedonio, F.; Curcio, E.; Drioli E. (2018) Membrane technology in renewable-energy driven desalination. Renewable and Sustainable Energy Reviews,81, 1-21. 10.1016/j.rser.2017.07.047

[5] A. J. K. Karabelas, C.P.; Kostoglou, M.; Sioutopoulos, D.C., Analysis of specific energy consumption in reverse osmosis desalination processes, Desalination 431, 2018, 10.1016/j.desal.2017.04.006

[6] E. Jones, M. Qadir, M. T.H. van Vliet, V. Smakhtin, S. Kang, The state of desalination and brine production: A global outlook, Science of The Total Environment, 657, 10.1016/j.scitotenv.2018.12.076

[7] Elkadeem, M.R., Kotb, K.M.; Elmaadawy, K.; Dán, A.; Sharshir, S.W. (2021) Feasibility analysis and optimization of an energy-water-heat nexus supplied by an autonomous hybrid renewable power generation system: An empirical study on airport facilities. Desalination, Vol. 504, 114952, 10.1016/j.desal.2021.114952

[8] Ji, X.; Curcio, E.; Al Obaidani, S.; Di Profio, G.; Fontananova, E.; Drioli, E. (2010) Membrane distillation crystallization seawater, 10.1016/j.seppur.2009.11.004.

[9] Politano, A.; Argurio, P. ; Di Profio, G. ; Sanna, V.; Cupolillo, A.; Chakraborty, S.; Arafat, H.A.; Curcio, E. (2017) Photothermal Membrane Distillation for Seawater Desalination, Adv. Mater. 29, 1–6, 10.1002/adma.201603504.

[10] Avci, A.H.; Messana, D.A.; Santoro, S.; Tufa, R.A.; Curcio, E.; Di Profio, G.; Fontananova, E. (2020) Energy Harvesting from Brines by Reverse Electrodialysis Using Nafion Membranes. Membranes, 10, 168, 10.3390/membranes10080168

[11] Maril, M., Delplancke, J. L., Cisternas, N., Tobosque, P., Maril, Y., & Carrasco, C. (2022). Critical aspects in the development of anodes for use in seawater electrolysis. International Journal of Hydrogen Energy, 47(6), 3532 3549. 10.1016/J.IJHYDENE.2021.11.002

[11 a] https://www.wri.org/

[12] Accessed on March 2025, http://www.crrinnovabili.it/impianto-solare-termodinamico-concentrazione/

[13] Huang, Z., Liu, X., Sun, S., Tang, Y., Yuan, X., & Tang, Q. (2021). Global assessment of future sectoral water scarcity under adaptive inner-basin water allocation measures. Science of The Total Environment, 783, 146973. 10.1016/J.SCITOTENV.2021.146973

[14] Zetland, D., The role of prices in managing water scarcity. Water Security, 12, 100081. 10.1016/J.WASEC.2020.100081

[15] Chave K.E. Chemical reactions and the composition of sea water, J. Chem. Educ., 48/3,pp. 148–150, 10.1021/ed048p148

[16] A. Uihlein, D. Magagna, Wave and tidal current energy – A review of the current state of research beyond, Renewable and Sustainable Energy Reviews, Volume 58, May 2016, Pages 1070-1081, 10.1016/j.rser.2015.12.284

[17] Horne, R.A. (1970) Sea water, Advances in Hydroscience, 6, 107–140, 10.1016/B978-0-12-021806-6.50009-5

[18] Zhao, T., Xu, M., Xiao, X., Ma, Y., Li, Z., & Wang, Z. L. (2021) Recent progress in blue energy harvesting for powering distributed sensors in ocean. Nano Energy, 88, 106199. 10.1016/J.NANOEN.2021.106199

[19] G. Ramasamy, P. K. Rajkumar, M. Narayanan, Generation of energy from salinity gradients using capacitive reverse electro dialysis: a review, 10.1007/s11356-020-12188-8

[20] L. Chen, G. Msigwa, M. Yang, A. I. Osman, S. Fawzy, D. W. Rooney, Strategies to achieve a carbon neutral society: a review, Volume 20, pages 2277–2310, 10.1007/s10311-022-01435-8

[21] Veerman J., Saakes M., Metz S.J., Harmsen G.J. (2009) Reverse electrodialysis: performance of a stack with 50 cells on the mixing of sea and river water. J Membr Sci., 327:136-44, 10.1016/j.memsci.2008.11.015

[22] C. Tristán, Fallanza, M., Ibáñez, R., Ortiz, I., Recovery of salinity gradient energy in desalination plants by reverse electrodialysis, Desalination Volume 496, 15 December 2020, 114699, 10.1016/j.desal.2020.114699

[23] Tufa, R.A., Curcio E., Van Baak, W., Veerman, J., Grasman, S., Fontananova, E., Di Profio, G. (2014) Potential of brackish water and brine for energy generation by salinity gradient power-reverse electrodialysis (SGP-RE). RSC Adv; 4:42617e23, 10.1039/C4RA05968A

[24] Tedesco, M.; Brauns, E.; Cipollina, A.; Micale, G.; Modica, P.; Russo, G.; Helsen, J. (2015) Reverse electrodialysis with saline waters and concentrated brines: a laboratory investigation towards technology scale up, J. Membr. Sci., 492, pp. 9–20, 10.1016/j.memsci.2015.05.020

[25] Tedesco, M.; Cipollina, A.;Tamburini, A., Micale, G.; Helsen, J.; Papapetrou, M. (2014), REAPower: use of

desalination brine for power production through reverse electrodialysis, Desalin. Water Treat., 53,pp. 3161–3169, 10.1080/19443994.2014.934102

[26] Huang, Z., Yuan, X., & Liu, X., The key drivers for the changes in global water scarcity: Water withdrawal versus water availability, Journal of Hydrology, 601, 126658 10.1016/J.JHYDROL.2021.126658.

[27] Ram, M., Osorio-Aravena, J. C., Aghahosseini, A., Bogdanov, D., & Breyer, C. (2022). Job creation during a climate compliant global energy transition across the power, heat, transport, and desalination sectors by 2050. Energy, 238, 121690. 10.1016/J.ENERGY.2021.121690

[28] Ben Ali, I., Turki, M., Belhadj, J., & Roboam, X. (2020). Systemic design and energy management of a standalone battery-less PV/Wind driven brackish water reverse osmosis desalination system. Sustainable Energy Technologies and Assessments, 42, 100884. 10.1016/J.SETA.2020.100884

[29] Abdel-Jawad, M., Ebrahim, S., Al-Atram, F., & Al-Shammari, S. Pretreatment of the Municipal Wastewater Feed for Reverse Osmosis Plants. Restoration and Rehabilitation of the Desert Environment, 229 245. 10.1016/B978-0-444-82471-4.50028-8

[30] Veerman J., Saakes M., Metz S.J., Harmsen G.J. (2009) Reverse electrodialysis: performance of a stack with 50 cells on the mixing of sea and river water. J Membr Sci., 327:136-44, 10.1016/j.memsci.2008.11.015.

[31] Catrini, P., Cipollina, A., Micale, G., Piacentino, A., & Tamburini, A. (2017). Exergy analysis and thermoeconomic cost accounting of a Combined Heat and Power steam cycle integrated with a Multi Effect Distillation-Thermal Vapour Compression desalination plant. Energy Conversion and Management, 149, 950 965. 10.1016/J.ENCONMAN.2017.04.032

[32] https://sustainabledevelopment.un.org/content/documents/5734Blue%20Energy.pdf

[33] https://ec.europa.eu/environment/water/index_en.htm

[34] Drioli, E., Di Profio, G., Curcio, E. (2012) Progress in membrane crystallization, Curr. Opin. Chem. Eng. 1, 178 182, 10.1016/j.coche.2012.03.005

[35] Lacey, R.E. (1980) Energy by reverse electrodialysis. Ocean Eng. 7, 1–47, 10.1016/0029-8018(80)90030-X

[36] Zetland, D. (2021). The role of prices in managing water scarcity. Water Security, 12, 100081. 10.1016/J.WASEC.2020.100081

[37] Santoro,S., Vidorreta, I.M., Sebastian, V., Moro, A., Coelhoso, I.M., Portugal, C.A.M., Lima, J.C., Desiderio, G., Lombardo, G., Drioli, E., Mallada, R., Crespo, J.G., Criscuoli, A., Figoli, A. (2017) A non-invasive optical method for mapping temperature polarization in direct contact membrane distillation, J. Memb. Sci. 536, 156 166. 10.1016/j.memsci.2017.05.001

[38] Politano, A., Argurio, P., Di Profio, G., Sanna, V., Cupolillo, A., Chakraborty, S., Arafat, H.A., Curcio, E. (2017) Photothermal Membrane Distillation for Seawater Desalination, Adv. Mater. 29, 1603504. 10.1002/adma.201603504

[39] N. S. Lewis, *Science* 2016, **351**, 353. 10.1126/science.aad1920

[40] Y. Parent, D. Blake, K. Magrini-Bair, C. Lyons, C. Turchi, A. Watt, E. Wolfrum, M. Prairie, *Sol. Energy* 1996, **56**, 429. 10.1016/0038-092X(96)81767-1

[41] H. Tong, S. X. Ouyang, Y. P. Bi, N. Umezawa, M. Oshikiri, J. H. Ye, *Adv. Mater.* 2012, **24**, 229. 10.1002/adma.201102752

[42] D. Bahnemann, *Sol. Energy* 2004, **77**, 445. 10.1016/j.solener.2004.03.031

[43] D. Kraemer, B. Poudel, H. P. Feng, J. C. Caylor, B. Yu, X. Yan, Y. Ma, X. W. Wang, D. Wang, A. Muto, K. McEnaney, M. Chiesa, Z. Ren, G. Chen, *Nat. Mater.* 2011, **10**, 532. 10.1038/nmat3013v

[44] G. M. Ayoub, A. A. Hindi, L. Malaeb, *Desalination* 2009, **242**, 128. 10.1016/j.desal.2008.03.036

[45] Y. Zeng, J. F. Yao, B. A. Horri, K. Wang, Y. Z. Wu, D. Li, H. T. Wang, *Energy Environ. Sci.* 2011, **4**, 4074. 10.1039/C1EE01532J

[46] O. Neumann, A. S. Urban, J. Day, S. Lal, P. Nordlander, N. J. Halas, *ACS Nano* 2013, **7**, 42. 10.1021/nn304948h

[47] O. Neumann, A. D. Neumann, E. Silva, C. Ayala-Orozco, S. Tian, P. Nordlander, N. J. Halas, *Nano Lett.* 2015, **15**, 7880. 10.1021/acs.nanolett.5b02804

[48] P. Tao, W. Shang, C. Y. Song, Q. C. Shen, F. Y. Zhang, Z. Luo, N. Yi, D. Zhang, T. Deng, *Adv. Mater.* 2015, **27**, 428. 10.1002/adma.201401449

[49] Y. M. Liu, S. T. Yu, R. Feng, A. Bernard, Y. Liu, Y. Zhang, H. Z. Duan, W. Shang, P. Tao, C. Y. Song, T. Deng, *Adv. Mater.* 2015, **27**, 2768. 10.1002/adma.201500135

[50] L. B. Zhang, B. Tang, J. B. Wu, R. Y. Li, P. Wang, *Adv. Mater.* 2015, **27**, 4889. 10.1002/adma.201502362

[51] Y. Liu, D. D. Wang, L. Zhao, M. Lin, H. Z. Sun, H. C. Sun, B. Yang, *RSC Adv.* 2016, **6**, 15854. 10.1039/C5RA25613E

[52] T. Park, J. Na, B. Kim, Y. Kim, H. Shin, E. Kim, *ACS Nano* 2015, **9**, 11830. 10.1021/acsnano.5b04042

[53] Y. Ito, Y. Tanabe, J. H. Han, T. Fujita, K. Tanigaki, M. W. Chen, *Adv. Mater.* 2015, **27**, 4302. 10.1002/adma.201501832

[54] H. Ghasemi, G. Ni, A. M. Marconnet, J. Loomis, S. Yerci, N. Miljkovic, G. Chen, *Nat. Commun.* 2014, **5**, 4449. 10.1038/ncomms5449

[55] G. Katumba, L. Olumkor, A. Forbes, G. Makiwa, B. Mwakikunga, J. Lu, E. Wäcklgård, *Sol. Energy. Mater. Sol. Cells* 2008, **92**, 1285. 10.1016/j.solmat.2008.04.023

[56] S. J. Norton, T. Vo-Dinh, *J. Appl. Phys.* 2016, **119**, 083105. 10.1063/1.4942623

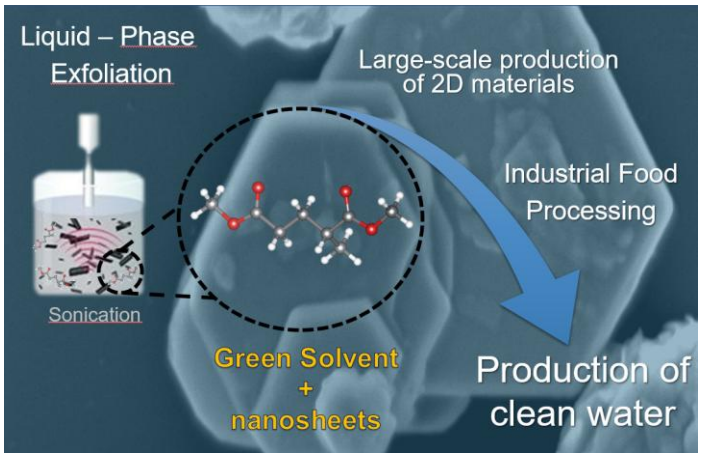
[57] V. T. Truong, *Synth. Met.* 1992, **52**, 33. 10.1016/0379-6779(92)90017-D

Chapter 2

Dimethyl 2-Methylglutarate (Iris): A Green Platform for Efficient Liquid-Phase Exfoliation of 2D Materials

Keywords: 2D Materials; Green Chemistry; Iris; Liquid-phase Exfoliations

GRAPHICAL ABSTRACT



Contents

Abstract

2.1 Introduction to 2D Materials: Challenges and solutions

2.1.1 Scalability Challenges and Solvent Selection for LEP

2.1.2 A Sustainable Alternative: Dimethyl 2-Methylglutarate (Iris)

2.2 Results and Discussion

2.2.1 Surface Tension Considerations for Iris-assisted Exfoliation

2.2.2 Structural and optical Characterization of nanosheets

2.2.3 Chemical Stability and Exfoliation Mechanism

2.3 Conclusion

2.4 Experimental Section

References

This chapter has been published as:

D'Olimpio G., Occhiuzzi J., Lozzi L., Ottaviano L, Politano A., Dimethyl 2-Methylglutarate (Iris): A Green Platform for Efficient Liquid-Phase Exfoliation of 2D Materials, Adv. Sustain. Syst. 2022, 6, 2200277;
https://doi.org/10.1002/adsu.202200277

Abstract

Liquid-phase exfoliation of bulk crystals of layered materials, held together by weak interlayer van der Waals forces, is an ideal platform for scalable synthesis of nanosheets. However, it is mandatory to substitute existing solvents, regrettably displaying severe limitations due to toxicity. Here, dimethyl 2-methylglutarate (Rhodiasolv$^{(R)}$ Iris) is validated for efficient liquid-phase exfoliation of selected van der Waals materials, namely, MoS_2, WS_2, GeSe, and graphite. Here, we show that Iris-assisted liquid phase exfoliation provides high yield (up to 52%) of flakes of 2D materials with aspect ratio as high as 500. Considering the various advantages of Iris over the state-of-the-art solvents, including the absence of toxicity and its biodegradability, the present work was carried out as part of my PhD research. This opens new possibilities for the ecofriendly production of 2D materials and for their extensive usage in industrial processes hitherto semi-unexplored, owing to the toxicity of state-of-the-art solvents (including the production of drinkable water or fruit juice concentration). Accordingly, the validation of Iris for sustainable liquid-phase exfoliation of van der Waals crystals has intrinsic outstanding potential commercial impact. Moreover, PhD work presents, for the first time, the surface tension, Hansen solubility parameter, and viscosity of Rhodiasolv Iris. These parameters are critical for the development of sustainable processes based on this innovative green solvent.

2.1 Introduction to 2D Materials: Challenges and solutions

2.1.1 Scalability challenges and solvent selection for LEP

The emergence of 2D materials [1-8] had a tremendous impact on the scientific research, in consideration of the unique properties and their broad technological prospect in photonics [9], flexible electronics [10], nanocomposites [11, 12], (photo)electrocatalysis [13-15], supercapacitors [16, 17], functional coatings[18], (bio)sensors [19] and desalination [11, 20-22]. The large-scale manufacture of atomically thin layers is hitherto an important hurdle in the pathway for the industrial exploitation of 2D materials [23, 24]. While most basic investigations on 2D materials were performed on flakes prepared by mechanical exfoliation [25] or on atomically thin layers synthetized by chemical vapor deposition [26], unfortunately such methods are unfeasible to tackle scalability. As a matter of fact, mechanical exfoliation is poorly reproducible and with scarce yield [25], while chemical vapor deposition is affected by the need of a suitable substrate[27], which should be successively etched and transferred [28], with the consequent insufficient crystallinity (owing to the unavoidable presence of defects [29]) and cleanliness (associated to polymeric residuals in the successive transfer process [30, 31]) of

produced 2D materials. On the other hand, liquid-phase exfoliation (LPE) from parental bulk crystals is ideal for a scalable production of 2D materials, dispersed in solvents, suitable for their successive implementation [32]. Solvents for LPE must minimize the energy cost for separating the sheets by breaking the weak interlayer van der Waals bonds. Specifically, the interfacial surface tension between the solid and the liquid should be minimized [33, 34]. One of the most widely used models for describing interfacial surface tension is the Owens, Wendt, Rabel, and Kaelble (OWRK) model, which decomposes the interfacial surface tension into i) polar and ii) dispersive components. By selecting the most opportune ratios between these quantities in the solvent and in the layered materials, the yield is maximized based on the minimization of the surface tension. Specifically [33]

$$\sigma_{sl} = \sigma_s + \sigma_l - 2\left(\sqrt{{\sigma_s}^d \cdot {\sigma_l}^d} + \sqrt{{\sigma_s}^p \cdot {\sigma_l}^p}\right)$$
$$= {\sigma_s}^d + {\sigma_s}^p + {\sigma_l}^d + {\sigma_l}^p - 2\left(\sqrt{{\sigma_s}^d \cdot {\sigma_l}^d} + \sqrt{{\sigma_s}^p \cdot {\sigma_l}^p}\right) \quad (1)$$

where σ_s is the surface tension of the solid (i.e., materials to be exfoliated) and σ_l is the surface tension of the liquid (i.e., the solvent). The superscripts "p" and "d" stand for polar and dispersive components, respectively. σ_{sl} is the interfacial surface tension between the material and the solvent, which should be minimized to optimize the efficiency of the exfoliation.

Equation (1) can be also expressed as

$$\sigma_{sl} = \left(\frac{{\sigma_s}^p}{{\sigma_s}^d} + 1\right){\sigma_s}^d + \left(\frac{{\sigma_1}^p}{{\sigma_1}^d} + 1\right){\sigma_1}^d - 2\left(\sqrt{\left(\frac{{\sigma_s}^p}{{\sigma_s}^d} + 1\right){\sigma_s}^d} + 1\right)\sqrt{{\sigma_1}^d \cdot {\sigma_s}^d}$$
$$= \left(\sqrt{{\sigma_s}^d}\sqrt{\left(\frac{{\sigma_s}^p}{{\sigma_s}^d} + 1\right)} - \sqrt{{\sigma_1}^d}\sqrt{\left(\frac{{\sigma_1}^p}{{\sigma_1}^d} + 1\right)}\right)^2$$
$$+2\sqrt{{\sigma_1}^d \cdot {\sigma_s}^d}\left(\sqrt{\left(\frac{{\sigma_1}^p}{{\sigma_1}^d} + 1\right)}\sqrt{\left(\frac{{\sigma_s}^p}{{\sigma_s}^d} + 1\right)} - \sqrt{\left(\frac{{\sigma_1}^p{\sigma_s}^p}{{\sigma_1}^d{\sigma_s}^p}\right)} - 1\right) \quad (2)$$

By inspecting Equation (2), it can be seen that in order to minimize interfacial surface tension of 2D materials and solvents, the following conditions should be verified i) $\sigma_s^d \approx \sigma_l^d$ and ii) $\sigma_s^p \approx \sigma_l^p$ and, consequently,

$$\frac{\sigma_s{}^p}{\sigma_s{}^d} \approx \frac{\sigma_l{}^p}{\sigma_l{}^d} \tag{3}$$

Moreover, the dispersibility of nanosheets in a specific solvent is another key issue, subject to the peculiar solvent-solute interaction, described by contemplating the Hansen solubility parameters (HSP) to account dispersion forces (δ_d), polar interactions (δ_P), and hydrogen bonds (δ_H).

Whensoever δ_d, δ_P, and δ_H values of the solvent closely match those of the solute, the total interaction energy required for exfoliation and dispersion is minimized.

The most diffuse solvents for dispersion of van der Waals crystals are N,N-dimethylformamide (DMF) and NMP [35], owing to a good matching of their surface energy and HSP (reported in Table 1) with surface tension and HSP of solvents in Table 2.

Table 2.1. *Surface energy and Hansen solubility parameters of van der Waals crystals.*

	Surface Energy	**Hansen Solubility Parameters**		
	E_{sur} [mNm^{-1}]	**δ_d [MPa$^{1/2}$]**	**δ_p [MPa$^{1/2}$]**	**δ_H [MPa$^{1/2}$]**
Graphite [52]	≈62	≈18	≈9.3	≈7.7
MoS2 [57]	≈70	17–19	6–12	4.5–8.5
WS_2 [57]	≈75	16–18	5–14	2–19
GeSe [58]	≈220	n.a.	n.a.	n.a.

Table 2.2. *Surface tension and the Hansen solubility parameters for Iris, NMP, DMF, IPA and Urea.*

	Surface Tension	**Hansen Solubility Parameters**		
	σ_s [mNm^{-1}]	**δ_d [MPa$^{1/2}$]**	**δ_p [MPa$^{1/2}$]**	**δ_H [MPa$^{1/2}$]**
NMP	40.1	18.0	12.3	7.2
DMF	37.1	17.4	13.7	11.3
IPA	21.7	15.8	6.1	16.4
Urea 30% in H_2O	74.0	17.0	16.7	38.0
Iris	33.0	16.6	8.7	5.0

Unfortunately, DMF and NMP show severe toxicity issues (including as reproductive toxin [36]), which have determined restriction to their use in both USA [37, 38] and Europe (where they are listed among substances of very high concern [39]).

2.1.2 A Sustainable Alternative: Dimethyl 2-Methylglutarate (Iris)

The quest of an ecofriendly substitute to such standard aprotic solvents is mandatory. Several possible candidates show remarkable pitfall. As an example, volatile organic compounds (VOCs) display an insufficient exfoliation yield [40], with the need to transfer nanosheets from NMP suspensions[41]. Moreover, most VOC exhibit flash temperatures as low as 10–13 °C, with consequent issues for safe industrial procedures. Another possibility for LPE is represented by electrochemical exfoliation in electrolytes [37], which however requires the addition of conductive additives [42] for insulating and semiconducting samples. Moreover, it produces highly defective nanosheets [37, 43] with thickness far from the monolayer regime [44]. Moreover, for LPE assisted by urea aqueous solutions [45], the yield is as low as 2.4%, due to a surface tension significantly different from other solvents (Table 2).

On the other hand, residuals are unavoidable for LPE assisted by surfactants in aqueous media [46].

As regards dihydrolevoglucosenone (Cyrene), whose use in LPE has been recently explored [47], one should mention that its excessive dynamic viscosity (around 15 cP at room temperature) impedes any use in inkjet printing.

Manifestly, current methods using standard solvents inexorably inhibit the scalability of Flatland-based industry. Thus, the quest of a solvent enabling i) sustainable LPE and ii) high yield is mandatory.

In the present PhD work, we validate the use of dimethyl 2-methylglutarate (Rhodiasolv Iris, CAS: 33514-22-6) as a polar solvent for sonication-assisted LPE of van der Waals crystals. Iris ($C_8H_{14}O_4$) does not display measurable toxicity for doses below 2000 mg kg^{-1} d^{-1}. Its water solubility is higher than 25 g L^{-1} at T = 23 °C. Notably, Iris has a flash point of 90.8 °C [48].

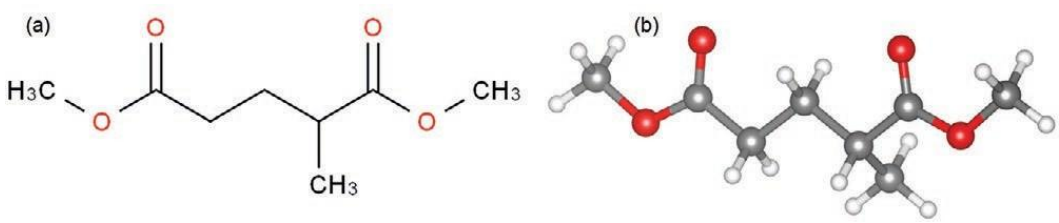


Figure 2.1. *a) Plain and b) ball-and-stick representations of the atomic structure of dimethyl 2 – methylglutarate (Iris).*

The sufficiently high dynamic viscosity (2.85 cP at T = 20 °C) enables suitable use in ink-jet printing of nanosheets-based devices, contrarily to NMP and DMF, which suffer poor jet performance, owing to a dynamic viscosity below 2 cP [49].

Specifically, by adopting as case-study examples MoS_2, WS_2, GeSe, and graphene, we demonstrate the suitability of Iris to produce atomically thin layers of layered materials by sonication-assisted LPE. The absence of any toxicity issues in Iris, with an exfoliation yield as high as 52%, enables the use of 2D materials in agri-food industry (including the production of potable water[50] or fruit juices[51]).

2.2 Results and Discussion

2.2.1 Surface Tension Considerations for Iris-assisted Exfoliation

The value of the surface tension of Iris (33.0 mN m^{-1}, Table 2) resembles the cases of NMP and DMF, whereas it is lower by ≈35% in isopropyl alcohol (IPA). By defining the surface tension (σ_s) as

$$\sigma_s = (E_{Sur} - TS_{Sur}) \tag{4}$$

where E_{Sur} corresponds to surface energy, T is the temperature and S_{Sur} surface entropy and considering S_{Sur} for liquids generally is around 0.1 mN m^{-1}, one can conclude that generally a mismatch by at least 30 mN m^{-1} exists between the surface energy of the van der Waals crystals with surface tensions of solvents at room temperature [56].

2.2.2 Structural and optical Characterization of nanosheets

The effectiveness of Iris to achieve high-yield dispersions of nanosheets was certified through an examination of dispersed flakes for selected cases of MoS_2, WS_2, GeSe, and graphite.

First, the yield of the process in terms of the amount of nanosheets with respect to the initial concentration was evaluated to range between 38% and 52% in all cases in the same conditions.

In the case of MoS_2, a single flake initially identified using bright field scanning transmission electron microscopy (BF-STEM) (Figure 2.2 a) was further analyzed with atomic-resolution high-angle annular dark field scanning transmission electron microscopy (HAADF-STEM) (Figure 2.2 b), which confirmed the absence of structural damage in the basal plane of the nanosheets.

Accordingly, sonication-assisted LPE of van der Waals crystals with the Rhodiasolv Iris solvent just breaks weak interlayer van der Waals bonds. We were unable to detect defective regions, even for statistical analyses extended to 13 different samples.

Moreover, the lack of any modification in the electronic band structure was secured by UV–Vis absorption data (Figure 2.2 c).

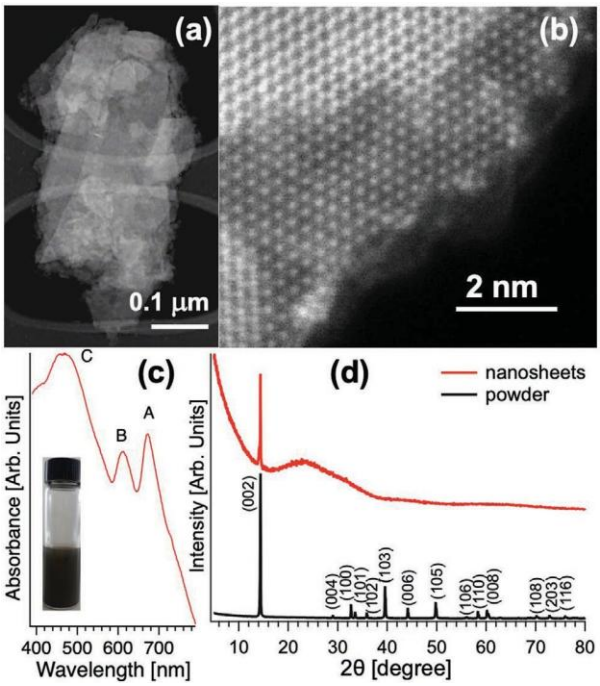


Figure 2.2. *a) BF-STEAM image with various nanosheets of MoS_2 on a lacey carbon grid. b) High-resolution high-angle annular dark field-STEM image for a self-standing nanosheet. c) UV–Vis spectrum of MoS_2 nanosheets produced by Iris-assisted LPE. d) XRD pattern of (black curve) powdered MoS_2 bulk crystals and (red curve) exfoliated nanosheets of MoS_2.*

Especially, observation of the peculiar absorptions at 674 and 612 nm related to the A and B excitons of MoS_2, originating from the interband excitonic transition at the K point of the Brillouin zone [59-61], secures that the LPE in Iris solvent did not modify the electronic band structure of MoS_2.

The final MoS_2 dispersion had a concentration of 0.18 mg mL^{-1} (with a yield of ≈ 52% of the initial mass in the final dispersion). The stability of the dispersions was evaluated by acquiring daily photographs for 10 d, which indicated that 67% of the nanosheets persist in the dispersions after 10 d.

X-ray diffraction (XRD) measurements were used to evaluate the crystal structure of MoS_2 nanosheets obtained by Iris-assisted LPE with respect to the bulk MoS_2 (Figure 2.2 d). Powders of

bulk MoS_2 exhibited the characteristic XRD pattern of a hexagonal structure [62], with peaks matching with International Centre for Diffraction Data ref no. 04-003-3374. On the other hand, the appearance of a strong (002) reflection centered at 14.4° in the XRD pattern of exfoliated MoS_2 nanosheets secured their good crystallinity (Figure 2.2 d), congruently with results in ref. [8].

Figure 2.3 shows the log-normal distribution of lateral size (peaked around ≈ 0.5 µm) and thickness (peaked around ≈ 6 nm) of MoS_2 nanosheets produced by Iris-assisted LPE, based on the statistical analysis of experiments by scanning electron microscope (SEM) and atomic force microscope (AFM).

The statistical analyses on the thickness of exfoliated flakes revealed that a bimodal distribution with the second maximum located even at 30 nm, thus inferring an incomplete exfoliation of the parental bulk crystals, also clarified by supporting STEM images. Correspondingly, Iris-assisted LPE provides 98% of flakes with thickness below 15 nm.

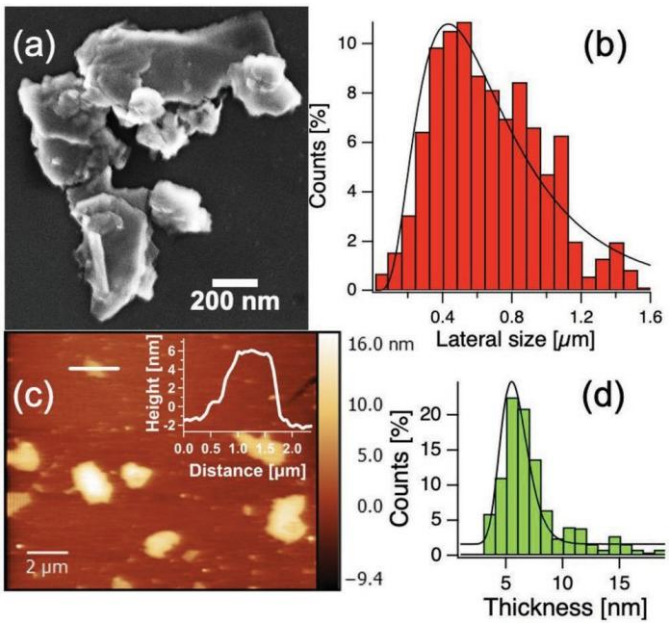


Figure 2.3. *a) Selected high-resolution SEM picture of MoS_2 nanosheet. b) Distribution of lateral size of MoS_2 nanosheets based on SEM experiments. c) Selected AFM picture of MoS_2 flakes. The inset reports the height profile along the white solid line. d) Thickness distribution derived from AFM experiments.*

2.2.3 Chemical stability and Exfoliation Mechanism

To assess eventual influence of LPE with Iris solvent on MoS_2, X-ray photoelectron spectroscopy (XPS) characterization was performed. Core-level spectra of bulk and exfoliated MoS_2 are shown in Figure 2.4.

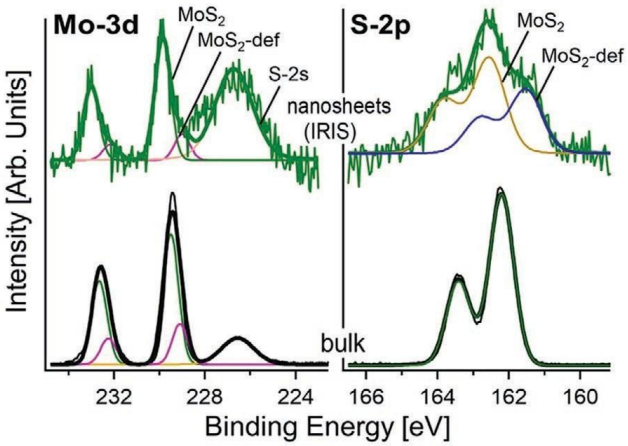


Figure 2.4. *Mo-3d and S-2p core-level XPS spectra of bulk and nanosheets of MoS_2 exfoliated in Iris. The component at a BE of 226.7 eV in Mo-3d core level is related to the overlapping S-2s core level. The photon energy is 1486.6 eV (Al K_α) and the spectra are normalized to the maxima.*

The Mo-3d core levels are split in J = 5/2 and 3/2 components shifted by 3.1 eV. Specifically, XPS measurements indicate that Mo-3d core levels displays two different contributions arising from pristine (fully coordinated atoms) and defective MoS_2 (sulfur vacancies, related to neighboring vacancy sites) with a binding energy (BE) of 229.8 and 229.0 eV for the J = 5/2 component, respectively, in agreement with previous works on MoS_2-based systems [63]. Actually, defects introduce a minority component at lower BE, due to a redistribution of charge. Specifically, the charge localized on the more electronegative sulfur atom, once it is desorbed, is redistributed on the first neighboring atoms, so as to enhance the Coulomb screening effect [64-66]. Notably, we note in Mo-3d spectra the absence of MoO_3-derived spectral features, which should appear at a BE of 232.4 eV for the J = 5/2 component [67]. Therefore, we can conclude that Iris does not act as an oxidation agent for the MoS_2 nanosheets and, correspondingly, Iris-assisted liquid-phase exfoliation process does not favor the oxidation of MoS_2 flakes. Concerning the S-2p core levels, they are split in J = 3/2 and 1/2 components shifted by 1.2 eV. Two well-distinct contributions associated to pristine and defective MoS_2 are observed at a BE of 162.5 and 161.5 eV for the J = 3/2 component, respectively, as in previous reports [64, 65]. Correspondingly, in S-2p core level no trace of sulfur-oxide phases was found.

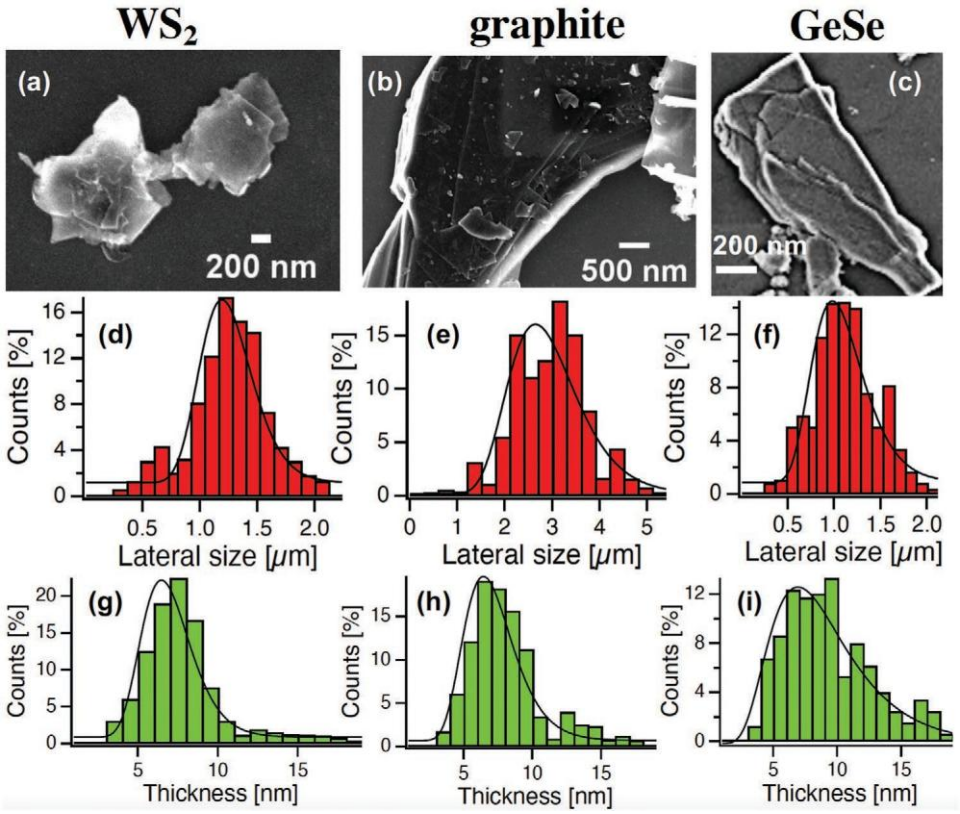


Figure 2.5. *Selected SEM images of Iris-assisted LPE-exfoliated nanosheets of a) WS_2, b) graphite, and c) GeSe. Statistical analysis of d–f) lateral size and g–i) thickness of d,g) WS_2, e,h) graphite, and f,i) GeSe flakes, respectively.*

To endorse the use of Iris as a suitable solvent for sonication-assisted LPE of van der Waals crystals, we validated its effectiveness for the cases of WS_2, graphite, and GeSe (Figure 2.5).

Panels (a–c) of Figure 2.5 report a representative SEM image of Iris-exfoliated WS_2, few-layer graphene, and GeSe nanosheets. Their corresponding distribution of lateral size and thickness are reported in panels (d–f) and (g–i), respectively.

As concerns WS_2 exfoliation, statistical analyses on both lateral size and thicknesses (Figure 2.5 d,g) reveal similar values compared to the case of MoS_2. Precisely, the distribution of lateral size is centred around ≈1.2 μm, whereas the thickness distribution is peaked around 7 nm. As regards the exfoliation of few-layer graphene flakes with Iris, the average lateral size exceeds 3 μm, with an average thickness of 7 nm. GeSe flakes have average lateral area and thickness of 1 and 9 nm, respectively. It is also important to remark that the use of other solvents for LPE of Ge bulk crystals could provide undesired effects. As an example, IPA provides nucleation of Se nanowires through abstraction of Se from the surface of GeSe flakes with the self-assembled formation of Se nanowires. Actually, for all case-study examples of van der Waals crystals studied for Iris, only 2D nanosheets with an aspect ratio exceeding 10^2 were obtained, with the highest aspect ratio being 500 for few-layer graphene. It should be noticed that all types of the exfoliated 2D flakes have rugged edge (Figures 2.2, 2.3, and 2.5), while LPE assisted by other solvents, such as NMP,

provides flakes with sharp edges with well-defined angle between, following some sort of crystallographic orientation, congruently with findings in literature [68]. Recently, Coleman and co-workers [68] have demonstrated that, in the early stages of LPE, sonication induces the breakage of large flakes, with the formation of kink band striations on the flake surfaces, predominantly along zigzag directions. Then, cracking occurs along these striations and, together with intercalation of solvent, thin strips of van der Waals crystals are unzipped and peeled off, lastly affording atomically thin layers. The above-mentioned difference regarding the shape of the flakes produced by Iris-assisted LPE could be rationalized by considering that, following suggestions by Bari et al. [69], the shape of edges and folds in nanosheets produced by sonication-assisted LPE are correlated to their bending moduli and sonication response. Correspondingly, the difference in the shape of the same crystal exfoliated with NMP and Iris could be correlated to the sonication response. One can infer that a key role could be played by the particularly reduced value of HSP of the Iris solvent, related to polar interactions (δ_P) and hydrogen bonds (δ_H), as reported in Table 2.

2.3 Conclusion

We have validated Iris as a suitable green solvent for producing atomically thin layers of van der Waals crystals with nanometric thickness and micrometric lateral size. Based on our results, one can propose that Iris could also substitute solvents usually used for all processes, such as shear mixing [70] or wet-jet mill [71], particularly promising for industrial scale up. The efficiency of the Iris-based LPE process is crucial in order to combine intrinsic benefits for environmental health and safety with optimization of performances. Undeniably, the introduction of a green solvent for LPE also will expand the growing market of 2D materials toward fields to date nearly unexplored (e.g., recovery of minerals from seawater, concentration of fruit juices, production of drinking water, etc.), as a result of the toxicity of state-of-the-art solvents for LPE, with subsequent superb impact on the commercial potential of their technological applications. Moreover, here we have reported for the first time the values of the surface tension, Hansen solubility parameter, and viscosity of the new solvent Rhodiasolv Iris, remained unexplored so far. Such information will be relevant for sustainable processes based on this new green solvent.

2.4 Experimental Section

Materials: WS_2 (CAS Number 12138-09-9), MoS_2 (CAS Number 1317- 33-5), and graphite (CAS

Number 7782-42-5) were bought from SigmaAldrich. Dimethyl 2-methylglutarate (Rhodiasolv Iris) was provided by Rhodiasolv, Solvay Novecare, Paris.

Exfoliation of van der Waals Crystals: 0.04 g of powder of WS_2, MoS_2, and graphite were dispersed in 45 mL Rhodiasolv Iris and sonicated for 4 h in bath sonicator in a thermostat bath to avoid undesired temperature increase ($T \leq 24$ °C). To eliminate Iris, various centrifuges were performed. After a first centrifuge at 5000 rpm, supernatant was cast off and replaced with comparable quantity of ethanol. Then, a couple of further centrifuges were carried out to eliminate solvent residuals, with a final centrifuge at 1000 rpm to separate thinner flakes from thick and unexfoliated material. Conclusively, the supernatant was taken for spectroscopic and microscopic analyses.

Characterization: STEM investigation was performed with a JEOL ARM200F Cs-corrected microscope. Field Emission Scanning Electron Microscope experiments were performed with Gemini SEM 500, at an accelerating voltage of 2 kV. AFM measurements were performed with a Nanosurf NaioAFM instrument, using the Dynamic Force configuration with a dynamic mode cantilever. Used tips had a spring constant of 48 N m^{-1} and resonance frequency of 190 kHz. UV–VIS absorption was measured with spectrometer by Perkin Elmer (Lambda 750). XPS measurements were carried out with a PHI 1257 spectrometer with a monochromatic Al Kα source (h_v = 1486.6 eV). The experimental resolution was 0.3 eV. XRD experiments were performed at Instituto de Ciencia de Materiales de Barcelona of Consejo Superior de Investigaciones Científicas (CSIC) (ICMAB-CSIC), Barcelona, Spain using a point detector in θ−2θ configuration using a Bruker-AXS (model A25 D8 Discover).

References

[1] X. Ren, Y. Tian, F. Shaik, J. Yang, R. Liu, K. Guo, B. Jiang. An Efficient Electrocatalyst Based on Vertically Aligned Heteroatom(B/N/P/O/S)-Doped Graphene Array Integrated with FeCoNiP Nanoparticles for Overall Water Splitting. *Adv. Sustainable Syst.* 2022, **6**, 2100436. 10.1002/adsu.202100436

[2] A. Anouar, R. García-Aboal, P. Atienzar, A. Franconetti, N. Katir, A. El Kadib, A. Primo, H. Garcia. Remarkable Activity of 002 Facet of Ruthenium Nanoparticles Grown on Graphene Films on the Photocatalytic CO_2 Methanation. *Adv. Sustainable Syst.* 2022, **6**, 2100487. 10.1002/adsu.202100487

[3] K. Sathiyan, A. Lal, A. Borenstein. Laser Processed Magnetite Nanoparticles Embedded on rGO Composites for Efficient Electrocatalytic Oxygen Evolution Reaction. *Adv. Sustainable Syst.* 2022, **6**, 2200076. 10.1002/adsu.202200076

[4] J. S. Arya Nair, S. Saisree, K. Y. Sandhya. Ultra-Rapid Removal of Pb(II) Ions by a Nano-MoS2 Decorated Graphene Aided by the Unique Combination of Affinity and Electrochemistry. *Adv. Sustainable Syst.* 2022, 2200039.

10.1002/adsu.202200039

[5] M. Y. Yu, C. Li, W. Li, P. Min. Reduced Graphene Oxide Decorated Cellulose Acetate Filter Evaporators for Highly Efficient Water Evaporation and Purification Driven by Solar Energy and Environmental Energy. *Adv. Sustainable Syst.* 2022, **6**, 2200023. 10.1002/adsu.202200023

[6] M. Reina, A. Scalia, G. Auxilia, M. Fontana, F. Bella, S. Ferrero, A. Lamberti. Boosting Electric Double Layer Capacitance in Laser-Induced Graphene-Based Supercapacitors. *Adv. Sustainable Syst.* 2022, **6**, 2100228. 10.1002/adsu.202100228

[7] Y. Wang, L. Wang, X. Zhang, X. Liang, Y. Feng, W. Feng. Two-dimensional nanomaterials with engineered bandgap: Synthesis, properties, applications. *Nano Today* 2021, **37**, 101059. 10.1016/j.nantod.2020.101059

[8] D. Gopalakrishnan, D. Damien, M. M. Shaijumon. MoS2 Quantum Dot-Interspersed Exfoliated MoS2 Nanosheets. *ACS Nano* 2014, **8**, 5297. 10.1021/nn501479e

[9] C. Lee, S. Kim, Y. H. Cho. Silk and Paper: Progress and Prospects in Green Photonics and Electronics. *Adv. Sustainable Syst.* 2022, **6**, 2000216. 10.1002/adsu.202000216

[10] D. Jiang, Z. Liu, Z. Xiao, Z. Qian, Y. Sun, Z. Zeng, R. Wang. Flexible electronics based on 2D transition metal dichalcogenides. *J. Mater. Chem. A* 2022, **10**, 89. 10.1039/D1TA06741A

[11] N. Li, J. Ma, Y. Zhang, L. Zhang, T. Jiao. Recent Developments in Functional Nanocomposite Photocatalysts for Wastewater Treatment: A Review. *Adv. Sustainable Syst.* 2022, **6**, 2200106. 10.1002/adsu.202200106

[12] Q. Dai, Z. Liu, L. Huang, C. Wang, Y. Zhao, Q. Fu, A. Zheng, H. Zhang, X. Li. Thin-film composite membrane breaking the trade-off between conductivity and selectivity for a flow battery. *Nat. Commun.* 2020, **11**, 13. 10.1038/s41467-019-13704-2

[13] Z. Xiao, X. Gan, T. Zhu, D. Lei, H. Zhao, P. Wang. Activating the Basal Planes in 2H-MoTe2 Monolayers by Incorporating Single-Atom Dispersed N or P for Enhanced Electrocatalytic Overall Water Splitting. *Adv. Sustainable Syst.* 2022, **6**, 2100515. 10.1002/adsu.202100515

[14] X. Pang, S. Xue, T. Zhou, M. Qiao, H. Li, X. Liu, Q. Xu, G. Liu, W. Lei. Noble Metal-Free Heterojunction of Ultrathin Ti3C2 MXene/WO3 for Boosted Visible-Light-Driven Photoreactivity. *Adv. Sustainable Syst.* 2022, 2100507. 10.1002/adsu.202100507

[15] Y. Wang, F. Zhao, Y. Wang, Y. Zhang, Y. Shen, Y. Feng, W. Feng. Broadband self-powered photoelectrochemical photodetector based on Te/Se heterostructure nanocomposites. *Compos. Commun.* 2022, **32**, 101175. 10.1016/j.coco.2022.101175

[16] Z. Bai, D. Zhang, Y. Guo, Y. Yang, H. Yan, Y. Wang, J. Cheng, P. K. Chu, H. Pang, Y. Luo. Hierarchical Cobalt-Nickel Double Hydroxide Arrays Assembled on Naturally Sedimented Ti3C2Tx for High-Performance Flexible Supercapacitors. *Adv. Sustainable Syst.* 2022, **6**, 2100371. 10.1002/adsu.202100371

[17] Y. Xu, M. Peng, K. Zhang, L. Wang, J. Chen, T. Hu, K. Yuan. From Crystalline to Partially Amorphous: A Facile Strategy toward Sulfur Vacancy-Enriched CoNi2S4 Nanosheets with Improved Supercapacitor Performance. *Adv. Sustainable Syst.* 2022, **6**, 2100414. 10.1002/adsu.202100414

[18] W. Han, Z. Wu, Y. Li, Y. Wang. Graphene family nanomaterials (GFNs) promising materials for antimicrobial coating and film: A review. *Chem. Eng. J. (Lausanne)* 2019, **358**, 1022. 10.1016/j.cej.2018.10.106

[19] V. Galstyan, A. Moumen, G. W. C. Kumarage, E. Comini. Progress towards chemical gas sensors: Nanowires

and 2D semiconductors. *Sens. Actuators, B* 2022, **357**, 131466. 10.1016/j.snb.2022.131466

[20] S. Xiao, X. Zhao, S. Liu, Y. Xue, G. Li, J. Yang. rGO-CuOx Composites Reduced by Solid-Phase Microwave Thermal Shock for High-Efficient Seawater Desalination and Purification. *Adv. Sustainable Syst.* 2022, **6**, 2100500. 10.1002/adsu.202100500

[21] R. Zha, T. Shi, L. He, M. Zhang. Chemistry and Nanotechnology-Oriented Strategies toward Nanocellulose for Human Water Treatment. *Adv. Sustainable Syst.* 2022, **6**, 2100302. 10.1002/adsu.202100302

[22] E. Baigorria, L. F. Fraceto. Biopolymer-Nanocomposite Hybrid Materials as Potential Strategy to Remove Pesticides in Water: Occurrence and Perspectives. *Adv. Sustainable Syst.* 2022, **6**, 2100243. 10.1002/adsu.202100243

[23] N. Kumar, R. Salehiyan, V. Chauke, O. J. Botlhoko, K. Setshedi, M. Scriba, M. Masukume, S. S. Ray. Top-down synthesis of graphene: A comprehensive review. *FlatChem* 2021, **27**, 100224. 10.1016/j.flatc.2021.100224

[24] A. Zavabeti, A. Jannat, L. Zhong, A. A. Haidry, Z. Yao, J. Z. Ou. Two-Dimensional Materials in Large-Areas: Synthesis, Properties and Applications. *Nano-Micro Lett.* 2020, **12**, 66. 10.1007/s40820-020-0402-x

[25] L. Ottaviano, S. Palleschi, F. Perrozzi, G. D'Olimpio, F. Priante, M. Donarelli, P. Benassi, M. Nardone, M. Gonchigsuren, M. Gombosuren, A. Lucia, G. Moccia, O. A. Cacioppo. Mechanical exfoliation and layer number identification of MoS_2 revisited. *2D Mater.* 2017, **4**, 045013. 10.1088/2053-1583/aa8764

[26] K. Chen, L. Shi, Y. Zhang, Z. Liu. Scalable chemical-vapour-deposition growth of three-dimensional graphene materials towards energy-related applications. *Chem. Soc. Rev.* 2018, **47**, 3018. 10.1039/C7CS00852J

[27] Q. Ji, Y. Zhang, Y. Zhang, Z. Liu. Chemical vapour deposition of group-VIB metal dichalcogenide monolayers: engineered substrates from amorphous to single crystalline. *Chem. Soc. Rev.* 2015, **44**, 2587. 10.1039/C4CS00258J

[28] J. Qu, B.-W. Li, Y. Shen, S. Huo, Y. Xu, S. Liu, B. Song, H. Wang, C. Hu, W. Feng. Evaporable Glass-State Molecule-Assisted Transfer of Clean and Intact Graphene onto Arbitrary Substrates. *ACS Appl. Mater. Interfaces* 2019, **11**, 16272. 10.1021/acsami.8b21946

[29] S. Wang, A. Robertson, J. H. Warner. Atomic structure of defects and dopants in 2D layered transition metal dichalcogenides. *Chem. Soc. Rev.* 2018, **47**, 6764. 10.1039/C8CS00236C

[30] M. Chen, R. C. Haddon, R. Yan, E. Bekyarova. Advances in transferring chemical vapour deposition graphene: a review. *Mater. Horiz.* 2017, **4**, 1054. 10.1039/C7MH00485K

[31] X. Yang, M. Yan. Removing contaminants from transferred CVD graphene. *Nano Res.* 2020, **13**, 599. 10.1007/s12274-020-2671-6

[32] X. Zheng, H. Cong, T. Yang, K. Ji, C. Wang, M. Chen. High-efficiency 2D nanosheet exfoliation by a solid suspension-improving method. *Nanotechnology* 2022, **33**, 185602. 10.1088/1361-6528/ac4b7c

[33] J. Shen, Y. He, J. Wu, C. Gao, K. Keyshar, X. Zhang, Y. Yang, M. Ye, R. Vajtai, J. Lou. Liquid Phase Exfoliation of Two-Dimensional Materials by Directly Probing and Matching Surface Tension Components. *Nano Lett.* 2015, **15**, 5449. 10.1021/acs.nanolett.5b01842

[34] M. Wang, X. Xu, Y. Ge, P. Dong, R. Baines, P. M. Ajayan, M. Ye, J. Shen. Surface Tension Components Ratio: An Efficient Parameter for Direct Liquid Phase Exfoliation. *ACS Appl. Mater. Interfaces* 2017, **9**, 9168. 10.1021/acsami.6b16578

[35] Y. Xu, H. Cao, Y. Xue, B. Li, W. Cai. Liquid-Phase Exfoliation of Graphene: An Overview on Exfoliation Media, Techniques, and Challenges. *Nanomaterials* 2018, **8**, 942. 10.3390/nano8110942

[36] K. Sitarek, J. Stetkiewicz. Assessment of reproductive toxicity and gonadotoxic potential of N-methyl-2-pyrrolidone in male rats. *Int. J. Occup. Environ. Health* 2008, **21**, 73. 10.2478/v10001-008-0006-z

[37] Y. Yang, H. Hou, G. Zou, W. Shi, H. Shuai, J. Li, X. Ji. Electrochemical exfoliation of graphene-like two-dimensional nanomaterials. *Nanoscale* 2019, **11**, 16. 10.1039/C8NR08227H

[38] A. Llevot, E. Grau, S. Carlotti, S. Grelier, H. Cramail. Dimerization of abietic acid for the design of renewable polymers by ADMET. *Eur. Polym. J.* 2015, **67**, 409. 10.1016/j.eurpolymj.2014.10.021

[39] F. Bozso, P. Avouris. Alkali co-adsorption and surface coverage effects on electron-stimulated desorption (ESD): CO and NO on Ni(111). *Chem. Phys. Lett.* 1986, **125**, 531. 10.1016/0009-2614(86)87093-2

[40] A. O'Neill, U. Khan, P. N. Nirmalraj, J. Boland, J. N. Coleman. Graphene Dispersion and Exfoliation in Low Boiling Point Solvents. *J. Phys. Chem. C* 2011, **115**, 5422. 10.1021/jp110942e

[41] X. Zhang, A. C. Coleman, N. Katsonis, W. R. Browne, B. J. Van Wees, B. L. Feringa. Dispersion of graphene in ethanol using a simple solvent exchange method. *Chem. Commun.* 2010, **46**, 7539. 10.1039/C0CC02688C

[42] F. Li, M. Xue, X. Zhang, L. Chen, G. P. Knowles, D. R. MacFarlane, J. Zhang. Advanced Composite 2D Energy Materials by Simultaneous Anodic and Cathodic Exfoliation. *Adv. Energy Mater.* 2018, **8**, 1702794. 10.1002/aenm.201702794

[43] Z. Y. Xia, S. Pezzini, E. Treossi, G. Giambastiani, F. Corticelli, V. Morandi, A. Zanelli, V. Bellani, V. Palermo. Graphene: The Exfoliation of Graphene in Liquids by Electrochemical, Chemical, and Sonication-Assisted Techniques: A Nanoscale Study. *Adv. Funct. Mater.* 2013, **23**, 4756. 10.1002/adfm.201370188

[44] Z. Zeng, Z. Yin, X. Huang, H. Li, Q. He, G. Lu, F. Boey, H. Zhang. Single-Layer Semiconducting Nanosheets: High-Yield Preparation and Device Fabrication. *Angew. Chem.* 2011, **50**, 11093. 10.1002/anie.201106004

[45] P. He, C. Zhou, S. Tian, J. Sun, S. Yang, G. Ding, X. Xie, M. Jiang. Urea-assisted aqueous exfoliation of graphite for obtaining high-quality graphene. *Chem. Commun.* 2015, **51**, 4651. 10.1039/C5CC00059A

[46] M. Lotya, Y. Hernandez, P. J. King, R. J. Smith, V. Nicolosi, L. S. Karlsson, F. M. Blighe, S. De, Z. Wang, I. McGovern. Liquid Phase Production of Graphene by Exfoliation of Graphite in Surfactant/Water Solutions. *J. Am. Chem. Soc.* 2009, **131**, 3611. 10.1021/ja807449u

[47] H. J. Salavagione, J. Sherwood, V. Budarin, G. Ellis, J. Clark, P. Shuttleworth. Identification of high-performance solvents for the sustainable processing of graphene. *Green Chem.* 2017, **19**, 2550. 10.1039/C7GC00112F

[48] https://echa.europa.eu/de/registration-dossier/-/registered-dossier/2181/9.

[49] J. Li, M. C. Lemme, M. Östling. Inkjet Printing of 2D Layered Materials. *ChemPhysChem* 2014, **15**, 3427. 10.1002/cphc.201402103

[50] A. Gugliuzza, A. Politano, E. Drioli. The advent of graphene and other two-dimensional materials in membrane science and technology. *Curr. Opin. Chem. Eng.* 2017, **16**, 78. 10.1016/j.coche.2017.03.003

[51] G. D. Arend, K. Rezzadori, L. S. Soares, J. C. C. Petrus. Performance of nanofiltration process during concentration of strawberry juice. *J. Food Sci. Technol.* 2019, **56**, 2312. 10.1007/s13197-019-03659-z

[52] Y. Hernandez, V. Nicolosi, M. Lotya, F. M. Blighe, Z. Sun, S. De, I. T. McGovern, B. Holland, M. Byrne, Y. K. Gun'ko, J. J. Boland, P. Niraj, G. Duesberg, S. Krishnamurthy, R. Goodhue, J. Hutchison, V. Scardaci, A. C. Ferrari, J. N. Coleman. High-yield production of graphene by liquid-phase exfoliation of graphite. *Nat. Nanotechnol.* 2008, **3**, 563. 10.1038/nnano.2008.215

[53] Y. Hernandez, M. Lotya, D. Rickard, S. D. Bergin, J. N. Coleman. Measurement of Multicomponent Solubility Parameters for Graphene Facilitates Solvent Discovery. *Langmuir* 2009, **26**, 3208. 10.1021/la903188a

[54] S. Halonen, T. Kangas, M. Haataja, U. Lassi. Urea-Water-Solution Properties: Density, Viscosity, and Surface Tension in an Under-Saturated Solution. *Emiss. Control Sci. Technol.* 2017, **3**, 161. 10.1007/s40825-016-0051-1

[55] A. Aghanouri, G. Sun. Prediction of Solubility Behavior of Globular Plant Proteins with Hansen Solubility Parameters: A Conformational Study. *ACS Sustainable Chem. Eng.* 2016, **4**, 2337. 10.1021/acssuschemeng.6b00022

[56] J. Lyklema. The surface tension of pure liquids: Thermodynamic components and corresponding states. *Colloids Surf., A* 1999, **156**, 413. 10.1016/S0927-7757(99)00100-4

[57] J. N. Coleman, M. Lotya, A. O'Neill, S. D. Bergin, P. J. King, U. Khan, K. Young, A. Gaucher, S. De, R. J. Smith, I. V. Shvets, S. K. Arora, G. Stanton, H.-Y. Kim, K. Lee, G. T. Kim, G. S. Duesberg, T. Hallam, J. J. Boland, J. J. Wang, J. F. Donegan, J. C. Grunlan, G. Moriarty, A. Shmeliov, R. J. Nicholls, J. M. Perkins, E. M. Grieveson, K. Theuwissen, D. W. McComb, P. D. Nellist. Two-dimensional nanosheets produced by liquid exfoliation of layered materials, *Science* 2011, **331**, 568. 10.1126/science.1194975

[58] G. Bianca, M. I. Zappia, S. Bellani, Z. k. Sofer, M. Serri, L. Najafi, R. Oropesa-Nuñez, B. Martín-García, T. s. Hartman, L. Leoncino. Liquid-Phase Exfoliated GeSe Nanoflakes for Photoelectrochemical-Type Photodetectors and Photoelectrochemical Water Splitting, *ACS Appl. Mater. Interfaces* 2020, **12**, 48598. 10.1021/acsami.0c14201?ref=pdf

[59] A. Splendiani, L. Sun, Y. Zhang, T. Li, J. Kim, C. Y. Chim, G. Galli, F. Wang, *Nano Lett.* 2010, **10**, 1271. 10.1021/nl903868w

[60] K. F. Mak, C. Lee, J. Hone, J. Shan, T. F. Heinz. Atomically Thin MoS2: A New Direct-Gap Semiconductor, *Phys. Rev. Lett.* 2010, **105**, 136805. 10.1103/PhysRevLett.105.136805

[61] K. Wang, Y. Feng, C. Chang, J. Zhan, C. Wang, Q. Zhao, J. N. Coleman, L. Zhang, W. J. Blau, J. Wang, Broadband ultrafast nonlinear absorption and nonlinear refraction of layered molybdenum dichalcogenide semiconductors, *Nanoscale* 2014, 6, 10530. 10.1039/C4NR02634A

[62] P. Joensen, E. Crozier, N. Alberding, R. Frindt, A study of single-layer and restacked MoS2 by X-ray diffraction and X-ray absorption spectroscopy, *J. Phys. C* 1987, **20**, 4043. 10.1088/0022-3719/20/26/009

[63] M. Donarelli, F. Bisti, F. Perrozzi, L. Ottaviano, Tunable sulfur desorption in exfoliated MoS2 by means of thermal annealing in ultra-high vacuum, *Chem. Phys. Lett.* 2013, **588**, 198. 10.1016/j.cplett.2013.10.034

[64] A. Di Paola, L. Palmisano, A. Venezia, V. Augugliaro, Coupled Semiconductor Systems for Photocatalysis. Preparation and Characterization of Polycrystalline Mixed WO3/WS2 Powders, *J. Phys. Chem. B* 1999, **103**, 8236. 10.1021/jp9911797

[65] K. Wong, X. Lu, J. Cotter, D. Eadie, P. Wong, K. Mitchell, Surface and friction characterization of MoS2 and WS2 third body thin films under simulated wheel/rail rolling–sliding contact, *Wear* 2008, **264**, 526. 10.1016/j.wear.2007.04.004

[66] A. Shpak, A. Korduban, L. Kulikov, T. Kryshchuk, N. Konig, V. Kandyba, XPS studies of the surface of nanocrystalline tungsten disulfide, *J. Electron Spectrosc. Relat. Phenom.* 2010, **181**, 234. 10.1016/j.elspec.2010.05.030

[67] N. V. Alov, XPS study of MoO3 and WO3 oxide surface modification by low-energy Ar+ ion bombardment, *Phys. Status Solidi C* 2015, **12**, 263. 10.1002/pssc.201400108

[68] Z. Li, R. J. Young, C. Backes, W. Zhao, X. Zhang, A. A. Zhukov, E. Tillotson, A. P. Conlan, F. Ding, S. J. Haigh, K. S. Novoselov, J. N. Coleman, Mechanisms of Liquid-Phase Exfoliation for the Production of Graphene *ACS Nano* 2020, **14**, 10976. 10.1021/acsnano.0c03916

[69] R. Bari, D. Parviz, F. Khabaz, C. D. Klaassen, S. D. Metzler, M. J. Hansen, R. Khare, M. J. Green, Liquid phase

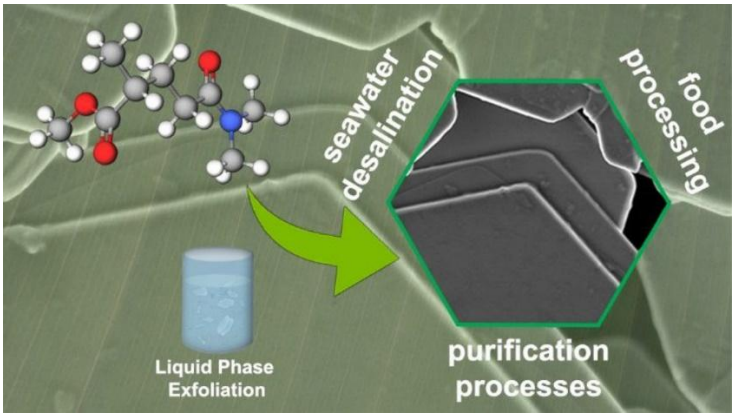
exfoliation and crumpling of inorganic nanosheets *Phys. Chem. Chem. Phys.* 2015, **17**, 9383. 10.1039/c5cp00294j
[70] S. Biccai, S. Barwich, D. Boland, A. Harvey, D. Hanlon, N. McEvoy, J. N. Coleman, Exfoliation of 2D materials by high shear mixing *2D Mater.* 2018, **6**, 015008. 10.1088/2053-1583/aae7e3
[71] Y. Tominaga, K. Sato, D. Shimamoto, Y. Imai, Y. Hotta, Wet-jet milling-assisted exfoliation of h-BN particles with lamination structure *Ceram. Int.* 2015, **41**, 10512. 10.1016/j.ceramint.2015.04.143

Chapter 3

The Quest for Green Solvents for the Sustainable Production of Nanosheets of Two-Dimensional (2D) Materials, a Key Issue in the Roadmap for the Ecology Transition in the Flatland

Keywords: Cyrene; Polarclean; Iris; green chemistry; 2D materials; liquid-phase exfoliation

GRAPHICAL ABSTRACT



Contents

Abstract

3.1 Challenges and Opportunities in the Scalable Production of High-Quality 2D Materials

3.2 Materials and Methods

3.3 Results and Discussion

3.3.1 Solvent Properties and Emerging Methods for Efficient Liquid Phase Exfoliation

3.3.2 Evaluation of Green Solvents: Performance, Toxicity, and Applicability

3.3.3 Microscopic and Structural Characterization of 2D Nanosheets

3.3.4 Spectroscopic Characterization of Defects and Chemical Stability

3.4 Conclusions

References

This chapter has been published as:

Occhiuzzi J., Politano G.G, D'Olimpio G., Politano A., The Quest for Green Solvents for the sustainable Production of Nanosheets of Two-Dimensional (2D) Materials, a Key Issue in the Roadmap for the Ecology Transition in the Flatland, Molecules 2023, 28(3), 1484; https://doi.org/10.3390/molecules28031484

Abstract

The recent advent of two-dimensional (2D) materials has had a ground-breaking impact on science and technology. To exploit in technology their unique thickness-dependent physicochemical properties, the large-scale production of 2D materials is mandatory, but it represents an open challenge still due to various pitfalls and severe limitations including the toxicity of state-of-the-art solvents. Thus, liquid-phase exfoliation based on green and bioderived solvents represents an ideal methodology for massive production. This is particularly crucial for introducing 2D materials in technological applications such as the production of drinking water and agri-food industrial processes. Here, we assessed the production of 2D nanosheets (specifically, graphene, WS_2, MoS_2) with liquid-phase exfoliation assisted by eco-friendly solvents, with a comparative evaluation of green solvents in terms of the yield and, moreover, the aspect ratio, defectivity, and crystalline quality of the produced nanosheets. In particular, we focus on the most promising green solvents in terms of the yield and the crystalline quality of the produced nanosheets: Polarclean (Rhodiasolv® PolarClean), Iris (Rhodiasolv® Iris), and Cyrene (a green dipolar aprotic solvent prepared by pyrolysis of cellulose-containing biomass), which were compared with acetone/water mixtures, isopropyl alcohol (IPA), triethanolamine (TEA), aqueous solutions of urea, and an ethanol/water mixture as well as two toxic solvents largely used for the production of 2D nanosheets: N-methyl-2-pyrrolidone (NMP) and N, N-dimethylformamide (DMF). Remarkably, the density of defects was particularly low in the liquid-phase exfoliation with Polarclean, as indicated by the Raman spectrum of graphene, with the I(D)/I(G) ratio below 0.1. Furthermore, Polarclean and Iris also enable ink-jet printing with functional inks of 2D materials based on green solvents due to their low dynamic viscosity at room temperature.

3.1 Challenges and Opportunities in the Scalable Production of High-Quality 2D Materials

2D materials represent a promising platform for technology [1-7] because of their unique physicochemical properties associated with the atomic thickness [8-20]. This implies enormous versatility in various fields, ranging from electrochemical energy storage devices, sensing, photonics, optoelectronics, and energy storage/production [21-25]. However, the industrial exploitation of 2D materials implies the need to achieve the sustainable large-scale production of 2D materials with high crystalline quality and unaltered electronic properties [26,27]. As of mid-2022, the global graphene and graphene oxide installed capacity undoubtedly exceeds 12,000 tonnes per year, but utilisation is low as the orders lag significantly behind.

Taking China's graphene industry as a case-study example, with the production volume of 2000

tonnes per year of graphene powders and 3.5 million m^2 per year of graphene films [28], its capability for economically scalable production is absolutely satisfactory. The quality of the graphene products, nevertheless, differs tremendously in practice, as it is extremely dependent on the graphene sources, manufacturing techniques, and fabrication condition monitoring.

Evident inconsistencies persist in the flake size and number of layers of commercially available graphene samples, along with considerable differences in the defect density and impurity content. These wide variations in quality have resulted in exaggerated reports on the applications of graphene and complaints about unrepeatable performance.

While mechanical exfoliation suffers from non-scalable processes with scarce reproducibility [29], chemical vapour deposition necessitates specific substrates allowing for epitaxial growth [30-36], with consequent complications related to the etching of 2D layers from the substrate [37], resulting in flakes with degraded crystalline quality with high amounts of defects and metallic impurities [38] and/or polymer residuals from the transfer process, altering the physicochemical properties of transferred flakes of 2D materials [39]. The removal of the substrate is also a challenging issue for the preparation of graphene by Si sublimation from the SiC substrate [40].

While the bottom–up synthesis is evidently inadequate for massive production, the top–down approach, implying exfoliation from parental bulk crystals, is in principle more suitable for scale up [41-43]. However, one should consider that mechanical exfoliation fails in reproducibility and scalability. On the other hand, liquid-phase exfoliation (LPE) [44,45] represents a viable technique able to overcome such difficulties. Definitely, LPE is suitable for scaling up by ensuring the massive production of highly crystalline 2D materials [46]. However, the quest of the most suitable solvent for the process remains an open issue to date. Currently, the most commonly used solvents for LPE are N-methyl-2-pyrrolidone (NMP) and N, N-dimethylformamide (DMF), due to the strong compatibility of their values of surface tension and of the Hansen solubility parameters (HSP) with surface energy and HSP for graphite and other 2D materials (Table 2). Unfortunately, NMP and DMF have recently been listed as extremely hazardous substances for toxicity issues, with subsequent restrictions on their use in both Europe and the United States of America [46-48]. Accordingly, the scientific community is engaged in a quest for environmentally friendly solvents that are capable of replacing NMP and DMF for the LPE of 2D materials, with appropriate effectiveness.

3.2 Materials and Methods

Materials: WS_2 (CAS number 12138-09-9), MoS_2 (CAS number 1317-33-5), and graphite (CAS

number 7782-42-5) were purchased from Sigma-Aldrich. Absolute ethanol and N-methyl-2-pyrrolidone (NMP) were purchased from commercial chemical suppliers. Methyl-5-(dimethylamino)-2-methyl-5-oxopentanoate (Rhodiasolv Polarclean) and dimethyl 2-methylglutarate (Rhodiasolv Iris) were provided by Rhodiasolv, Solvay Novecare, Paris. Exfoliation: The preparation of the methodology for the exfoliation of the layered materials was performed by considering 0.05 g of the powders (WS_2, MoS_2, and graphite) dispersed in 40 mL of the solvents under investigation (NMP, Rhodiasolv Polarclean, Rhodiasolv Iris).

The solution was sonicated for 4 h in a sonicator bath (Labsonic LBD2 working at 40 kHz) with a thermostat built into it to prevent excessive temperature rise (set not to exceed 25 °C). Next, it is necessary to completely remove the solvent used from the solution. This mechanism is accomplished by numerous centrifugations.

The sequence of centrifugations started with an initial centrifugation at 5000 rpm for 20 min, at the end of which the supernatant was discarded and replaced with the same amount of ethanol. The second step saw further centrifugations aimed at removing the residue of the solvent used, with a final centrifugation at 1000 rpm.

This last centrifugation was performed to try to separate the thinner flakes from the thicker part of the material that had not been exfoliated. At the end of this process, the supernatant from the last step was taken for later characterisation.

3.3 Results and Discussion

3.3.1 Solvent Properties and Emerging Methods for Efficient Liquid Phase Exfoliation

Among the ideal characteristics that the solvent must have, it is important to consider their values of polarity, surface tension, viscosity, and toxicity [49]. In particular, a suitable solvent for LPE should minimize the energy input required to overcome the van der Waals forces for effective sheet separation [50]. This corresponds to the minimisation of the enthalpy of mixing per unit of volume (ΔH/V). In turn, it is related to the Helmholtz energy of solvent (F_{solv}), the thickness of the flakes ($T_{layered}$), the free Helmholtz energy of layered materials (Flayered), and the volume fraction (ϕ) through [51,52]:

$$\frac{\Delta H}{V} \sim \frac{2}{T_{layered}} \left(\sqrt{F_{solv}} - \sqrt{F_{layered}}\right)^2 \phi \quad (1)$$

with

$$F_{layered} = (\sigma_s - T\, S_{Sur}) \quad (2)$$

where σ_s is the surface energy and S_{Sur} is the surface entropy.

Therefore, matching the surface tensions of the solvent and layered materials (already showed in the in Chapter 2) is crucial to achieve an efficient LPE. However, another critical issue is related to the dispersibility of the flakes and solvent, which depends on the specific molecular interactions between the solvent and the solute. The evaluation of the dispersibility of both nanosheets and the solvent can be carried out based on the assessment of HSP, which describes the interaction between the solvent and the solute. Precisely, HSP considers the dispersion forces (δ_d), polarity interactions (δ_p), and hydrogen bonds (δ_h), respectively. If the HSP of solvents has comparable values with the solute, the energy cost for their dispersion is minimised.

Volatile organic compounds (VOCs such as isopropyl alcohol and ethanol), although they appear as good alternatives to NMP and DMF, unfortunately, they suffer from insufficient exfoliation yields, which are inevitably halved [54] due to the need to transfer nanosheets from a suspension into NMP [55]. Moreover, their flash temperature is often around 12–13 °C, which could result in being hazardous for industry.

With regard to the possibility of using surfactants in aqueous media [56], most of them are insulating and their residuals [57] are thus detrimental in many applications requiring thermal and electrical conductivity.

Electrochemical exfoliation (both anodic and cathodic) in aqueous electrolytes has emerged as a novel platform for the production of 2D materials [58]. However, for bulk semiconductors or insulators, electrochemical exfoliation is ineffective in breaking the interlayer van der Waals forces without including a conducting additive [59]. Furthermore, reaching the monolayer regime through the electrochemical exfoliation of bulk materials remains a severe hurdle [60]. Another problem is related to the unconventional operational electrochemical conditions, which imply the occurrence of oxygen and hydrogen evolution stimulated by electrochemical polarisation [61]. Finally, electrochemical exfoliation in aqueous electrolytes typically afford flakes of 2D materials with a high number of defects [58,62].

3.3.2 Evaluation of Green Solvents: Performance, Toxicity, and Applicability

Recently, TEA [63] and urea aqueous solutions [64] have been proposed as green alternative media for the LPE of graphene and other layered materials. Regarding TEA, though it shows good results in terms of the flakes' microstructure and dispersion stability, issues related to the yield of the process, and mainly to the chemical modification of flakes induced by possible functionalisation

[65,66] during the process are still open. In addition, the very high dynamic viscosity (605.9 cP at T = 25 °C [67]) precludes the use of such dispersions for the inkjet printing of 2D material-based inks, for which the viscosity range is recommended to be 1–10 cP [68]. On the other hand, aqueous dispersions of urea have shown encouraging results for graphite exfoliation, obtaining high quality flakes. Nevertheless, the low yield of the process (2.4%), evidently related to the significant difference in the surface energy makes urea inappropriate for scalability. Among the various attempts in the literature, the most effective green solvents for the LPE of 2D materials appear to be: (i) dihydrolevoglucosenone (Cyrene, CAS: 53716-82-8) [69]; (ii) methyl-5-(dimethylamino)-2-methyl-5-oxopentanoate (Rhodiasolv Polarclean, CAS: 1174627-68-9) [70]; and (iii) dimethyl 2-methylglutarate (Rhodiasolv Iris, CAS: 33514-22-6) [71] (Figure 3.1).

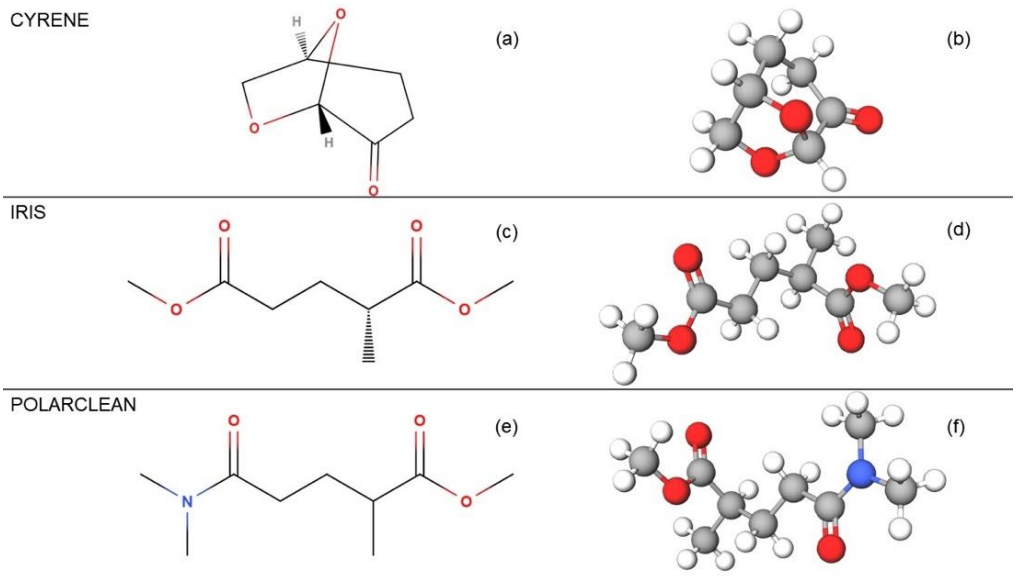


Figure 3.1. *Comparison of the molecular structures of the solvents used: Cyrene, Iris, and Polarclean, whose atomic structures are shown in (a,c,e) plain and (b,d,f) ball-and-stick layouts, respectively.*

Dihydrolevoclucosenone (Cyrene is its market name) is a biomass-derived solvent ($C_6H_8O_3$) has been considered in recent studies [69] to be the most viable substituent to NMP as an organic solvent. It does not exhibit the amide functionality associated with the reproductive toxicity of many of the common dipolar aprotic solvents. This solvent limits the production of corrosive or polluting by-products at the end of its cycle due to the lack of chlorine. In addition, unlike other petrochemical dipolar aprotic solvents, which, on decomposition, tend to release NO_x, Cyrene has a flash point of 108 °C, it is stable, and after biodegradation, it releases only carbon dioxide and water. However, it should be mentioned that Cyrene has an acute toxicity (LD50 > 2000 mg/kg) and aquatic toxicity (EC50 > 100 mg/L), which makes its use for drinking water production

impossible. Moreover, its use in inkjet printing is also impossible because of the high dynamic viscosity (14.5 cP at T = 20 °C).

Polarclean ($C_9H_{17}NO_3$) could represent a more effective candidate for the massive production of 2D materials by LPE, based on results in [70]. It does not show toxicity up to 1000 mg/ (kg day), it is biodegradable, and non-mutagenic, thus being safer than oxygenated solvents such as VOCs. The water solubility of Polarclean is more than 490 g/L under room temperature conditions (25 °C) and it has a melting point at an ambient pressure of 160 °C. Currently, Polarclean is mostly used for the solubilisation of agrochemicals as well as for crop protection and animal nutrition [72]. Recently, the use of Polarclean has been extended to the production of polymeric membranes for ultrafiltration and water desalination for the production of drinking water [73], the synthesis of bio-based aliphatic polyurethanes [74], the dimerisation of abietic acid [75], and for copper-catalysed azide– alkyne cycloaddition [76].

Polarclean is absolutely compatible for use in drinking water production or for the agrifood industry. Moreover, its dynamic viscosity of 9.78 cP (at T = 23 °C) makes it suitable for ink-jet printing, contrary to Cyrene.

Another promising eco-friendly solvent could be Iris ($C_8H_{14}O_4$), considering the very recent findings [71]. In the previous chapter, Iris has an excellent safety profile: it is nontoxic, biodegradable, non-carcinogenic, and non-irritating. This solvent has the lowest of the toxicity levels investigated; in fact, its dosage can be as high as 2000 mg/ (kg day) without any detectable toxicity. The enormous potential of this solvent also lies in its flash point being as low as 90.8 °C, which reduces the flammability risks, and moreover, facilitates the removal of the solvent by evaporation. Its solubility in water is greater than 25 g/L at a temperature of 23 °C. With a dynamic viscosity value as low as 2.85 cP at 20 °C, it suitable for use in inkjet printing, like for Polarclean. Table 3 reports the density, the boiling point, and the dynamic viscosity at room temperature of the various solvents used for LPE.

Table 3.1. *Density, boiling point, and dynamic viscosity at 25 ◦C for NMP, DMF, IPA, acetone, ethanol, aqueous urea solutions, Cyrene, Polarclean, and Iris.*

Solvent	Density [g/cm^3]	Boiling Point [°C]	Dynamic Viscosity at 20 °C [cP]
NMP	1.03	202	1.66
DMF	0.94	153	0.92
IPA	0.78	82	2.01
Acetone	0.78	56	0.32

Ethanol	0.79	78	1.09
Urea 30% in H_2O	1.32	135	1.40
TEA	1.13	335	404
Cyrene	1.25	226	14.5
Polarclean	1.04	280	9.78
Iris	1.05	222	2.85

3.3.3 Microscopic and Structural Characterization of 2D Nanosheets

Graphite, MoS_2, and WS_2 were selected as representative layered materials and the quality of the nanosheets of the 2D materials produced by LPE with a specific solvent was assessed. Their lateral size were evaluated by electron microscopies such as scanning electron microscopy (SEM) and transmission electron microscopy, TEM), the thickness checked by atomic force microscopy, (AFM) of the nanosheets of the same set of layered materials: graphite, MoS_2, and WS_2. Figure 3.2 shows the microscopical images and statistical analysis to assess the lateral size of flakes produced with LPE assisted by Polarclean and Iris. Remarkably, NMP-assisted LPE resulted in the formation of flakes with sharp edges and defined angles (similarly to the case of Polarclean), with an average lateral size of around 3–4 nm, which emerged from the analysis of the distribution (Figure 3.2 f). However, the thickness analysis by AFM measurements revealed the incomplete exfoliation. Definitely, when comparing the collected microscopical images, it was evident that the flakes exfoliated with Polarclean (in the case of WS_2) and Iris (in the case of MoS_2) were thinner (as reported in the published articles [70,71]) than those obtained with NMP with the same experimental procedure.

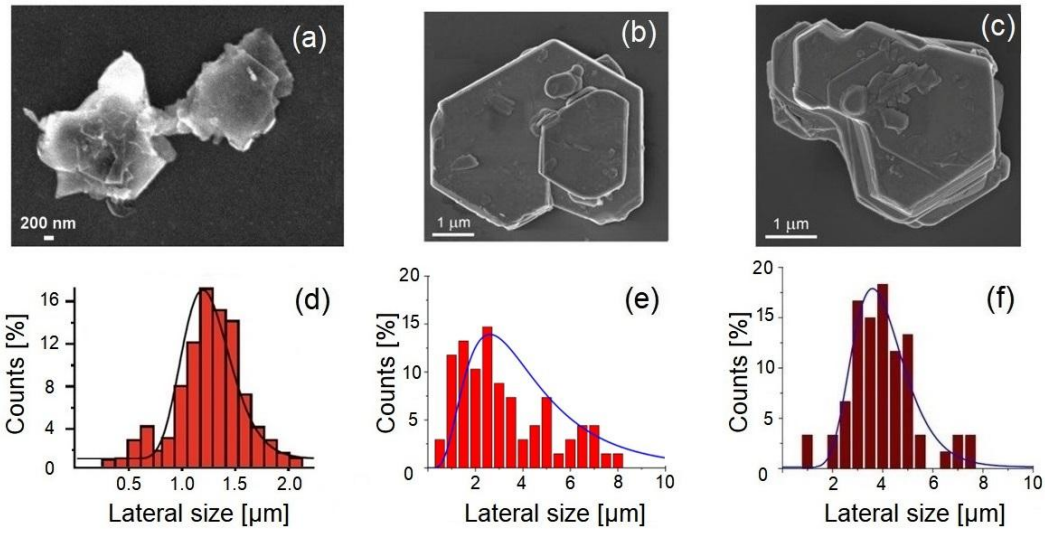


Figure 3.2. *Comparison of the representative high-resolution SEM images and statistical analysis determined from the images. Exfoliated nanolayers with the LPE of WS_2, assisted by (a) Iris, (b) Polarclean (taken from [70] with permission), (c) NMP. Lateral scale size distribution analysis of WS_2 with (d) Iris, (e) Polarclean (taken from [70] with permission), (f) NMP.*

Remarkably, the use of these innovative green solvents did not alter the electronic properties of 2D materials, as inferred from the UV-Vis absorption spectra in Figure 3.2 (exhibiting excitons for both MoS_2 and WS_2, being 2D semiconductors [70,71]). Repeating the UV-Vis spectra in a timescale of months also enabled us to secure the stability of the produced functional inks.

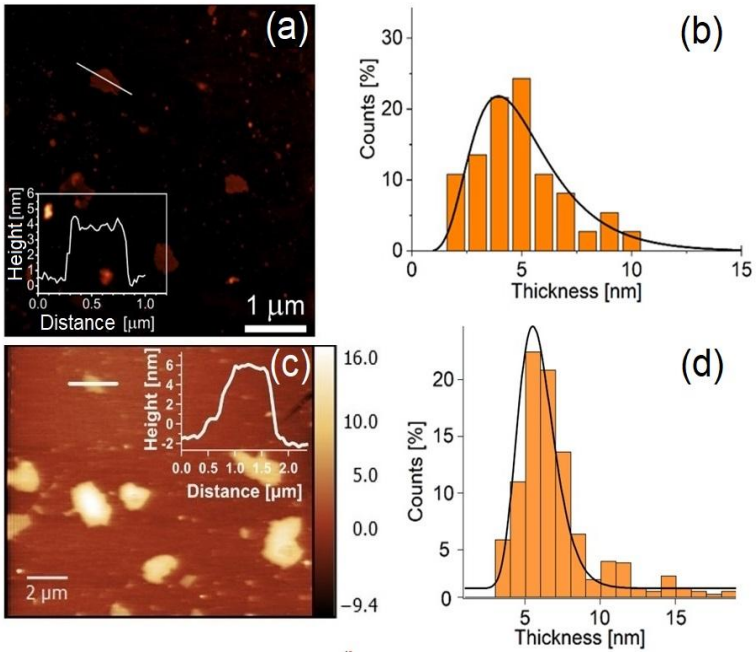


Figure 3.3. *Representative AFM image of MoS_2 flakes in (a) Polarclean (taken from [70] with permission) and (c) Iris. The height profile along the white solid line is reported in the inset. Analysis of the thickness distribution (b,d) was determined from the AFM measurements.*

Figure 3.3 a-d reports the representative AFM measurement and statistical thickness distribution for the case study example of WS_2 produced by LPE with Polarclean and Iris. In both cases, the average thickness was around 5 nm, thus confirming the efficient exfoliation in atomically thin layers.

The performances of Polarclean as an exfoliation medium for 2D materials was directly compared with the case of the most diffuse state-of-the-art solvent (i.e., NMP). Therefore, we also performed LPE under the same operating conditions for NMP. While the lateral size was comparable, the statistical analysis on thickness revealed a bimodal distribution for 2D materials produced by NMP-assisted LPE, which peaked around 4 and 30 nm, corresponding to thin and thick flakes, respectively.

Remarkably, ~85% of flakes exfoliated by Polarclean had a thickness < 5 nm. One can deduce the prevalence of ultrathin flakes (1-3 layers) in Polarclean-assisted LPE. In contrast, the use of NMP in the same processing conditions produced flakes with an ~76% of thickness > 5nm, thus evidencing a largely incomplete exfoliation of the bulk crystal in NMP-assisted LPE.

3.3.4 Spectroscopic Characterization of Defects and Chemical Stability

More insights on the quality of the nanosheets produced by LPE with Polarclean and Iris were provided by X-ray photoelectron spectroscopy (XPS). The core-level spectra of the bulk and exfoliated MoS_2 are shown in Figure 3.4. The Mo-3d core levels are split into J = 5/2 and 3/2 components shifted by 3.1 eV. Specifically, the Mo-3d core levels had two different contributions from pristine (fully coordinated atoms) and defective MoS_2 (with sulphur vacancies), with a binding energy (BE) of 229.8 and 229.2 eV for the J = 5/2 component, respectively. Moreover, a minority component located at lower BE was associated with the presence of the defects due to a redistribution of the charge. Explicitly, the charge localised on the more electronegative sulphur atom, once it is desorbed, is redistributed on the first neighbouring atoms to increase the Coulomb screening effect [77,78]. Particularly, one could note in the Mo-3d spectra the lack of MoO3-derived spectral components, which should be present at a BE of 232.4 eV for the J = 5/2 component [79]. Therefore, one can infer that both Polarclean and Iris do not act as oxidation agents for MoS_2 nanosheets, and congruently, Polarclean/Iris-assisted LPE process do not favour the oxidation of MoS_2 flakes. Concerning the S-2p core levels, they were split in J = 1/2 and 3/2 components shifted by 1.2 eV. Two well-distinct contributions associated with pristine and defective MoS_2 were observed at a BE of 162.5 and 161.5 eV for the J = 3/2 component, respectively, as in previous reports [80-82]. No trace of the sulphur-oxide phases was found, in

contrast to the case of WS_2, for which spectral contributions from both SO_4 and SO_3 exist.

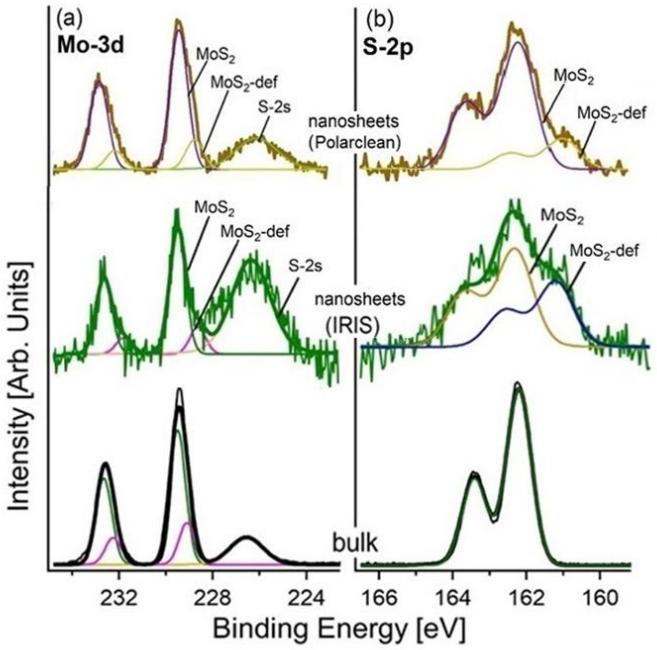


Figure 3.4. *(a) The Mo-3d and (b) S-2p core levels of the bulk MoS_2 and MoS_2 nanosheets produced by LPE with Polarclean (taken from [70] with permission) and Iris. The component at a BE of 226.7 eV in the Mo-3d core level (in panel a) was related to the overlap of the S-2s core level. The photon energy was 1486.6 eV (Al Kα), and the spectra were normalised to the maximum.*

A direct comparison between the XPS spectra of the Iris and Polarclean LPE-MoS_2 only showed a higher presence of defects in the case of the MoS_2 exfoliated with Iris.

Concerning the exfoliation of graphene flakes with Polarclean, amazingly, the distribution of the lateral size reached an average value as high as 10 µm, absolutely one of the largest reported to date for the LPE of nanosheets starting from bulk graphite [12,19]. The related Raman spectrum (Figure 3.5) exhibited D and G bands at 1331 and 1581 cm^{-1}, respectively. One should consider that whereas the G peak resulted from the E_{2g} optical phonon of graphene [83], the D band is produced by breathing modes of six-atom rings and necessitates a defect for its activation [84]. Consequently, the I(D)/I(G) ratio is a generally accepted probe of structural defects in the graphene layer [85]. Outstandingly, in the case of the Polarclean-assisted LPE of graphene, the I(D)/I(G) was 0.07 ± 0.01. Therefore, one can guess a density of defects of only $(8 \pm 2) \cdot 10^9$ cm^{-2}, congruently with the exceptional crystalline order of exfoliated graphene flakes (without indication of defects) in the HR-TEM images in [70]. For the cases of other solvents, the density of defects for graphene exfoliated by LPE was $(6 \pm 2) \cdot 10^{10}$, $(5 \pm 2) \cdot 10^{10}$, $(1.0 \pm 0.3) \cdot 10^{11}$, $(9 \pm 3) \cdot 10^{10}$, $(4 \pm 1) \cdot 10^{10}$, $(2.6 \pm 0.7) \cdot 10^{11}$, $(6 \pm 2) \cdot 10^{10}$, $(7 \pm 2) \cdot 10^{10}$ defects$\cdot cm^{-2}$ with NMP [69,86], Cyrene [69], IPA [87],

DMF [88], acetone/water [89], ethanol/water [90], TEA [63], and aqueous solution of urea [64], respectively. Evidently, graphene flakes exfoliated with Polarclean displayed a density of defects lower by about one order of magnitude compared to LPE assisted by other solvents.

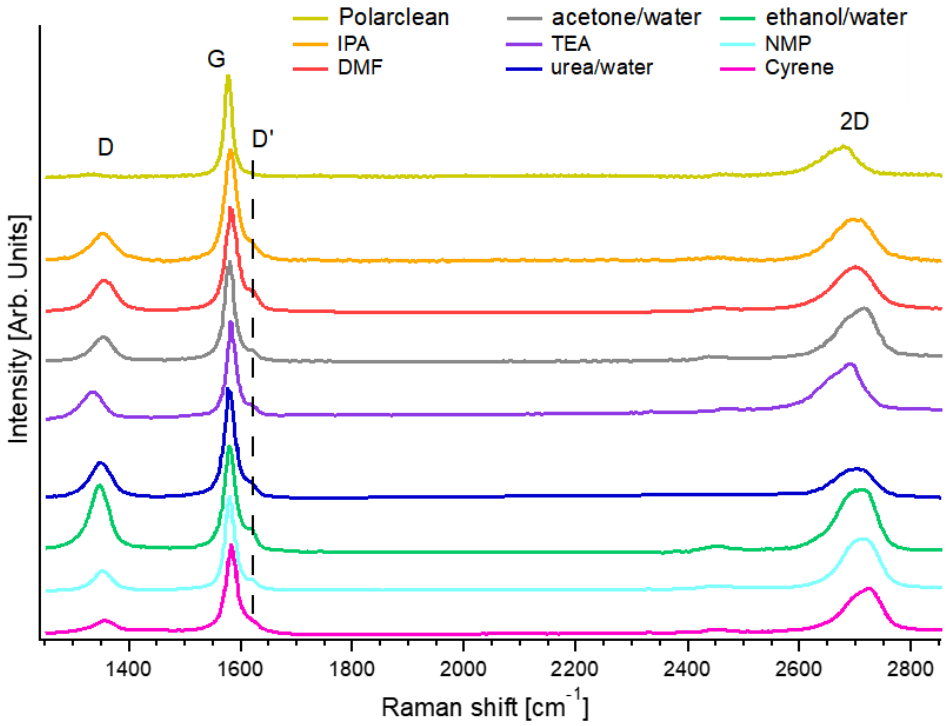


Figure 3.5. *Comparison of the Raman spectrum for graphene exfoliated in the liquid phase with NMP [69], Cyrene [69], IPA [87], DMF [88], acetone/water [89], ethanol/water [90], TEA [63], and aqueous solution of urea [64], and Polarclean [70]. Data were taken from the above-mentioned references.*

The inspection of the intensity of the D′ band could offer further clues on the density of defects. Comparable to the D band, the D′ mode is a double resonance due to the transverse optical (TO) phonons at K or K′, activated by defects, with the difference that it involves an intravalley rather than intervalley process [85]. Notably, the intensity of the D′ band at 1615 cm^{-1} was suppressed for the case of the Polarclean-assisted LPE of graphene, in contrast with the case of other solution processing methods (Figure 3.5).

3.4 Conclusions

Here, we assessed the choice of solvents for LPE for the production of atomically thin layers of van der Waals crystals. The most competitive solvents, both in terms of environmental sustainability and operability, were examined and compared with those that are more widely used, but harmful to human health. The most promising eco-friendly solvents in terms of the yield and

crystalline quality of the produced nanosheets are Polarclean, Iris, and Cyrene. Among these solvents, one can note that the density of defects is exceptionally low in Polarclean-assisted LPE, as inferred by the Raman spectroscopy in graphene, with the I(D)/I(G) ratio of only 0.07. Moreover, Polarclean and Iris also enable ink-jet printing with functional inks of 2D materials based on green solvents.

The superior performances in LPE, together with the absence of any toxicity issue and its biodegradability, make green solvents such as Polarclean and Iris ideal candidates for the sustainable large-scale production of 2D materials. Naturally, they can also replace solvents commonly employed for other processing methods beyond sonication such as shear mixing [91] or wet-jet mill [92], particularly promising for industrial scale up. The efficiency of the green LPE process is crucial in order to combine intrinsic benefits for environmental health and safety with the optimisation of the performance. Undeniably, the introduction of a green solvent for LPE will also expand the growing market of 2D materials towards fields nearly unexplored (e.g., recovery of minerals from seawater, concentration of fruit juices, production of drinking water, etc.) to date, as a result of the toxicity of the state-of-the-art solvents for LPE, with subsequent superb impact on the commercial potential of their technological applications.

References

[1] Gurunlu, B.; Tasdelen-Yucedag, C.; Bayramoglu, M. One Pot Synthesis of Graphene through Microwave Assisted Liquid Exfoliation of Graphite in Different Solvents. *Molecules* **2022**, *27*, 5027. 10.3390/molecules27155027

[2] Sun, X.; Chen, Y.; Liu, K.; Ding, Y.; Zeng, M.; Fu, L. Atomic Scale Materials for Emerging Robust Catalysis. *Small Methods* 2018, *2*, 1800181. 10.1002/smtd.201800181

[3] Mounet, N.; Gibertini, M.; Schwaller, P.; Campi, D.; Merkys, A.; Marrazzo, A.; Sohier, T.; Castelli, I.E.; Cepellotti, A.; Pizzi, G. Two-dimensional materials from high-throughput computational exfoliation of experimentally known compounds. *Nat. Nanotechnol.* **2018**, *13*, 246. 10.1038/s41565-017-0035-5

[4] Kuraganti, V.; Siva, P.; Bar-Ziv, R.; Bar Sadan, M. Incorporating Nb into $MoSe_2$ Nanoflowers for Overall Electrocatalytic Water Splitting. *Isr. J. Chem.* **2022**, *62*, e202100055. 10.1002/ijch.202100055

[5] Kadam, S.R.; Bar-Ziv, R.; Bar-Sadan, M. A cobalt-doped WS_2/WO_3 nanocomposite electrocatalyst for the hydrogen evolution reaction in acidic and alkaline media. *New J. Chem.* **2022**, *46*, 20102–20107. 10.1039/d2nj02687b

[6] Maiti, P.S.; Ghosh, S.; Leitus, G.; Houben, L.; Bar Sadan, M. Oriented Attachment of 2D Nanosheets: The Case of Few-Layer Bi_2Se_3. *Chem. Mater.* **2021**, *33*, 7558–7565, 10.1021/acs.chemmater.1c02707.

[7] Kadam, S.R.; Ghosh, S.; Bar-Ziv, R.; Bar-Sadan, M. Structural Transformation of SnS_2 to SnS by Mo Doping Produces Electro/Photocatalyst for Hydrogen Production. *Chem. Eur. J.* **2020**, *26*, 6679–6685, 10.1002/chem.202000366.

[8] Balakrishnan, P.; Sanij, F.D.; Chang, Z.; Leung, P.K.; Su, H.; Xing, L.; Xu, Q. Nano-Graphene Layer from Facile,

Scalable and Eco-Friendly Liquid Phase Exfoliation Strategy as Effective Barrier Layer for High-Performance and Durable Direct Liquid Alcohol Fuel Cells. *Molecules* **2022**, *27*, 3044, 10.3390/molecules27093044.

[9] Cupolillo, A.; Ligato, N.; Caputi, L.S. Plasmon dispersion in quasi-freestanding graphene on Ni(111). *Appl. Phys. Lett.* **2013**, *102*, 111609, 10.1063/1.4798331.

[10] Xu, S.; Niu, M.; Zhao, G.; Ming, S.; Li, X.; Zhu, Q.; Ding, L.-X.; Kim, M.; Alothman, A.A.; Mushab, M.S.S.; et al. Size control and electronic manipulation of Ru catalyst over B, N co-doped carbon network for high-performance hydrogen evolution reaction. *Nano Res.* **2022,** 10.1007/s12274-022-5250-1.

[11] Cupolillo, A.; Ligato, N.; Caputi, L.S. Two-dimensional character of the interface-π plasmon in epitaxial graphene on Ni(111). *Carbon* **2012**, *50*, 2588–2591, 10.1016/j.carbon.2012.02.017.

[12] Al Taleb, A.; Anemone, G.; Miranda, R.; Farías, D. Characterization of interlayer forces in 2D heterostructures using neutral atom scattering. *2D Mater.* **2018**, *5*, 045002, 10.1088/2053-1583/aacf26.

[13] Jin, X.; Wang, X.; Liu, Y.; Kim, M.; Cao, M.; Xie, H.; Liu, S.; Wang, X.; Huang, W.; Nanjundan, A.K.; et al. Nitrogen and Sulfur Co-Doped Hierarchically Porous Carbon Nanotubes for Fast Potassium Ion Storage. *Small* **2022**, *18*, 2203545, 10.1002/smll.202203545.

[14] Maccariello, D.; Campi, D.; Al Taleb, A.; Benedek, G.; Farías, D.; Bernasconi, M.; Miranda, R. Low-energy excitations of graphene on Ru(0001). *Carbon* **2015**, *93*, 1–10, 10.1016/j.carbon.2015.05.028.

[15] Borca, B.; Castenmiller, C.; Tsvetanova, M.; Sotthewes, K.; Rudenko, A.N.; Zandvliet, H.J.W. Image potential states of germanene. *2D Mater.* **2020**, *7*, 035021, 10.1088/2053-1583/ab96cf.

[16] Socol, M.; Trupina, L.; Galca, A.-C.; Chirila, C.; Stan, G.E.; Vlaicu, A.-M.; Stanciu, A.E.; Boni, A.G.; Botea, M.; Stanculescu, A.; et al. Electro-active properties of nanostructured films of cytosine and guanine nucleobases. *Nanotechnology* **2021**, *32*, 415702, 10.1088/1361-6528/ac10e4.

[17] Borca, B.; Michnowicz, T.; Pétuya, R.; Pristl, M.; Schendel, V.; Pentegov, I.; Kraft, U.; Klauk, H.; Wahl, P.; Gutzler, R.; et al. Electric-Field-Driven Direct Desulfurization. *ACS Nano* **2017**, *11*, 4703–4709, 10.1021/acsnano.7b00612.

[18] Ghosh, B.; Kumar, P.; Thakur, A.; Chauhan, Y.S.; Bhowmick, S.; Agarwal, A. Anisotropic plasmons, excitons, and electron energy loss spectroscopy of phosphorene. *Phys. Rev. B* **2017**, *96*, 035422, 10.1103/PhysRevB.96.035422.

[19] Ghosh, B.; Singh, B.; Prasad, R.; Agarwal, A. Electric-field tunable Dirac semimetal state in phosphorene thin films. *Phys. Rev. B* **2016**, *94*, 205426, 10.1103/PhysRevB.94.205426.

[20] Al Taleb, A.; Farías, D. Phonon dynamics of graphene on metals. *J. Phys. Cond. Matt.* **2016**, *28*, 103005, 10.1088/0953-8984/28/10/103005.

[21] Tang, H.; Chen, C.J.; Huang, Z.; Bright, J.; Meng, G.; Liu, R.S.; Wu, N. Plasmonic hot electrons for sensing, photodetection, and solar energy applications: A perspective. *J. Chem. Phys.* **2020**, *152*, 220901, 10.1063/5.0005334.

[22] Pu, J.; Tan, Y.; Wang, T.; Zhu, X.; Fan, S. Ultrathin Two-Dimensional Fe-Co Bimetallic Oxide Nanosheets for Separator Modification of Lithium-Sulfur Batteries. *Molecules* **2022**, *27*, 7762, 10.3390/molecules27227762.

[23] Boroujerdi, R.; Paul, R. Graphene-Based Electrochemical Sensors for Psychoactive Drugs. *Nanomaterials* **2022**, *12*, 2250, 10.3390/nano12132250.

[24] Iravani, S.; Varma, R.S. MXene-Based Photocatalysts in Degradation of Organic and Pharmaceutical Pollutants. *Molecules* **2022**, *27*, 6939, 10.3390/molecules27206939.

[25] Paone, E.; Miceli, M.; Malara, A.; Ye, G.; Mousa, E.; Bontempi, E.; Frontera, P.; Mauriello, F. Direct Reuse of Spent Lithium-Ion Batteries as an Efficient Heterogeneous Catalyst for the Reductive Upgrading of Biomass-Derived

Furfural. *ACS Sustain. Chem. Eng.* **2022**, *10*, 2275–2281, 10.1021/acssuschemeng.1c08008.

[26] Robinson, J.T.; Schmucker, S.W.; Diaconescu, C.B.; Long, J.P.; Culbertson, J.C.; Ohta, T.; Friedman, A.L.; Beechem, T.E. Electronic hybridization of large-area stacked graphene films. *ACS Nano* **2013**, *7*, 637–644, 10.1021/nn304834p.

[27] Wan, X.; Huang, Y.; Chen, Y. Focusing on energy and optoelectronic applications: A journey for graphene and graphene oxide at large scale. *Acc. Chem. Res.* **2012**, *45*, 598–607, 10.1021/ar200229q.

[28] Lin, L.; Peng, H.; Liu, Z. Synthesis challenges for graphene industry. *Nat. Mater.* **2019**, *18*, 520–524, 10.1038/s41563-019-0341-4.

[29] Yi, M.; Shen, Z. A review on mechanical exfoliation for the scalable production of graphene. *J. Mater. Chem. A* **2015**, *3*, 11700–11715, 10.1039/C5TA00252D.

[30] Cabrero-Vilatela, A.; Weatherup, R.S.; Braeuninger-Weimer, P.; Caneva, S.; Hofmann, S. Towards a general growth model for graphene CVD on transition metal catalysts. *Nanoscale* **2016**, *8*, 2149–2158, 10.1039/C5NR06873H.

[31] Al Taleb, A.; Yu, H.K.; Anemone, G.; Farías, D.; Wodtke, A.M. Helium diffraction and acoustic phonons of graphene grown on copper foil. *Carbon* **2015**, *95*, 731–737, 10.1016/j.carbon.2015.08.110.

[32] Anemone, G.; Climent-Pascual, E.; Yu, H.; Al Taleb, A.; Jimenez-Villacorta, F.; Prieto, C.; Wodtke, A.M.; de Andres, A.; Farias, D. Quality of Graphene on Sapphire: Long-range Order from Helium Diffraction versus Lattice Defects from Raman Spectroscopy. *RSC Adv.* **2016**, *6*, 21235–21245, 10.1039/C5RA27452D.

[33] Cupolillo, A.; Ligato, N.; Osman, S.M.; Caputi, L.S. Carbon K-edge electron-energy-loss near-edge structure in the reflection mode on graphene/Ni(111). *Appl. Phys. Lett.* **2016**, *109*, 161603, 10.1063/1.4965856.

[34] Ligato, N.; Caputi, L.S.; Cupolillo, A. Oxygen intercalation at the graphene/Ni(111) interface: Evidences of non-metal islands underneath graphene layer. *Carbon* **2016**, *100*, 258–264, 10.1016/j.carbon.2016.01.011.

[35] Cupolillo, A.; Ligato, N.; Caputi, L. Low energy two-dimensional plasmon in epitaxial graphene on Ni (111). *Surf. Sci.* **2013**, *608*, 88–91, 10.1016/j.susc.2012.09.018.

[36] Ligato, N.; Cupolillo, A.; Caputi, L.S. Study of the intercalation of graphene on Ni(111) with Cs atoms: Towards the quasi-free graphene. *Thin Solid Films* **2013**, *543*, 59–62, 10.1016/j.tsf.2013.02.121.

[37] Zhang, X.; Wu, Z.; Zheng, H.; Ren, Q.; Zou, Z.; Mei, L.; Zhang, Z.; Xia, Y.; Lin, C.-T.; Zhao, P. High-quality graphene transfer via directional etching of metal substrates. *Nanoscale* **2019**, *11*, 16001–16006, 10.1039/C9NR05315H.

[38] Borin Barin, G.; Song, Y.; de Fátima Gimenez, I.; Souza Filho, A.G.; Barreto, L.S.; Kong, J. Optimized graphene transfer: Influence of polymethylmethacrylate (PMMA) layer concentration and baking time on graphene final performance. *Carbon* **2015**, *84*, 82–90, 10.1016/j.carbon.2014.11.040.

[39] Ambrosi, A.; Pumera, M. The CVD graphene transfer procedure introduces metallic impurities which alter the graphene electrochemical properties. *Nanoscale* **2014**, *6*, 472–476, 10.1039/C3NR05230C.

[40] Mishra, N.; Boeckl, J.; Motta, N.; Iacopi, F. Graphene growth on silicon carbide: A review. *Phys. Status Solidi A* **2016**, *213*, 2277–2289, 10.1002/pssa.201600091.

[41] Wang, J.; Li, N.; Xu, Y.; Pang, H. Two-Dimensional MOF and COF Nanosheets: Synthesis and Applications in Electrochemistry. *Chemistry* **2020**, *26*, 6402–6422, 10.1002/chem.202000294.

[42] Luong, D.X.; Bets, K.V.; Algozeeb, W.A.; Stanford, M.G.; Kittrell, C.; Chen, W.; Salvatierra, R.V.; Ren, M.; McHugh, E.A.; Advincula, P.A.; et al. Gram-scale bottom-up flash graphene synthesis. *Nature* **2020**, *577*, 647–651,

10.1038/s41586-020-1938-0.

[43] Le, T.H.; Oh, Y.; Kim, H.; Yoon, H. Exfoliation of 2D Materials for Energy and Environmental Applications. *Chemistry* **2020**, *26*, 6360–6401, 10.1002/chem.202000223.

[44] Martin-Perez, L.; Burzuri, E. Optimized Liquid-Phase Exfoliation of Magnetic van der Waals Heterostructures: Towards the Single Layer and Deterministic Fabrication of Devices. *Molecules* **2021**, *26*, 7371, 10.3390/molecules26237371.

[45] Backes, C.; Campi, D.; Szydlowska, B.M.; Synnatschke, K.; Ojala, E.; Rashvand, F.; Harvey, A.; Griffin, A.; Sofer, Z.; Marzari, N. Equipartition of Energy Defines the Size–Thickness Relationship in Liquid-Exfoliated Nanosheets. *ACS Nano* **2019**, *13*, 7050–7061, 10.1021/acsnano.9b02234.

[46] Xu, Y.; Cao, H.; Xue, Y.; Li, B.; Cai, W. Liquid-Phase Exfoliation of Graphene: An Overview on Exfoliation Media, Techniques, and Challenges. *Nanomaterials* **2018**, *8*, 942, 10.3390/nano8110942.

[47] Hernandez, Y.; Nicolosi, V.; Lotya, M.; Blighe, F.M.; Sun, Z.; De, S.; McGovern, I.T.; Holland, B.; Byrne, M.; Gun'Ko, Y.K.; et al. High-yield production of graphene by liquid-phase exfoliation of graphite. *Nat. Nanotechnol.* **2008**, *3*, 563–568, 10.1038/nnano.2008.215.

[48] Sitarek, K.; Stetkiewicz, J. Assessment of reproductive toxicity and gonadotoxic potential of N-methyl-2-pyrrolidone in male rats. *Int. J. Occup. Med. Environ. Health* **2008**, *21*, 73–80, 10.2478/v10001-008-0006-z.

[49] Shen, J.; He, Y.; Wu, J.; Gao, C.; Keyshar, K.; Zhang, X.; Yang, Y.; Ye, M.; Vajtai, R.; Lou, J.; et al. Liquid Phase Exfoliation of Two-Dimensional Materials by Directly Probing and Matching Surface Tension Components. *Nano Lett.* **2015**, *15*, 5449–5454, 10.1021/acs.nanolett.5b01842.

[50] Hernandez, Y.; Lotya, M.; Rickard, D.; Bergin, S.D.; Coleman, J.N. Measurement of multicomponent solubility parameters for graphene facilitates solvent discovery. *Langmuir* **2010**, *26*, 3208–3213, 10.1021/la903188a.

[51] Ghanbari, H.; Shafikhani, M.A.; Daryalaal, M. Graphene nanosheets production using liquid-phase exfoliation of pre-milled graphite in dimethylformamide and structural defects evaluation. *Ceram. Int.* **2019**, *45*, 20051–20057, 10.1016/j.ceramint.2019.06.267.

[52] Kai, L.N.; Barbara, M.M.; Ling, Q.; Colin, J.; Jesus, B.; Maria-Magdalena, T.; Iakovos, T.; Dmitry, G.E.; Kyriakos, P.; Jiawei, M.; et al. Direct Evidence of the Exfoliation Efficiency and Graphene Dispersibility of Green Solvents toward Sustainable Graphene Production. *ACS Sustainable Chemistry & Engineering* **2023**, *11*, 58–66, 10.1021/acssuschemeng.2c03594.

[53] Coleman, J.N.; Lotya, M.; O'Neill, A.; Bergin, S.D.; King, P.J.; Khan, U.; Young, K.; Gaucher, A.; De, S.; Smith, R.J.; et al. Two-dimensional nanosheets produced by liquid exfoliation of layered materials. *Science* **2011**, *331*, 568–571, 10.1126/science.1194975.

[54] O'Neill, A.; Khan, U.; Nirmalraj, P.N.; Boland, J.; Coleman, J.N. Graphene dispersion and exfoliation in low boiling point solvents. *J. Phys. Chem. C* **2011**, *115*, 5422–5428, 10.1021/jp110942e.

[55] Zhang, X.; Coleman, A.C.; Katsonis, N.; Browne, W.R.; Van Wees, B.J.; Feringa, B.L. Dispersion of graphene in ethanol using a simple solvent exchange method. *Chem. Commun.* **2010**, *46*, 7539–7541, 10.1039/C0CC02688C.

[56] Sethurajaperumal, A.; Varrla, E. High-Quality and Efficient Liquid-Phase Exfoliation of Few-Layered Graphene by Natural Surfactant. *ACS Sustain. Chem. Eng.* **2022**, *10*, 14746–14760, 10.1021/acssuschemeng.2c03742.

[57] Bonanni, A.; Pumera, M. Surfactants used for dispersion of graphenes exhibit strong influence on electrochemical impedance spectroscopic response. *Electrochem. Commun.* **2012**, *16*, 19–21, 10.1016/j.elecom.2011.12.012.

[58] Yang, Y.; Hou, H.; Zou, G.; Shi, W.; Shuai, H.; Li, J.; Ji, X. Electrochemical exfoliation of graphene-like two-dimensional nanomaterials. *Nanoscale* **2019**, *11*, 16–33, 10.1039/C8NR08227H.

[59] Li, F.; Xue, M.; Zhang, X.; Chen, L.; Knowles, G.P.; MacFarlane, D.R.; Zhang, J. Advanced composite 2D energy materials by simultaneous anodic and cathodic exfoliation. *Adv. Energy Mater.* **2018**, *8*, 1702794, 10.1002/aenm.201702794.

[60] Zeng, Z.; Yin, Z.; Huang, X.; Li, H.; He, Q.; Lu, G.; Boey, F.; Zhang, H. Single-Layer Semiconducting Nanosheets: High-yield preparation and device fabrication. *Angew. Chem.* **2011**, *50*, 11093–11097, 10.1002/anie.201106004.

[61] Fang, Y.; Li, X.; Li, J.; Yao, C.; Hoh, H.Y.; Hai, X.; Lu, J.; Su, C. Janus electrochemical exfoliation of two-dimensional materials. *J. Mater. Chem. A* **2019**, *7*, 25691–25711, 10.1039/C9TA10487A.

[62] Xia, Z.Y.; Pezzini, S.; Treossi, E.; Giambastiani, G.; Corticelli, F.; Morandi, V.; Zanelli, A.; Bellani, V.; Palermo, V. The exfoliation of graphene in liquids by electrochemical, chemical, and sonication-assisted techniques: A nanoscale study. *Adv. Funct. Mater.* **2013**, *23*, 4684–4693, 10.1002/adfm.201203686.

[63] Chen, H.; Liu, B.; Yang, Q.; Wang, S.; Liu, W.; Zheng, X.; Liu, Z.; Liu, L.; Xiong, C. Facile one-step exfoliation of large-size 2D materials via simply shearing in triethanolamine. *Mater. Lett.* **2017**, *199*, 124–127, 10.1016/j.matlet.2017.04.066.

[64] He, P.; Zhou, C.; Tian, S.; Sun, J.; Yang, S.; Ding, G.; Xie, X.; Jiang, M. Urea-assisted aqueous exfoliation of graphite for obtaining high-quality graphene. *Chem. Commun.* **2015**, *51*, 4651–4654, 10.1039/C5CC00059A.

[65] Ryu, M.Y.; Jang, H.K.; Lee, K.J.; Piao, M.; Ko, S.P.; Shin, M.; Huh, J.; Kim, G.T. Triethanolamine doped multilayer MoS_2 field effect transistors. *Phys. Chem. Chem. Phys.* **2017**, *19*, 13133–13139, 10.1039/C7CP00589J.

[66] Song, B.; Sizemore, C.; Li, L.; Huang, X.; Lin, Z.; Moon, K.S.; Wong, C.P. Triethanolamine functionalized graphene-based composites for high performance supercapacitors. *J. Mater. Chem. A* **2015**, *3*, 21789–21796, 10.1039/C5TA05674H.

[67] Blanco, A.; García-Abuín, A.; Gómez-Díaz, D.; Navaza, J.M.; Villaverde, Ó.L. Density, Speed of Sound, Viscosity, Surface Tension, and Excess Volume of N-Ethyl-2-pyrrolidone + Ethanolamine (or Diethanolamine or Triethanolamine) from T = (293.15 to 323.15) K. *J. Chem. Eng. Data* **2013**, *58*, 653–659, 10.1021/je301123j.

[68] Torrisi, F.; Carey, T. Graphene, related two-dimensional crystals and hybrid systems for printed and wearable electronics. *Nano Today* **2018**, *23*, 73–96, 10.1016/j.nantod.2018.10.009.

[69] Salavagione, H.J.; Sherwood, J.; Budarin, V.; Ellis, G.; Clark, J.; Shuttleworth, P. Identification of high performance solvents for the sustainable processing of graphene. *Green Chem.* **2017**, *19*, 2550–2560, 10.1039/C7GC00112F.

[70] Paolucci, V.; D'Olimpio, G.; Lozzi, L.; Mio, A.M.; Ottaviano, L.; Nardone, M.; Nicotra, G.; Le-Cornec, P.; Cantalini, C.; Politano, A. Sustainable Liquid-Phase Exfoliation of Layered Materials with Nontoxic Polarclean Solvent. *ACS Sustain. Chem. Eng.* **2020**, *8*, 18830–18840, 10.1021/acssuschemeng.0c04191.

[71] D'Olimpio, G.; Occhiuzzi, J.; Lozzi, L.; Ottaviano, L.; Politano, A. Dimethyl 2-Methylglutarate (Iris): A Green Platform for Efficient Liquid-Phase Exfoliation of 2D Materials. *Adv. Sustain. Syst.* **2022**, *6*, 2200277, 10.1002/adsu.202200277.

[72] Vidal, T.; Bramati, V.; Murthy, K.; Abribat, B. A New Environmentally Friendly Solvent of Low Toxicity for Crop Protection Formulations. *J. ASTM Int.* **2011**, *8*, 1–8, 10.1520/JAI103716.

[73] Dong, X.; Al-Jumaily, A.; Escobar, I.C. Investigation of the use of a bio-derived solvent for non-solvent-induced phase separation (NIPS) fabrication of polysulfone membranes. *Membranes* **2018**, *8*, 23, 10.3390/membranes8020023.

[74] Lebarbé, T.; More, A.S.; Sane, P.S.; Grau, E.; Alfos, C.; Cramail, H. Bio-Based Aliphatic Polyurethanes Through

ADMET Polymerization in Bulk and Green Solvent. *Macromol. Rapid Commun.* **2014**, *35*, 479–483, 10.1002/marc.201300695.

[75] Llevot, A.; Grau, E.; Carlotti, S.; Grelier, S.; Cramail, H. Dimerization of abietic acid for the design of renewable polymers by ADMET. *Eur. Polym. J.* **2015**, *67*, 409–417, 10.1016/j.eurpolymj.2014.10.021.

[76] Luciani, L.; Goff, E.; Lanari, D.; Santoro, S.; Vaccaro, L. Waste-minimised copper-catalysed azide–alkyne cycloaddition in Polarclean as a reusable and safe reaction medium. *Green Chem.* **2018**, *20*, 183–187, 10.1039/C7GC03022C.

[77] Mcintyre, N.S.; Spevack, P.A.; Beamson, G.; Briggs, D. Effects of Argon Ion-Bombardment on Basal-Plane and Polycrystalline MoS_2. *Surf. Sci.* **1990**, *237*, L390–L397, 10.1016/0039-6028(90)90508-6.

[78] Baker, M.A.; Gilmore, R.; Lenardi, C.; Gissler, W. XPS investigation of preferential sputtering of S from MoS_2 and determination of MoS_x stoichiometry from Mo and S peak positions. *Appl. Surf. Sci.* **1999**, *150*, 255–262, 10.1016/S0169-4332(99)00253-6.

[79] Alov, N.V. XPS study of MoO_3 and WO_3 oxide surface modification by low-energy Ar^+ ion bombardment. *Phys. Status Solidi C* **2015**, *12*, 263–266, 10.1002/pssc.201400108.

[80] Di Paola, A.; Palmisano, L.; Venezia, A.; Augugliaro, V. Coupled semiconductor systems for photocatalysis. Preparation and characterization of polycrystalline mixed WO_3/WS_2 powders. *J. Phys. Chem. B* **1999**, *103*, 8236–8244, 10.1021/jp9911797.

[81] Wong, K.; Lu, X.; Cotter, J.; Eadie, D.; Wong, P.; Mitchell, K. Surface and friction characterization of MoS_2 and WS_2 third body thin films under simulated wheel/rail rolling–sliding contact. *Wear* **2008**, *264*, 526–534, 10.1016/j.wear.2007.04.004.

[82] Shpak, A.; Korduban, A.; Kulikov, L.; Kryshchuk, T.; Konig, N.; Kandyba, V. XPS studies of the surface of nanocrystalline tungsten disulfide. *J. Electron Spectrosc. Relat. Phenom.* **2010**, *181*, 234–238, 10.1016/j.elspec.2010.05.030.

[83] Malard, L.M.; Pimenta, M.A.; Dresselhaus, G.; Dresselhaus, M.S. Raman spectroscopy in graphene. *Phys. Rep.* **2009**, *473*, 51–87, 10.1016/j.physrep.2009.02.003.

[84] Ferreira, E.M.; Moutinho, M.V.; Stavale, F.; Lucchese, M.M.; Capaz, R.B.; Achete, C.A.; Jorio, A. Evolution of the Raman spectra from single-, few-, and many-layer graphene with increasing disorder. *Phys. Rev. B* **2010**, *82*, 125429, 10.1103/PhysRevB.82.125429

[85] Cançado, L.G.; Jorio, A.; Ferreira, E.H.M.; Stavale, F.; Achete, C.A.; Capaz, R.B.; Moutinho, M.V.O.; Lombardo, A.; Kulmala, T.S.; Ferrari, A.C. Quantifying Defects in Graphene via Raman Spectroscopy at Different Excitation Energies. *Nano Lett.* **2011**, *11*, 3190–3196, 10.1021/nl201432g.

[86] Khan, U.; Porwal, H.; O'Neill, A.; Nawaz, K.; May, P.; Coleman, J.N. Solvent-exfoliated graphene at extremely high concentration. *Langmuir* **2011**, *27*, 9077–9082, 10.1021/la201797h.

[87] Çelik, Y.; Flahaut, E.; Suvacı, E. A comparative study on few-layer graphene production by exfoliation of different starting materials in a low boiling point solvent. *FlatChem* **2017**, *1*, 74–88, 10.1016/j.flatc.2016.12.002.

[88] Zhang, R.; Zhang, B.; Sun, S. Preparation of high-quality graphene with a large-size by sonication-free liquid-phase exfoliation of graphite with a new mechanism. *RSC Adv.* **2015**, *5*, 44783–44791, 10.1039/C5RA04480D.

[89] Yi, M.; Shen, Z.; Zhang, X.; Ma, S. Achieving concentrated graphene dispersions in water/acetone mixtures by the strategy of tailoring Hansen solubility parameters. *J. Phys. D Appl. Phys.* **2012**, *46*, 025301, 10.1088/0022-3727/46/2/025301.

[90] Capasso, A.; Castillo, A.D.R.; Sun, H.; Ansaldo, A.; Pellegrini, V.; Bonaccorso, F. Ink-jet printing of graphene

for flexible electronics: An environmentally-friendly approach. *Solid State Commun.* **2015**, *224*, 53–63, 10.1016/j.ssc.2015.08.011.

[91] Biccai, S.; Barwich, S.; Boland, D.; Harvey, A.; Hanlon, D.; McEvoy, N.; Coleman, J.N. Exfoliation of 2D materials by high shear mixing. *2D Mater.* **2018**, *6*, 015008, 10.1088/2053-1583/aae7e3.

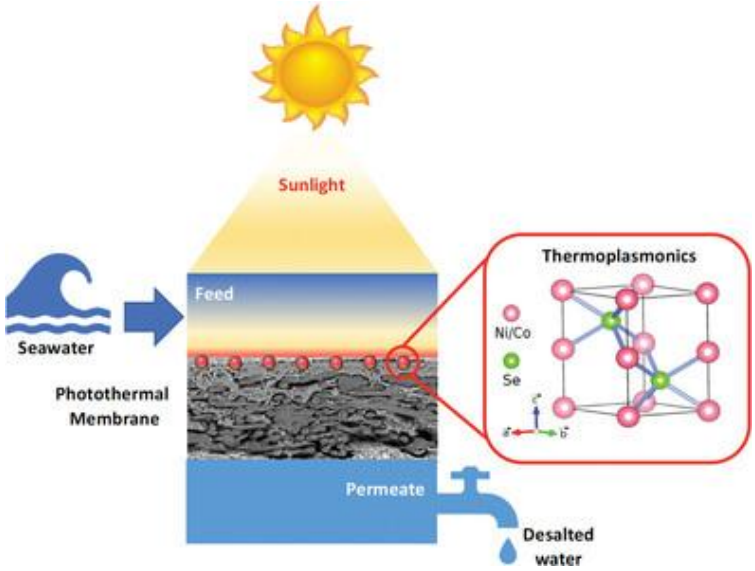
[92] Tominaga, Y.; Sato, K.; Shimamoto, D.; Imai, Y.; Hotta, Y. Wet-jet milling-assisted exfoliation of h-BN particles with lamination structure. *Ceram. Int.* **2015**, *41*, 10512–10519, 10.1016/j.ceramint.2015.04.143.

Chapter 4

NiSe and CoSe Topological Nodal-Line Semimetals: A Sustainable Platform for Efficient Thermoplasmonics and Solar-Driven Photothermal Membrane Distillation

Keywords: Solar membrane distillation; thermoplasmonics; topological materials; optical anisotropy; nodal-line semimetals

GRAPHICAL ABSTRACT



Contents

Abstract

4.1 Introduction

4.1.1 Thermoplasmonics and Its Applications

4.1.2 Advancing Solar Membrane Distillation with Photothermal Materials

4.2 Results

4.2.1 Structural characterization of NiSe and CoSe Nanoparticles
4.2.2 Morphological characterization
4.2.3 Photothermal performance and Solar-Driven MD Efficiency
4.2.4 Stability, Energy efficiency and Potential Applications

4.3 Experimental Section

4.3.1 Nanoparticles preparation

4.3.2 Membrane procedure

4.3.3 Experimental Setup for Solar-Driven VMD procedure

4.4 Conclusions

References

This chapter has been published as:

Abramovich S., Dutta D., Rizza C., Santoro S., Aquino M., Cupolillo A., Occhiuzzi J., La Russa M.F., Ghosh B., Farias D., Locatelli A., Boukhvalov D.W., Agarwal A., Curcio E., Bar Sadan M., Politano A.; NiSe and CoSe topological nodal-line semimetals: a sustainable platform for efficient thermoplasmonics and solar-driven photothermal membrane distillation Small 18 2201473 (https://doi.org/10.1002/smll.202201473)

Abstract

The control of heat at the nanoscale via the excitation of localized surface plasmons in nanoparticles (NPs) irradiated with light holds great potential in several fields (cancer therapy, catalysis, desalination). To date, most thermoplasmonic applications are based on Ag and Au NPs, whose cost of raw materials inevitably limits the scalability for industrial applications requiring large amounts of photothermal NPs, as in the case of desalination plants. On the other hand, alternative nanomaterials proposed so far exhibit severe restrictions associated with the insufficient photothermal efficacy in the visible, the poor chemical stability, and the challenging scalability. Here, it is demonstrated the outstanding potential of NiSe and CoSe topological nodal-line semimetals for thermoplasmonics. The anisotropic dielectric properties of NiSe and CoSe activate additional plasmonic resonances. Specifically, NiSe and CoSe NPs support multiple localized surface plasmons in the optical range, resulting in a broadband matching with sunlight radiation spectrum. Finally, it is validated the proposed NiSe and CoSe-based thermoplasmonic platform by implementing solar-driven membrane distillation by adopting NiSe and CoSe nanofillers embedded in a polymeric membrane for seawater desalination. Remarkably, replacing Ag with NiSe and CoSe for solar membrane distillation increases the transmembrane flux by 330% and 690%, respectively. Correspondingly, costs of raw materials are also reduced by 24 and 11 times, respectively. The results pave the way for the advent of NiSe and CoSe for efficient and sustainable thermoplasmonics and related applications exploiting sunlight within the paradigm of the circular blue economy.

4.1 Introduction

4.1.1 Thermoplasmonics and Its Applications

In recent years, the opportunity to exploit metal nanostructures as nanosources of heat, tunable with light, has originated the fast-growing field of thermoplasmonics.[1] Upon illumination at the plasmon frequency, metal NPs display enhanced light absorption, enabling efficient light-to-heat conversion.[1a] Recently, thermoplasmonic effects have been successfully exploited mainly for biomedical applications, such as photothermal cancer therapy,[2] neural stimulation,[3] bacteria killing,[4] intracellular delivery of miRNA,[5] photothermal biosensors for SARS-CoV-2 detection.[6] Additionally, thermoplasmonic effects also play a pivotal role in photothermal actuators,[7] nanofurnaces for heterogeneous catalysis,[8] and solar-driven water evaporation.[9] In particular, thermoplasmonics could provide a relevant contribution for addressing the global water shortage, which represents one of the most vital open challenges for mankind,[10] further

exacerbated by climate change[11] and particularly relevant in developing countries.[12] Concomitantly, the urgent need for a green transition[13] has boosted the advent of sustainable technologies for seawater desalination,[14] enabling the integration of renewable energy sources, such as solar power, in desalination processes,[15] today dominated by membranes.[16] Among the various membrane technologies, MD affords a reliable prospect to recover simultaneously fresh water from seawater and brine at competitive costs.[17] Explicitly, MD is based on the evaporation and diffusion of water through a microporous hydrophobic membrane under a vapor pressure gradient.[10c,18] Although unlimited by osmotic and concentration polarization phenomena affecting pressure-driven operations, such as reverse osmosis,[19] the efficiency of MD is severely reduced (even by 30–50% [20]) by temperature polarization,[20] which consists in the reduction of the temperature at the feed side, within the boundary layer adjacent to the membrane interface, as a result of the removal of the latent heat of vaporization associated to the transmembrane flux of water vapor.

4.1.2 Advancing Solar Membrane Distillation with Photothermal Materials

While MD unquestionably still faces critical technological challenges, the use of radically innovative physicochemical concepts and processes, enabled by novel materials, could provide step-change improvements. In this respect, the localized heating at the water vapor–liquid interface achieved by light-toheat conversion in photothermal materials has recently opened unprecedented opportunities in MD.[21] Using photothermal materials in MD could be crucial to implementing an environment-friendly green technology, exploiting renewable energy sources, such as solar power, to achieve efficient solar desalination.[15] In particular, photothermal MD implemented with plasmonic Ag nanofillers in hydrophobic polymeric membranes was shown to increase the transmembrane flux by one order of magnitude when irradiated with UV light.[10c,22] Accordingly, thermoplasmonic effects, promoted under solar irradiation, could be exploited to implement an innovative photothermal MD unit powered by sunlight, enabling its installation in remote areas without electric power grids for producing potable water for isolated communities, only using solar power. However, the use of Ag implies i) high costs impeding industrial scale-up and ii) an inefficient matching with sunlight radiation spectrum. In general, replacing Ag and Au with cheap materials, exhibiting plasmonic resonances matching with the solar spectrum is one of the main open challenges of the whole plasmonic community.[23] Recently, several candidates for have emerged, such as nitrides (TiN[24] and HfN[25]), SnS_2 [26] /$SnSe_2$, [27] Xenes (phosphorene,[28] arsenene,[29] stanene[30]), titanium carbides (namely, MXenes[31]), metal

oxides,[32] etc. However, most of them have poor photothermal efficacy[10e] and high chemical instability with spontaneous oxidation already at room temperature, as in the case of Xenes [33] or tin dichalcogenides.[34] Historically, individual plasmonic materials were initially identified mainly by intuition, trial, and error, and analogy to other materials, often with successive theoretical models to unveil their connection with band structure.[35] However, the recent efforts to perform a systematic analysis of band structure [36] can provide step-change support in the quest of photothermal materials with desired features in terms of excitation spectrum and light-to-heat conversion efficiency.[35a] Such a materials genome approach, now implemented in open-source databases, [37] is ideal for achieving a band-structure engineered platform for thermoplasmonics and related applications. In particular, the crystal anisotropy, [38] with corresponding anisotropic optical properties, offers novel functionalities for applications in plasmonics.[39] As a matter of fact, electromagnetic anisotropy is commonly adopted in engineering several optical devices, such as polarizers, [40] wave plates, [41] hyper-lenses, [42] spatial optical filters, [43] and phase matching components. [44] In principle, electromagnetic anisotropy could open new excitation channels with superior photothermal efficiency by improving the matching with the sunlight radiation spectrum. Here, we demonstrate that the anisotropic optical properties of NiSe and CoSe make them a suitable platform for solardriven thermoplasmonics, by combining theoretical predictions based on their band structure and dielectric properties, up to a direct validation carried out by fabricating photothermal nanocomposite hydrophobic membranes with NiSe and CoSe nanofillers. Outstandingly, the replacement of Ag (widely recognized as a state-of-the-art reference for thermoplasmonics) with NiSe and CoSe nanoscale thermal hotspots enables a significantly improved efficiency of solar membrane distillation, with an increase of transmembrane flux by 330% and 690% and with a reduction of costs by 24 and 11 times, respectively.

4.2 Results

4.2.1 Structural characterization of NiSe and CoSe Nanoparticles

NiSe and CoSe NPs were synthetized following the Experimental Section (below, in the paragraph 4.3) extensively described in the corresponding section. The analysis of X-ray diffraction (XRD) pattern indicated that the crystallographic structure for both NPs is hcp (P63/mmc space group), with lattice parameters matching with ICDD 00-002-0892 and 00-008-0414 for NiSe and CoSe, respectively. The analysis based on transmission electron microscopy (TEM) images indicated a wide size distribution of synthetized NiSe and CoSe NPs (Figure 4.1 a,b), with an average diameter

of 30 ± 7 and 15 ± 5 nm for NiSe and CoSe NPs, respectively.

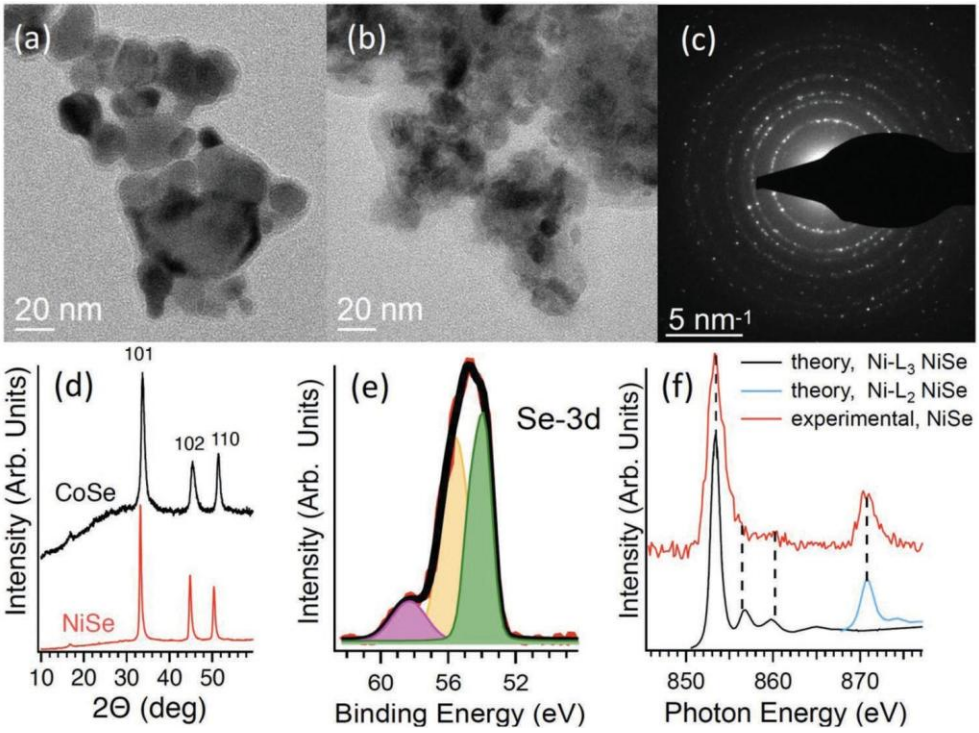


Figure 4.1. *a) TEM images of NiSe b) and CoSe. c) SAED images of NiSe. d) Powder XRD diffraction pattern of NiSe and CoSe. e) μ-XPS spectrum on an individual NiSe NP measured by means of XPEEM apparatus, with a photon energy of 150 eV. The purple, yellow, and green areas depict the spectral contribution from SeO_{2-x}, Se(0) and Se(II) species, respectively. f) Experimental Ni-L_{23} absorption edge, measured on an individual NiSe NP, compared with theoretical predictions by Feff 9 code for L_2 and L_3 absorption edges of NiSe.*

The physicochemical properties of NiSe and CoSe nanofillers, including their surface status, were assessed by nano spectroscopy tools at the soft X-ray beamline Nanospectroscopy at Elettra–Trieste synchrotron, using an energy-filtered Low Energy Electron Microscope (LEEM)-Photoelectron Emission Microscope (PEEM) with spatial resolution of 10 nm.

Using X-ray photoelectron microscopy (XPEEM), NiSe and CoSe NPs were imaged and, moreover, core levels were acquired (Figure 4.1 e) with nanoscale resolution. To provide information on the surface of the NPs, surface sensitivity was enhanced by using low-energy photons (150 eV).

4.2.2 Morphological characterization

Specifically, we observed by μ-XPS (X-ray photoelectron spectroscopy) three different oxidation status in Se-3d core levels, arising from Se(II) and Se(0) species at a binding energy of 53.8 and

55.2 eV, respectively. On the other hand, oxidation is limited, as indicated by the SeO_{2-x} component at 58.0 eV with only 11% of the spectral area, while in previous studies on NiSe NPs this component was even predominant in the region of Se-3d core levels.[51] Conversely, the bulk crystals of the NPs are stoichiometric, as also indicated by the excellent matching of the experimental Ni-L_{23} absorption edge with theoretical predictions for the case of NiSe by using Feff 9 code.[52]

To validate the use of NiSe and CoSe NPs in thermoplasmonics, we implemented solar-driven MD with nanocomposite membranes with NiSe and CoSe nanofillers.

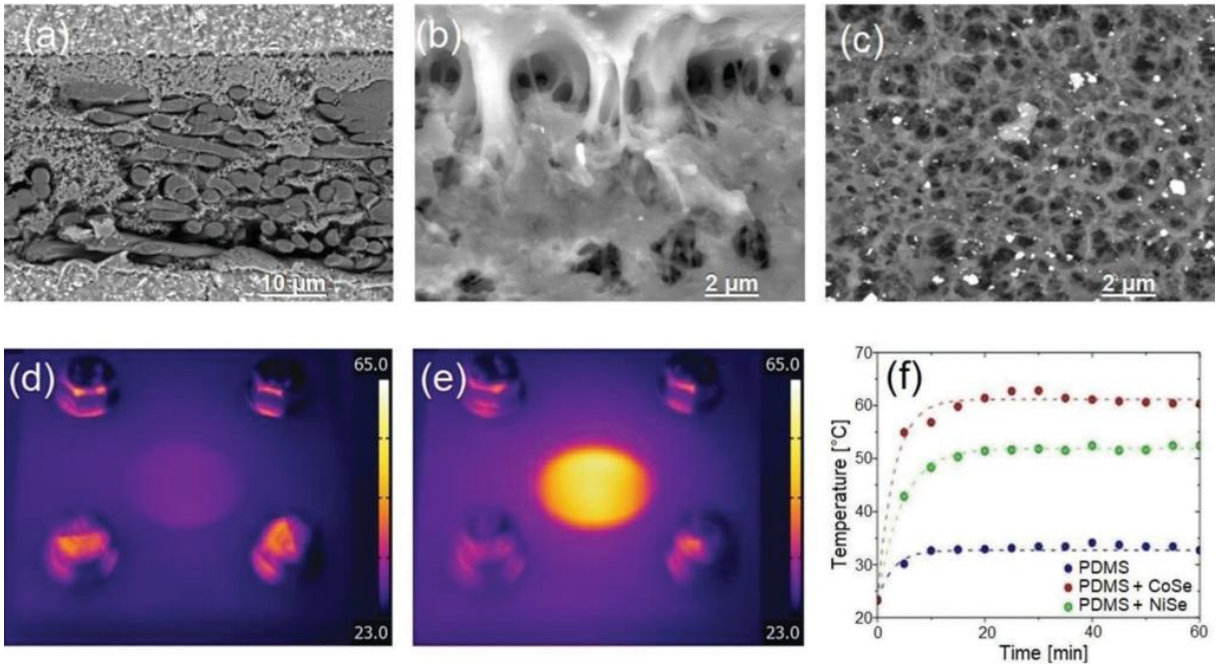


Figure 4.2. *SEM micrographs of CoSe (2.5 wt%) in PDMS/PVDF membrane: a) cross-sectional view (magnification 900x). b) Detail of the cross-section of the coating (magnification 10 000x). c) Top view of coated surface (magnification 4000x). Infrared pictures under 1-sun illumination of composite membranes coated by d) bare PDMS and e) PDMS loaded with 2.5 wt% CoSe. f) Evolution in time of the temperature profile of membrane surface under solar radiation of bare PDMS coating and of nanocomposite coatings based on 2.5 wt% of NiSe and CoSe embedded into PDMS.*

The SEM cross-sectional micrograph of the nanocomposite membrane (Figure 4.2 a), made of a polyvinylidene fluoride (PVDF) support coated with a thin porous polydimethylsiloxane $(C_2H_6OSi)_n$ (PDMS) layer embedding NiSe or CoSe NPs, revealed a porous structure, which extends throughout the membrane thickness (180 ± 2 µm). The choice of PDMS as an anchoring agent for NPs secured a proper adhesion to the substrate, owing to the abundance of silanol moieties able to interact with the fluorinated support.[53] The coating layer appeared uniformly distributed over the PVDF support with a thickness of around 2 µm (Figure 4.2 b). NPs are clearly

noticeable on the surface of the composite membrane (Figure 4.2 c), endowing the membrane with photothermal features.

4.2.3 Photothermal performance and Solar-Driven MD Efficiency

Noteworthy, the low concentration of Si in the sprayed solution secured an appropriate membrane porosity of the photothermal layer (i.e., 54.6 ± 1.6%), slightly lower than that of the bare support (56.7 ± 0.8%). This morphology, characterized by a mean pore size of 0.21 ± 0.05 µm, offers a minimal resistance to the mass transport of water vapor through the membrane.

Further characterization confirmed that the developed nanocomposite membranes exhibited suitable features for MD applications. In particular, the high hydrophobic behaviour (contact angle > 110°), combined with the submicrometric pore size (largest pore <0.3 µm), secures a Liquid Entry Pressure (LEP) - estimated according to the Young-Laplace equation [54] - ranging from 1.5 bar for 2.5 wt% CoSe-PDMS to 2.6 bar for 2.5 wt% NiSe-PDMS. The values of LEP, i.e. the minimum hydrostatic pressure required to push the liquid into the largest membrane pores, exceed the operational transmembrane pressure of vacuum membrane distillation (VMD) process, preventing the wetting phenomenon and the consequent reduction of the salt rejection. [55] Energy-dispersive x-ray spectroscopy (EDS) analysis revealed the presence of Si atoms only within the coated top layer. This observation was corroborated by cross-sectional EDS analysis of the membranes with PDMS coating loaded with 2.5 wt% NiSe and 2.5 wt% CoSe which confirmed the presence of metallic NPs in the proximity of the membrane surface. This is a crucial aspect, since the localization of NPs at the membrane surface: i) secures an efficient absorption of the incident radiation; ii) accelerates the evaporation rate thanks to an efficient light-to-heat conversion at the membrane-water interface, and iii) minimizes the cost of the nanocomposite photothermal layer. [56] Thermal imaging upon solar irradiation reveled the effectiveness of light-to-heat conversion promoted by the plasmonic nanofillers. Interestingly, the coating with 2.5 wt% CoSe (NiSe) coating reached a temperature of 61.9 ± 0.5 °C (52.4 ± 0.5 °C) under the equivalent of 1-sun solar irradiance (1000 W m^{-2}) in about 10 min. On the contrary, without photothermal nanofillers, i.e., for the bare PDMS coating, a temperature of 32.7 ±0.5 °C was observed even after 1h of sunlight exposure.

4.2.4 Stability, Energy efficiency and Potential Applications

This efficient light-to-heat conversion localized on the membrane surface is very attractive for the

MD process, securing a sustainable energy harvesting for the interfacial evaporation of water molecules and an effective overcoming of the thermal polarization, the major drawback of MD technology.[20] Therefore, the self-heating properties of the photothermal membranes are exploitable for boosting the vaporization of water: CoSe coating demonstrated a superior light-to-heat-to vapor conversion with a photothermal efficiency (η) of 54.2%; whereas values of 18.4% and 38.3% were observed for bare PDMS and PDMS loaded with 2.5 wt% NiSe coating, respectively. More precisely, we tested the potential of NiSe and CoSe for thermoplasmonics by implementing a solar-driven VMD. It should be remembered that in VMD the transmembrane flux (Jw) is proportional to the difference between the partial pressure of water vapor at the feed-membrane interface ($p_w^{membrane}$) and the vacuum pressure (p_w^{vacuum})

$$J_w = K\,(p_w^{membrane} - p_w^{vacuum})$$

where ($p_w^{membrane} - p_w^{vacuum}$) represents the driving force for the transport of water molecules in the gas phase through the membrane, and K is the mass transfer coefficient. According to Raoult's law, the value of $p_w^{membrane}$ is obtained by multiplying the vapor pressure of pure water p_w^0 evaluated at the interface temperature of the membrane (T_f^*), the molar fraction (x_w) and activity coefficient (γ_w, ≠1 for a nonideal mixture) of water in the feed solution.

The presence of photothermal NPs in the polymeric coating negligibly impacted on K. Membranes with a coating of bare PDMS and its modification by the inclusion of 2.5 wt% NiSe and CoSe nanofillers exhibited K values of 55.2, 58.1, and 58.9 kg m^{-2} h^{-1} atm^{-1} respectively, as resulting from VMD experiments carried out at 20 °C without sunlight irradiation. The advantages of the efficient light-to-heat conversion of NiSe and CoSe NPs are evident from the inspection of Figure 4.3 b. The temperature increase generated by nanoscale thermal hotspots resulted in an exponential increase of the transmembrane flux (J_w), coherently with the trend of water vapor pressure established by the Clausius–Clapeyron equation ($p_w^{membrane}$ increased from 39 to 152 mmHg under artificial solar irradiation sun by embedding CoSe NPs).

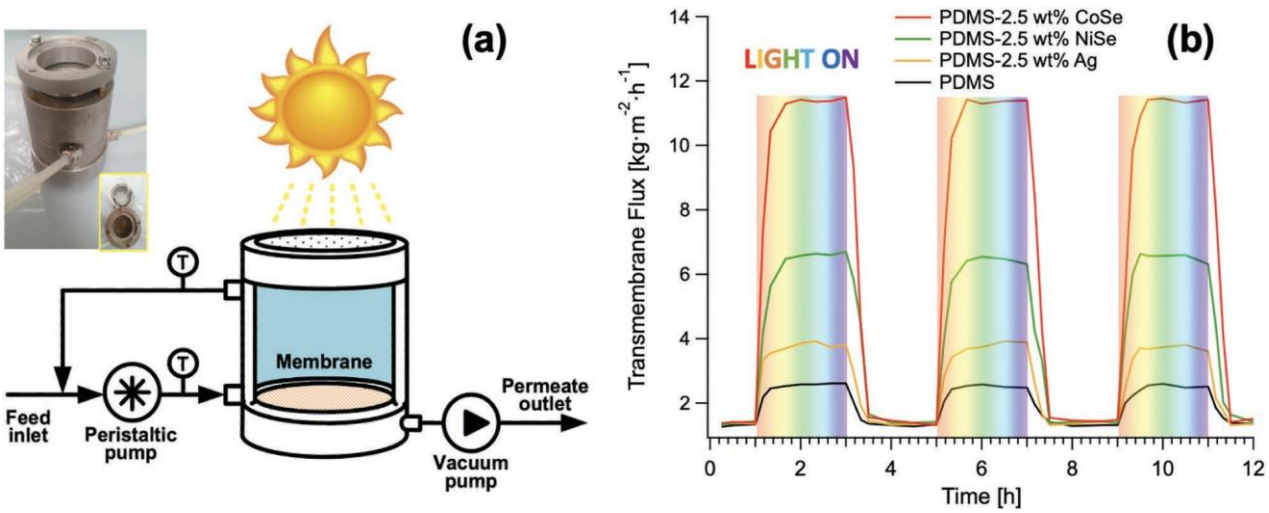


Figure 4.3. *a) Schematics of solar-driven VMD. The inset shows a photograph of the experimental apparatus. b) Transmembrane flux in VMD experiments using composite membranes with a coating of (black curve) bare PDMS and, moreover, 2.5 wt% of (orange curve) Ag; (green curve) NiSe; and (red curve) CoSe NPs embedded into PDMS. Feed: artificial seawater (0.5 m NaCl). Experiments were repeated for three cycles covering 12 h in presence (light ON) or absence (light OFF) of artificial solar irradiation (1000 W m^{-2}).*

For VMD operating under 1-sun illumination with pure water at 20 °C, bare PDMS coating provided a J_w of 2.6 ± 0.13 kg m^{-2} h^{-1} (T_f^* = 32.7 °C), whereas the evaporative flux raised to 6.8 ± 0.3 and 11.4 ± 0.3 kg m^{-2} h^{-1} in the presence of NiSe and CoSe nanofillers (corresponding to T_f^* of 52.4 and 61.9 °C), respectively. Moreover, the improvement of the productivity of the VMD process without increasing the energetic input resulted in a decreasing of the Specific Thermal Energy Consumption (STEC) required for water vaporization. In fact, the embodiment of NiSe and CoSe reduced the STEC of VMD of 61.8% and 77.2%, respectively, in comparison to the bare PDMS coating. The STEC required for solar-driven VMD performed with photothermal membranes load with CoSe nanofillers was 80 Kwh m^{-3} below the range of 130–210 Kwh m^{-3} estimated for stand-alone pilot-plant supplied by Solar Photovoltaic Technology.[57]

The effectiveness of desalination operations was confirmed by VMD experiments performed by feeding both seawater (0.5 m NaCl) and seawater reverse osmosis brine (1.0 M NaCl). Regardless of the concentration of dissolved salt, a high-quality distilled water (electrical conductivity below 0.1 μS cm^{-1}) was collected as permeate. Moreover, the transmembrane flux only showed a slight decrease by 4.3% and 5.2% when increasing the feed solution concentration to 0.5 and 1 M, respectively, due to the diminution of γ_w (from 0.983 to 0.966) and x_w (0.991–0.981).

In Figure 4.3 b, we also compare NiSe and CoSe with state-of-the-art reference for photothermal MD, i.e., Ag under 1-sun illumination. Notably, replacing Ag with NiSe and CoSe for solar membrane distillation increases of the transmembrane flux by 330% and 690%, respectively.

Correspondingly, costs are reduced by 24 and 11 times, respectively. Moreover, the fabricated NiSe- and CoSe-based nanocomposite membranes are exceptionally stable, as demonstrated by the excellent reproducibility even for an extended amount of working hours, consistently with the suitable chemical stability of NiSe and CoSe nanofillers inferred by density functional theory (compared to the table in the reference article, not shown in this chapter) and μ-XPS data (Figure 4.1 e).

Both DLS and high-resolution continuum source atomic absorption spectrometer (HR-CS AAS) analysis proved the absence of NiSe or CoSe NPs and related ions in the distillate, which presented in all cases a conductivity below than 10 $\mu S\ cm^{-1}$, demonstrating the efficiency of the photothermal membrane in seawater desalination (ion rejection>99%) and the absence of leaching.

The long-term stability of the photothermal membrane was demonstrated by protracting photothermal VMD practices for 24 h. VMD experiments using composite membranes with a coating of PDMS loaded with 2.5 wt% of CoSe secured a recovery factor of ≈75% in 24 h leading to a significant improvement of the concentration of NaCl in the retentate from 0.5 to 2 $_M$ reducing therefore the driving force of the mass transport due to the due to the diminution of γ_w (from 0.983 to 0.923) and x_w (0.991–0.965). Hence, the implementation of CoSe in solar driven VMD favors a drastic reduction of the brine produced in the retentate as byproduct of the process. Noteworthy, these experiments confirmed the opportunity to intensify the desalination process via solar-driven VMD exceeding the current water recovery factor of 50% of traditional desalination based on Reverse Osmosis.

4.3 Experimental section

4.3.1 Nanoparticles preparation

Synthesis of NiSe and CoSe NPs: NiSe and CoSe NPs were synthesized by a solvothermal technique. The initial step for the synthesis of NiSe and CoSe consisted in dissolving nickel (II) nitrate hexahydrate Ni $(NO_3)_2 \cdot 6H_2O$ (0.2 mmol) and cobalt (II) nitrate hexahydrate Co $(NO_3)_2 \cdot 6H_2O$ (0.2 mmol) in 50 mL of deionized water with stirring for 10 min, respectively. Separately, selenium powder (0.4 mmol) and hydrazine hydrate (20 mL) were stirred for 10 min. The two solutions were mixed and transferred to a Teflon-lined stainless-steel autoclave containing ethanolamine (10 mL) and kept at 180 °C for 16 h. After cooling to room temperature, the obtained products were centrifuged, washed several times with ethanol, and dried under vacuum.

Instrumentation and Methods: TEM: The suspensions were dropcasted onto a TEM grid and dried. JEOL 2100F transmission electron microscope operated at 200 kV.

SEM: Field emission scanning electron microscope (FESEM) experiments were carried with Gemini SEM 500, at an accelerating voltage of 2 kV.

Powder XRD: Panalytical Empyrean powder X-ray diffractometer equipped with a position-sensitive X'Celerator detector using Cu kα radiation.

Porometer: Measurements of pore size of nanocomposite membranes were carried out by using a PMI capillary flow porometer (Porous Materials Inc., Ithaca, NY) using Porewick (surface tension = 16 dyn cm^{-1}) as wetting liquid and processing the data with the software Caprep (Porous Materials Inc., Ithaca, NY).

4.3.2 Membrane procedure

Membrane Preparation: Composite membranes based on a thin porous layer of PDMS (Sigma-Aldrich) loaded with NiSe and CoSe NPs were prepared by the spray coating method. As support, a microporous commercial PVDF membrane Fortex complying ISO 10 993 and USP Class VI, with nominal pore size 0.2 μm (GVS, Italy) was used. The coating solution was prepared by dispersing the photothermal NPs via sonication (Sonica2200ETH, Soltec, Italy) for 30 min in heptane (Sigma-Aldrich). Then, PDMS was dissolved into the colloidal solution (5 wt%) by stirring for 3 h at room temperature. The concentration of the photothermal NPs was 2.5 wt% with respect to PDMS. Finally, the crosslinker was added to the polymeric solution at a concentration of 10 wt% with respect to PDMS. The polymeric solution (10 mL) was then transferred to an airbrush equipped with a compressor (Gocheer, model TS100BMC). The system was mounted on a 2D positioning control system for the planar motion (TEVO Tornado) at a velocity 60 mm s^{-1}. Each PVDF membrane (112 cm^2) was sprayed three times and then transferred in an oven at 60 °C for 60 min to promote the crosslinking of the polymer and the evaporation of the solvent.

4.3.3 Experimental Setup for Solar-Driven VMD procedure

VMD Experiments: A solar irradiation simulator (Abet Technologies, US) with irradiance of 1 sun (1000 W m^{-2}) over a 35 mm diameter field was used to irradiate a dedicated dead-end VMD cell with effective membrane area of 7.06 cm^2. The VMD cell was equipped with a quartz window and the solar lamp was put 10 cm above this quartz window to ensure that the light could irradiate the membrane. The lab-scale plant operated under vacuum pressure of 20 mbar and initial feed temperature of 293 K. The permeate conductivity was measured using a YSI Model 3200 conductivity meter at 20 °C (range: 0–4999 μS m^{-1}, accuracy: ±0.50% full scale, resolution: 1 μS

m^{-1}). For solar-driven VMD experiments, experiments with the same Ag NPs used for the previous works [10 c,d] for the sake of comparison were also carried out. Feed solution recirculated throughout the cell at 5.5×10^{-6} m^3 s^{-1} by a Masterflex L/S digital peristaltic pump (Cole-Palmer, US), whereas distillate was stripped by a vacuum pump VWR VP 820 (VWR International, US). The quality of the distillate was estimated with a DLS 90Plus Particle Size Analyzer (Brookhaven Instruments Corporation, USA) and a HR-CS AAS by means of ContrAA 700 (Analytik Jena AG, Germany) with a high-intensity Xe short-arc lamp as continuum source. STEC of solar-driven VMD was estimated according to the following equation

$$STEC = \frac{P_\rho}{J} \tag{3}$$

where P is the irradiance of the artificial sunlight, ρ is the water density, and J is the transmembrane flux in VMD practice.

4.4 Conclusions

In conclusion, the promising prospect of NiSe and CoSe for thermoplasmonics has been demonstrated by a joint theoretical and experimental investigation, going from the disclosure of their exotic electronic and optical properties up to technological implementation in the field of solar desalination. Remarkably, NiSe and CoSe show a giant electromagnetic anisotropy enabling multiple localized surface plasmon resonances lying in the optical range, as well as an unprecedentedly efficient plasmon-assisted solar thermal conversion. To validate our model, we carried out experiments of solar membrane distillation, using membranes coated with NiSe and CoSe NPs synthetized for this aim with a size tuned for achieving the optimal light-to-heat conversion efficiency. Explicitly, replacing Ag with NiSe and CoSe for solar MD increased the transmembrane flux by 330% and 690%, respectively, and, in addition, the corresponding costs of raw materials are reduced by 24 and 11 times. Accordingly, already in the first implementation, NiSe- and CoSe-based solar desalination largely exceeds state-of-the-art performances. Evidently, photothermal effects in NiSe and CoSe can improve the efficiency of any other application based on solar thermal conversion (solar steam generation, high-temperature heterogeneous catalysis, solar thermophotovoltaics, thermoelectric power generation, etc.), beyond solar-driven MD herein selected as a case study example.

Finally, it is noteworthy to highlight that NiSe and CoSe also exhibit unusual topological electronic states and optical features (viz., multiple topological Dirac nodal-line structures and hyperbolic electromagnetic response), bringing exciting new perspectives in the field of nanophotonics and topological materials.

References

[1] a) G. Baffou, F. Cichos, R. Quidant, Applications and challenges of thermoplasmonics. *Nat. Mater.* 2020, **19**, 946, 10.1038/s41563-020-0740-6;

b) Y. Liu, J. Liu, Q. Zhang, Q. Zhu, X. Liu, Z. Wang, Z. Dai, CuO/Ag2S/CuS Nanohybrids-Integrated Photoelectric and Photothermal Effects for Ultrasensitive Detection of Inorganic Pyrophosphatase. *Adv. Funct. Mater.* 2022, **32**, 2106854, 10.1002/adfm.202106854;

c) L. Uson, C. Yus, G. Mendoza, E. Leroy, S. Irusta, T. Alejo, D. García-Domingo, A. Larrea, M. Arruebo, R. Arenal, V. Sebastian, Nanoengineering Palladium Plasmonic Nanosheets Inside Polymer Nanospheres for Photothermal Therapy and Targeted Drug Delivery. *Adv. Funct. Mater.* 2022, **32**, 2106932, 10.1002/adfm.202106932;

d) Q. Yu, T. Peng, J. Zhang, X. Liu, Y. Pan, D. Ge, L. Zhao, F. Rosei, J. Zhang, Cu2−xSx Capped AuCu Nanostars for Efficient Plasmonic Photothermal Tumor Treatment in the Second Near-Infrared Window. *Small* 2022, **18,** 10.1002/smll.202103174;

e) Q. Xiang, C. Yang, Y. Luo, F. Liu, J. Zheng, W. Liu, H. Ran, Y. Sun, J. Ren, Z. Wang, Near-Infrared II Nanoadjuvant-Mediated Chemodynamic, Photodynamic, and Photothermal Therapy Combines Immunogenic Cell Death with PD-L1 Blockade to Enhance Antitumor Immunity. *Small* 2022, **18**, 2107809, 10.1002/smll.202107809;

f) B. Shan, H. Liu, L. Li, Y. Lu, M. Li, Near-Infrared II Plasmonic Phototheranostics with Glutathione Depletion for Multimodal Imaging-Guided Hypoxia-Tolerant Chemodynamic-Photocatalytic-Photothermal Cancer Therapy Triggered by a Single Laser. *Small* 2022, **18**, 2105638, 10.1002/smll.202105638.

[2] a) X. Liu, Y. Yang, M. Ling, R. Sun, M. Zhu, J. Chen, M. Yu, Z. Peng, Z. Yu, X. Liu, Near-Infrared II Light-Triggered Robust Carbon Radical Generation for Combined Photothermal and Thermodynamic Therapy of Hypoxic Tumors, *Adv. Funct. Mater.* 2021, **31**, 2101709, 10.1002/adfm.202101709;

b) B. Tian, S. Liu, L. Feng, S. Liu, S. Gai, Y. Dai, L. Xie, B. Liu, P. Yang, Y. Zhao, Renal-Clearable Nickel-Doped Carbon Dots with Boosted Photothermal Conversion Efficiency for Multimodal Imaging-Guided Cancer Therapy in the Second Near-Infrared Biowindow. *Adv. Funct. Mater.* 2021, **31**, 2100549, 10.1002/adfm.202100549;

c) P. Ye, F. Li, J. Zou, Y. Luo, S. Wang, G. Lu, F. Zhang, C. Chen, J. Long, R. Jia, M. Shi, Y. Wang, X. Cheng, G. Ma, W. Wei, In Situ Generation of Gold Nanoparticles on Bacteria-Derived Magnetosomes for Imaging-Guided Starving/Chemodynamic/Photothermal Synergistic Therapy against Cancer. *Adv. Funct. Mater.* 2022, **32**, 2110063, 10.1002/adfm.202110063;

d) R. Zheng, Q. Zhao, W. Qing, S. Li, Z. Liu, Q. Li, Y. Huang, Cu2−xSx Capped AuCu Nanostars for Efficient Plasmonic Photothermal Tumor Treatment in the Second Near-Infrared Window. *Small* 2022, **18**, 2103174, 10.1002/smll.202103174.

[3] Y. An, Y. Nam, Closed-loop control of neural spike rate of cultured neurons using a thermoplasmonics-based photothermal neural stimulation. *J. Neural Eng.* 2021, **18**, 066002, 10.1088/1741-2552/ac3265.

[4] Q. Bai, M. Liang, W. Wu, C. Zhang, X. Li, M. Liu, D. Yang, W. W. Yu, Q. Hu, L. Wang, F. Du, N. Sui, Z. Zhu, Plasmonic Nanozyme of Graphdiyne Nanowalls Wrapped Hollow Copper Sulfide Nanocubes for Rapid Bacteria-Killing. *Adv. Funct. Mater.* 2022, **32**, 2112683, 10.1002/adfm.202112683.

[5] M. Sun, Z. Ji, L. He, C. Zhao, L. Ma, X. Xu, E. J. Cornel, Z. Fan, X. Xu, Instant Intracellular Delivery of miRNA via Photothermal Effect Induced on Plasmonic Pyramid Arrays. *Adv. Funct. Mater.* 2022, **32**, 2107999, 10.1002/adfm.202107999.

[6] a) G. Qiu, Z. Gai, L. Saleh, J. Tang, T. Gui, G. A. Kullak-Ublick, J. Wang, Thermoplasmonic-Assisted Cyclic Cleavage Amplification for Self-Validating Plasmonic Detection of SARS-CoV-2. *ACS Nano* 2021, **15**, 7536 10.1021/acsnano.1c00957;

b) G. Qiu, Z. Gai, Y. Tao, J. Schmitt, G. A. Kullak-Ublick, J. Wang, Dual-Functional Plasmonic Photothermal Biosensors for Highly Accurate Severe Acute Respiratory Syndrome Coronavirus 2 Detection. *ACS Nano* 2020, **14**, 5268, 10.1021/acsnano.0c02439.

[7] Z. Li, Z. Ye, L. Han, Q. Fan, C. Wu, D. Ding, H. L. Xin, N. V. Myung, Y. Yin, Polarization-Modulated Multidirectional Photothermal Actuators. *Adv. Mater.* 2021, **33**, 2006367, 10.1002/adma.202006367.

[8] A. Naldoni, Z. A. Kudyshev, L. Mascaretti, S. P. Sarmah, S. Rej, J. P. Froning, O. Tomanec, J. E. Yoo, D. Wang, Š. Kment, T. Montini, P. Fornasiero, V. M. Shalaev, P. Schmuki, A. Boltasseva, R. Zbořil, Solar Thermoplasmonic Nanofurnace for High-Temperature
Heterogeneous Catalysis, *Nano Lett.* 2020, **20**, 3663, 10.1021/acs.nanolett.0c00594.

[9] a) L. Mascaretti, A. Schirato, R. Zbořil, Š. Kment, P. Schmuki, A. Alabastri, A. Naldoni, Solar steam generation on scalable ultrathin thermoplasmonic TiN nanocavity arrays, *Nano Energy* 2021, **83**, 105828, 10.1016/j.nanoen.2021.105828;

b) Y. Lin, H. Xu, X. Shan, Y. Di, A. Zhao, Y. Hu, Z. Gan, Solar steam generation based on the photothermal effect: from designs to applications, and beyond, *J. Mater. Chem. A* 2019, **7**, 19203, 10.1039/C9TA05935K;

c) X. Han, L. V. Besteiro, C. S. L. Koh, H. K. Lee, I. Y. Phang, G. C. Phan-Quang, J. Y. Ng, H. Y. F. Sim, C. L. Lay, A. Govorov, X. Y. Ling, Intensifying Heat Using MOF-Isolated Graphene for Solar-Driven Seawater Desalination at 98% Solar-to-Thermal Efficiency, *Adv. Funct. Mater.* 2021, **31**, 2008904, 10.1002/adfm.202008904;

d) H. Zhang, X. Shen, E. Kim, M. Wang, J. H. Lee, H. Chen, G. Zhang, J. K. Kim, Integrated Water and Thermal Managements in Bioinspired Hierarchical MXene Aerogels for Highly Efficient Solar-Powered Water Evaporation, *Adv. Funct. Mater.* 2022, **32**, 2111794, 10.1002/adfm.202111794;

e) M. S. Irshad, N. Arshad, X. Wang, H. R. Li, M. Q. Javed, Y. Xu, L. A. Alshahrani, T. Mei, J. Li, Intensifying Solar Interfacial Heat Accumulation for Clean Water Generation Excluding Heavy Metal Ions and Oil Emulsions, *Sol. RRL* 2021, **5**, 2100427, 10.1002/solr.202100427;

f) M. S. Irshad, X. Wang, A. Abbas, F. Yu, J. Li, J. Wang, T. Mei, J. Qian, S. Wu, M. Q. Javed, Salt-resistant carbon dots modified solar steam system enhanced by chemical advection, *Carbon* 2021, **176**, 313, 10.1016/j.carbon.2021.01.140;

g) M. S. Irshad, X. Wang, M. S. Abbasi, N. Arshad, Z. Chen, Z. Guo, L. Yu, J. Qian, J. You, T. Mei, Semiconductive, Flexible MnO2 NWs/Chitosan Hydrogels for
Efficient Solar Steam Generation, *ACS Sustainable Chem. Eng.* 2021, **9**, 3887, 10.1021/acssuschemeng.0c08981;

h) S.-L. Loo, L. Vásquez, M. Zahid, F. Costantino, A. Athanassiou, D. Fragouli, 3D Photothermal Cryogels for Solar-

Driven Desalination, *ACS Appl. Mater. Interfaces* 2021, **13**, 263, 10.1021/acsami.1c05087.

[10] a) A. Politano, A. Cupolillo, G. Di Profio, H. Arafat, G. Chiarello, E. Curcio, When plasmonics meets membrane technology, *J. Phys.: Condens. Matter* 2016, **28**, 363003, 10.1088/0953-8984/28/36/363003;

b) D. Elmaghraoui, A. Politano, S. Jaziri, Photothermal response of plasmonic nanofillers for membrane distillation, *J. Chem. Phys.* 2020, **152**, 114102, 10.1063/1.5139291;

c) A. Politano, P. Argurio, G. Di Profio, V. Sanna, A. Cupolillo, S. Chakraborty, H. A. Arafat, E. Curcio, Photothermal Membrane Distillation for Seawater Desalination, *Adv. Mater.* 2017, 29, 1603504, 10.1002/adma.201603504;

d) A. Politano, G. Di Profio, E. Fontananova, V. Sanna, A. Cupolillo, E. Curcio, Overcoming temperature polarization in membrane distillation by thermoplasmonic effects activated by Ag nanofillers in polymeric membranes, *Desalination* 2019, **451**, 192, 10.1016/j.desal.2018.03.006;

e) Y. Z. Tan, H. Wang, L. Han, M. B. Tanis-Kanbur, M. V. Pranav, J. W. Chew, Photothermal-enhanced and fouling-resistant membrane for solar-assisted membrane distillation, *J. Membr. Sci.* 2018, **565**, 254, 10.1016/j.memsci.2018.08.032.

[11] F. Leon, A. Ramos, J. Vaswani, C. Mendieta, S. Brito, Climate Change Mitigation Strategy through Membranes Replacement and Determination Methodology of Carbon Footprint in Reverse Osmosis RO Desalination Plants for Islands and Isolated Territories, *Water* 2021, **13**, 293, 10.3390/w13030293.

[12] L. Rosa, D. D. Chiarelli, M. C. Rulli, J. Dell'Angelo, P. D'Odorico, Global agricultural economic water scarcity, *Sci. Adv.* 2020, **6**, eaaz6031, 10.1126/sciadv.aaz6031.

[13] a) K. Hainsch, K. Löffler, T. Burandt, H. Auer, P. C. del Granado, P. Pisciella, S. Zwickl-Bernhard, Energy transition scenarios: What policies, societal attitudes, and technology developments will realize the EU Green Deal? *Energy* 2022, **239**, 122067, 10.1016/j.energy.2021.122067;

b) M. S. Zafar, M. Zahid, A. Athanassiou, D. Fragouli, Biowaste-Derived Carbonized Bone for Solar Steam Generation and Seawater Desalination, *Adv. Sustainable Syst.* 2021, **5**, 2100031, 10.1002/adsu.202100031.

[14] a) N. Mir, Y. Bicer, Thermodynamic modeling of a combined photo-electrodialysis-chloralkali system for sustainable desalination, *Desalination* 2021, **499**, 114822, 10.1016/j.desal.2020.114822;

b) X. Su, D. Hao, M. Sun, T. Wei, D. Xu, X. Ai, X. Guo, T. Zhao, L. Jiang, Nature Sunflower Stalk Pith with Zwitterionic Hydrogel Coating for Highly Efficient and Sustainable Solar Evaporation, *Adv. Funct. Mater.* 2022, **32**, 2108135, 10.1002/adfm.202108135;

c) Z. C. Xiong, Y. J. Zhu, Z. Y. Wang, Y. Q. Chen, H. P. Yu, Tree-Inspired Ultralong Hydroxyapatite Nanowires-Based Multifunctional Aerogel with Vertically Aligned Channels for Continuous Flow Catalysis, Water Disinfection, and Solar Energy-Driven Water Purification, *Adv. Funct. Mater.* 2022, **32**, 2106978, 10.1002/adfm.202106978.

[15] a) A. Siefan, E. Rachid, N. Elashwah, F. AlMarzooqi, F. Banat, R. van der Merwe, Desalination via solar membrane distillation and conventional membrane distillation: Life cycle assessment case study in Jordan, *Desalination* 2022, **522**, 115383, 10.1016/j.desal.2021.115383;

b) Q. Ma, Z. Xu, R. Wang, Distributed solar desalination by membrane distillation: current status and future perspectives, *Water Res.* 2021, **198**, 117154, 10.1016/j.watres.2021.117154.

[16] a) A. Ali, R. A. Tufa, F. Macedonio, E. Curcio, E. Drioli, Membrane technology in renewable-energy-driven desalination, *Renewable Sustainable Energy Rev.* 2018, **81**, 1, 10.1016/j.rser.2017.07.047;

b) H. Lu, W. Shi, F. Zhao, W. Zhang, P. Zhang, C. Zhao, G. Yu, High-Yield and Low-Cost Solar Water Purification via Hydrogel-Based Membrane Distillation, *Adv. Funct. Mater.* 2021, **31**, 2101036, 10.1002/adfm.202101036.

[17] a) E. Curcio, E. Drioli, Membrane Distillation and Related Operations—A Review, *Sep. Purif. Rev.* 2005, **34**, 35, 10.1081/SPM-200054951;
b) I. Hitsov, T. Maere, K. De Sitter, C. Dotremont, I. Nopens, Modelling approaches in membrane distillation: A critical review, *Sep. Purif. Technol.* 2015, **142**, 48, 10.1016/j.seppur.2014.12.026.
[18] a) R. Miladi, N. Frikha, A. Kheiri, S. Gabsi, Energetic performance analysis of seawater desalination with a solar membrane distillation, *Energy Convers. Manag.* 2019, **185**, 143, 10.1016/j.enconman.2019.02.011;
b) Q. Li, L. J. Beier, J. Tan, C. Brown, B. Lian, W. Zhong, Y. Wang, C. Ji, P. Dai, T. Li, P. Le Clech, H. Tyagi, X. Liu, G. Leslie, R. A. Taylor, An integrated, solar-driven membrane distillation system for water purification and energy generation, *Appl. Energy* 2019, **237**, 534, 10.1016/j.apenergy.2018.12.069;
c) A. Abdel-Karim, J. M. Luque-Alled, S. Leaper, M. Alberto, X. Fan, A. Vijayaraghavan, T. A. Gad-Allah, A. S. El-Kalliny, G. Szekely, S. I. A. Ahmed, S. M. Holmes, P. Gorgojo, PVDF membranes containing reduced graphene oxide: Effect of degree of reduction on membrane distillation performance, *Desalination* 2019, **452**, 196, 10.1016/j.desal.2018.11.014;
d) L. García-Fernández, B. Wang, M. C. García-Payo, K. Li, M. Khayet, Morphological design of alumina hollow fiber membranes for desalination by air gap membrane distillation, *Desalination* 2017, **420**, 226, 10.1016/j.desal.2017.07.021;
e) L. Eykens, I. Hitsov, K. De Sitter, C. Dotremont, L. Pinoy, B. Van der Bruggen, Direct contact and air gap membrane distillation: Differences and similarities between lab and pilot scale, *Desalination* 2017, **422**, 91, 10.1016/j.desal.2017.08.018.
[19] A. Matin, T. Laoui, W. Falath, M. Farooque, Fouling control in reverse osmosis for water desalination & reuse: Current practices & emerging environment-friendly technologies, *Sci. Total Environ.* 2021, **765**, 142721, 10.1016/j.scitotenv.2020.142721.
[20] A. Anvari, A. A. Yancheshme, K. M. Kekre, A. Ronen, State-of-the-art methods for overcoming temperature polarization in membrane distillation process: A review, *J. Membr. Sci.* 2020, **616**, 118413, 10.1016/j.memsci.2020.118413.
[21] A. G. Razaqpur, Y. Wang, X. Liao, Y. Liao, R. Wang, Progress of photothermal membrane distillation for decentralized desalination: A review, *Water Res.* 2021, **201**, 117299, 10.1016/j.watres.2021.117299.
[22] a) H. Ye, X. Li, L. Deng, P. Li, T. Zhang, X. Wang, B. S. Hsiao, Silver Nanoparticle-Enabled Photothermal Nanofibrous Membrane for Light-Driven Membrane Distillation, *Ind. Eng. Chem. Res.* 2019, **58**, 3269, 10.1021/acs.iecr.8b04708;
b) M. Gao, C. K. Peh, F. L. Meng, G. W. Ho, Photothermal Membrane Distillation toward Solar Water Production, *Small Methods* 2021, **5**, 2001200, 10.1002/smtd.202001200.
[23] G. V. Naik, V. M. Shalaev, A. Boltasseva, Alternative Plasmonic Materials: Beyond Gold and Silver, *Adv. Mater.* 2013, **25**, 3264, 10.1002/adma.201205076.
[24] Y. Li, C. Lin, Z. Wu, Z. Chen, C. Chi, F. Cao, D. Mei, H. Yan, C. Y. Tso, C. Y. H. Chao, B. Huang, Solution-Processed All-Ceramic Plasmonic Metamaterials for Efficient Solar–Thermal Conversion over 100–727 °C, *Adv. Mater.* 2021, **33**, 2005074, 10.1002/adma.202005074.
[25] D. B. O'Neill, S. K. Frehan, K. Zhu, E. Zoethout, G. Mul, E. C. Garnett, A. Huijser, S. H. C. Askes, Ultrafast Photoinduced Heat Generation by Plasmonic HfN Nanoparticles, *Adv. Opt. Mater.* 2021, **9**, 2100510, 10.1002/adom.202100510.
[26] J. Yang, L. Sun, S. Hui, P. Zhang, J. Li, D. Wang, X. Wang, S. Jiang, Ag functionalized SnS2 with enhanced

photothermal activity for safe and efficient wound disinfection, *Biomater. Sci.* 2021, **9**, 4728, 10.1039/D1BM00429H.

[27] S. Lee, L. Truong, M.-J. Lee, S.-H. Chun, Comparative Study of SnSe2 Exfoliation and the Photothermal Current from the Products, *Cryst. Growth Des.* 2021, **21**, 6648, 10.1021/acs.cgd.1c00917.

[28] Z. Xie, Y. Duo, Z. Lin, T. Fan, C. Xing, L. Yu, R. Wang, M. Qiu, Y. Zhang, Y. Zhao, The Rise of 2D Photothermal Materials beyond Graphene for Clean Water Production, *Adv. Sci.* 2020, **7**, 1902236, 10.1002/advs.201902236.

[29] C. Liu, S. Sun, Q. Feng, G. Wu, Y. Wu, N. Kong, Z. Yu, J. Yao, X. Zhang, W. Chen, Z. Tang, Y. Xiao, X. Huang, A. Lv, C. Yao, H. Cheng, A. Wu, T. Xie, W. Tao, Arsenene Nanodots with Selective Killing Effects and their Low-Dose Combination with ß-Elemene for Cancer Therapy, *Adv. Mater.* 2021, **33**, 2102054, 10.1002/adma.202102054.

[30] J. Ouyang, L. Zhang, L. Li, W. Chen, Z. Tang, X. Ji, C. Feng, N. Tao, N. Kong, T. Chen, Enhanced Potassium-Ion Storage of the 3D Carbon Superstructure by Manipulating the Nitrogen-Doped Species and Morphology, *Nano-Micro Lett.* 2021, **13**, 1, 10.1007/s40820-020-00525-y.

[31] a) X. Fan, Y. Ding, Y. Liu, J. Liang, Y. Chen, Plasmonic Ti3C2Tx MXene Enables Highly Efficient Photothermal Conversion for Healable and Transparent Wearable Device, *ACS Nano* 2019, **13**, 8124, 10.1021/acsnano.9b03161;

b) K. Chaudhuri, M. Alhabeb, Z. Wang, V. M. Shalaev, Y. Gogotsi, A. Boltasseva, Highly Broadband Absorber Using Plasmonic Titanium Carbide (MXene), *ACS Photonics* 2018, **5**, 1115, 10.1021/acsphotonics.7b01439.

[32] a) E. Sachet, C. T. Shelton, J. S. Harris, B. E. Gaddy, D. L. Irving, S. Curtarolo, B. F. Donovan, P. E. Hopkins, P. A. Sharma, A. L. Sharma, Dysprosium-doped cadmium oxide as a gateway material for mid-infrared plasmonics, *Nat. Mater.* 2015, **14**, 414, 10.1038/nmat4203;

b) K. Sun, W. Xiao, S. Ye, N. Kalfagiannis, K. S. Kiang, C. de Groot, O. L. Muskens, Embedded Metal Oxide Plasmonics Using Local Plasma Oxidation of AZO for Planar Metasurfaces, *Adv. Mater.* 2020, **32**, 2001534, 10.1002/adma.202001534;

c) Y. Wang, A. C. Overvig, S. Shrestha, R. Zhang, R. Wang, N. Yu, L. Dal Negro, Tunability of indium tin oxide materials for mid-infrared plasmonics applications, *Opt. Mater. Express* 2017, **7**, 2727, 10.1364/OME.7.002727;

d) A. Shabani, M. K. Nezhad, N. Rahmani, Y. K. Mishra, B. Sanyal, J. Adam, Revisiting the Optical Dispersion of Aluminum-Doped Zinc Oxide: New Perspectives for Plasmonics and Metamaterials, *Adv. Photonics Res.* 2021, **2**, 2000086, 10.1002/adpr.202000086.

[33] J. O. Island, G. A. Steele, H. S. J. van der Zant, A. Castellanos-Gomez, Environmental instability of few-layer black phosphorus, *2D Mater.* 2015, **2**, 011002, 10.1088/2053-1583/2/1/011002.

[34] V. Paolucci, G. D'Olimpio, C. N. Kuo, C. S. Lue, D. W. Boukhvalov, C. Cantalini, A. Politano, Self-Assembled SnO2/SnSe2 Heterostructures: A Suitable Platform for Ultrasensitive NO2 and H2 Sensing, *ACS Appl. Mater. Interfaces* 2020, **12**, 34362, 10.1021/acsami.0c07901.

[35] a) M. B. Cortie, M. D. Arnold, V. J. Keast, The Quest for Zero Loss: Unconventional Materials for Plasmonics, *Adv. Mater.* 2020, **32**, 1904532, 10.1002/adma.201904532;

b) T. Gong, J. N. Munday, Materials for hot carrier plasmonics, *Opt. Mater. Express* 2015, **5**, 2501, 10.1364/OME.5.002501.

[36] a) A. Rasmussen, T. Deilmann, K. S. Thygesen, Towards fully automated GW band structure calculations: What we can learn from 60.000 self-energy evaluations, *npj Comput. Mater.* 2021, **7**, 22, 10.1038/s41524-020-00480-7;

b) Y. Xu, L. Elcoro, Z.-D. Song, B. J. Wieder, M. Vergniory, N. Regnault, Y. Chen, C. Felser, B. A. Bernevig, High-

throughput calculations of magnetic topological materials, *Nature* 2020, **586**, 702, 10.1038/s41586-020-2837-0.

[37] A. Jain, S. P. Ong, G. Hautier, W. Chen, W. D. Richards, S. Dacek, S. Cholia, D. Gunter, D. Skinner, G. Ceder, Commentary: The Materials Project: A materials genome approach to accelerating materials innovation, *APL Mater.* 2013, **1**, 011002, 10.1063/1.4812323.

[38] a) C. Wang, G. Zhang, S. Huang, Y. Xie, H. Yan, The Optical Properties and Plasmonics of Anisotropic 2D Materials, *Adv. Opt. Mater.* 2020, **8**, 1900996, 10.1002/adom.201900996;

b) A. Nemilentsau, T. Low, G. Hanson, Anisotropic 2D Materials for Tunable Hyperbolic Plasmonics, *Phys. Rev. Lett.* 2016, **116**, 066804, 10.1103/PhysRevLett.116.066804.

[39] K. Korzeb, M. Gajc, D. A. Pawlak, Compendium of natural hyperbolic materials, *Opt. Express* 2015, **23**, 25406, 10.1364/OE.23.025406.

[40] S. Zhang, W. Shi, T. D. Siegler, X. Gao, F. Ge, B. A. Korgel, Y. He, S. Li, X. Wang, An All-Inorganic Colloidal Nanocrystal Flexible Polarizer, *Angew. Chem.* 2019, **131**, 8822, 10.1002/ange.201902240.

[41] H. Yang, H. Jussila, A. Autere, H.-P. Komsa, G. Ye, X. Chen, T. Hasan, Z. Sun, Optical Waveplates Based on Birefringence of Anisotropic TwoDimensional Layered Materials, *ACS Photonics* 2017, **4**, 3023, 10.1021/acsphotonics.7b00507.

[42] R. Dehbashi, K. S. Bialkowski, A. M. Abbosh, Uniqueness theorem and uniqueness of inverse problems for lossy anisotropic inhomogeneous structures with diagonal material tensors, *J. Appl. Phys.* 2017, **121**, 203103, 10.1063/1.4983768.

[43] Y. Song, V. Tran, J. Lee, Tuning Plasmon Resonance in Magnetoplasmonic Nanochains by Controlling Polarization and Interparticle Distance for Simple Preparation of Optical Filters, *ACS Appl. Mater. Interfaces* 2017, **9**, 24433, 10.1021/acsami.7b06977.

[44] X. Zhang, L. Guo, B. Zhang, J. Yu, Y. Wang, K. Wu, H.-j. Wang, M.-H. Lee, From silicates to oxonitridosilicates: improving optical anisotropy for phase-matching as ultraviolet nonlinear optical materials, *Chem. Commun.* 2021, **57**, 639, 10.1039/D0CC07269A.

[45] D. A. G. Bruggeman, Berechnung verschiedener physikalischer Konstanten von heterogenen Substanzen. I. Dielektrizitätskonstanten und Leitfähigkeiten der Mischkörper aus isotropen Substanzen, *Ann. Phys.* 1935, **416**, 636, 10.1002/andp.19354160705.

[46] F. Schneider, J. Draheim, R. Kamberger, U. Wallrabe, Process and material properties of polydimethylsiloxane (PDMS) for Optical MEMS, *Sens. Actuators, A* 2009, **151**, 95, 10.1016/j.sna.2009.01.026.

[47] B. Ung, Y. Sheng, Interference of surface waves in a metallic nanoslit, *Opt. Express* 2007, **15**, 1182, 10.1364/OE.15.001182.

[48] L. Landau, E. Lifshitz, L. Pitaevskii, *Electrodynamics of Continuous Media*, Pergamon Press, Oxford 1984.

[49] O. Levy, D. Stroud, Maxwell Garnett theory for mixtures of anisotropic inclusions: Application to conducting polymers, *Phys. Rev. B* 1997, **56**, 8035, 10.1103/PhysRevB.56.8035.

[50] A. Lalisse, G. Tessier, J. Plain, G. Baffou, Quantifying the Efficiency of Plasmonic Materials for Near-Field Enhancement and Photothermal Conversion, *J. Phys. Chem. C* 2015, **119**, 25518, 10.1021/acs.jpcc.5b09294.

[51] W. Hu, W. Zhen, M. Zhang, W. Wang, X. Jia, S. An, Y. Wang, Z. Guo, X. Jiang, Development of Nickel Selenide@polydopamine Nanocomposites for Magnetic Resonance Imaging Guided NIR-II Photothermal Therapy, *Adv. Healthcare Mater.* 2021, **10**, 2101542, 10.1002/adhm.202101542.

[52] J. J. Rehr, J. J. Kas, F. D. Vila, M. P. Prange, K. Jorissen, Parameter-free calculations of X-ray spectra with FEFF9, *Phys. Chem. Chem. Phys.* 2010, **12**, 5503, 10.1039/B926434E.

[53] Y. Pan, Y. Hang, X. Zhao, G. Liu, W. Jin, Optimizing separation performance and interfacial adhesion of PDMS/PVDF composite membranes for butanol recovery from aqueous solution, *J. Membr. Sci.* 2019, **579**, 210, 10.1016/j.memsci.2019.03.008.

[54] A. Alkhudhiri, N. Hilal, 3 - Membrane distillation-Principles, applications, configurations, design, and implementation, *Emerging Technologies for Sustainable Desalination Handbook* (Ed: V. G. Gude), Butterworth-Heinemann, Oxford 2018, p. 55, 10.1016/B978-0-12-815818-0.00003-5.

[55] T. Horseman, Y. Yin, K. S. S. Christie, Z. Wang, T. Tong, S. Lin, Wetting, Scaling, and Fouling in Membrane Distillation: State-of-the-art Insights on Fundamental Mechanisms and Mitigation Strategies, *ACS ES&T Eng.* 2021, **1**, 117, 10.1021/acsestengg.0c00025.

[56] C. Zhang, H. Q. Liang, Z. K. Xu, Z. Wang, Harnessing Solar-Driven Photothermal Effect toward the Water–Energy Nexus, *Adv. Sci.* 2019, **6**, 1900883, 10.1002/advs.201900883.

[57] D. Winter, J. Koschikowski, M. Wieghaus, Desalination using membrane distillation: Experimental studies on full scale spiral wound modules, *J. Membr. Sci.* 2011, **375**, 104, 10.1016/j.memsci.2011.03.030.

Chapter 5

Lithium recovery through WS_2 nanofillers-promoted solar photothermal membrane crystallization of LiCl

Keywords: Photothermal membrane crystallization; Photothermal nanosheets; Lithium recovery; Water-energy-raw materials nexus; Energy transition

Contents

Abstract

5.1 Introduction

5.2 Materials and methods

5.2.1 Materials and solvents

5.2.2 Ink

5.2.3 Membrane preparation

5.2.4 Membrane characterization

5.2.5 Photothermal membrane crystallization (PhMCr)

5.3 Results and discussion

5.3.1 High-concentration functional ink based on WS2 nanosheets
5.3.2 Light-to-heat conversion in WS2-based nanocomposite PVDF membranes
5.3.3 Nanocomposite membranes
5.3.4 Photothermal membrane crystallization

5.4 Conclusions

References

This chapter has been published as:

Santoro S., Aquino M., Rizza C., Occhiuzzi J., Mastrippolito D., D'Olimpio G., Avci A.H., De Santis J., Paolucci V., Ottaviano L., Lozzi L., Ronen A., Bar-Sadan M., Suk Han D., Politano A.; Curcio E. Lithium recovery through WS_2 nanofillers-promoted solar photothermal membrane crystallization of LiCl Desalination, 2023, 546-116186
https://doi.org/10.1016/j.desal.2022.116186

Abstract

The recovery of raw materials represents one of the greatest challenges for circular economy. Especially, the increased demand for lithium in the last years for its critical role for Li-ion batteries implies the need of a green technology for Li recovery able to address market requests. Here, we devise and implement a new technology exploiting on excitons-based light-to-heat conversion promoted by WS_2 nanofillers in nanocomposite polymeric membranes for sunlight-driven photothermal membrane crystallization, applied for the efficient extraction of lithium from Li-rich brines. The activation of photothermal effects of excitonic nanofillers in the PVDF-WS_2 nanocomposite enhances the evaporative flux of water under solar irradiation by 364%, triggering the heterogeneous nucleation and the crystallization of LiCl salt, once achieved the supersaturation. This new facile, economical, and green nanotechnology-enabled platform renews the interest for functional inks based on nanosheets of van der Waals semiconductors for the fabrication of functional nanocomposites, here exploited for the first time in the field of crystallization and the recovery of economically strategic minerals in a circular-economy paradigm. Moreover, these findings open up new opportunities for large-scale, efficient, and sustainable recovery of lithium (as well as other critical raw materials) for next-generation devices for the clean energy transition.

5.1. Introduction

Lithium (Li) represents a crucial driver of the energy transition towards sustainability away from fossil fuels, in consideration of its large exploitation in electrochemistry as cathode for batteries, owing to its high electrode potential (−3.05 eV) [1 , 2]. Nowadays, Li-ion batteries are recognized as a priority for energy storage in portable electronic devices and in electric vehicles [3]. Consequently, Li demand in the last 5 years has nearly doubled [4], with annual growth rates (AGR) of 24% [5]. Recently, both EU [6, 7] and USA [8] have listed Li as a critical raw material. Although it is present in more than 100 minerals [9], more than 60% of Li is stored as Li^+ cations in seawater (0.1–0.2 ppm) and hypersaline lakes (200 - 4000 ppm) called “salars”, mostly located in countries such as Chile, Bolivia, China, and USA [10]. Li extraction from ores is prohibitive, as it compromises the water-energy nexus by demanding an enormous amount of heat to upgrade the rock-minerals followed by Li dissolution in aqueous media [11 , 12]. On the other hand, Li-bearing brine mining could represent a viable approach [13], based on the exploitation of sunlight and wind to concentrate Li to ~6000 ppm lithium [14] after several fractionation steps carried out in different ponds to remove contaminants (e.g., Na, K, Mg, Ca) by precipitation [15]. Once the optimal

concentration of lithium chloride (LiCl) is achieved, the hyper-concentrated brine is treated with lime to induce Mg precipitation and, subsequently, with soda ash obtaining lithium carbonate (Li_2CO_3) [16 , 17]. Moreover, under the impulse of the circular economy, LiCl extracted from the anode electrode materials of spent lithium-ion batteries via leaching using hydrochloric acid represents an alternative resource [18].

Nevertheless, critical limitations of Li mining from brine are (i) the time-consuming concentration stage based on solar evaporation typically demanding 1-2 years, (ii) the need of vast areas for ponds, (iii) the low energetic efficiency (<40% [19], and (iv) the poor control associated to the inevitable dependence of the crystallization of the salt on meteorological conditions [20]. This scenario imposes a fast and radical re-design of the Li extraction from brine aimed to intensify the process without sacrificing the green approach, based on solar energy.

In this chapter of my PhD thesis, we show the capabilities for Li recovery enabled by membrane crystallization (MCr), recently emerged as a powerful technology able to drive an aqueous solution towards a specific degree of supersaturation by a controlled removal rate of the solvent under a partial pressure gradient [21]. Definitely, MCr promotes heterogeneous nucleation by appropriate tuning of the physicochemical properties of the membrane surface (i.e. contact angle, porosity, roughness) [22, 23] finely tuning the properties of the crystals (i.e. polymorphism, size and coefficient of variation) [24, 25]. Moreover, process optimization (mostly the identification of the optimal hydrodynamic conditions to control the rate of solvent removal and to avoid the precipitation of the crystals over the membrane) ensures the intensification of MCr process which can be easily integrated with other membrane units (i.e. Ultrafiltration, Microfiltration, Nanofiltration) enabling the recovery of crystallized salts from mother liquor [26 , 27]. However, the advantages of MCr technology related to the excellent control of the nucleation of crystals are obscured to date by several drawbacks, such as (i) the necessity of applying vacuum to sustain transmembrane flux until supersaturation in the presence of high solubility (as in the case of Li salts) [28], with the subsequent drastic reduction of water activity at high solute concentration [29] and (ii) the high energy costs related to the thermal demand for heating the feed solution [30]. Therefore, practical applications of MCr are elusive so far.

Herein, we provided a step-change advancement in MCr technology, totally based on the combination with renewable energy sources, such as sunlight, through the exploitation of light-to-heat conversion with photothermal nanofillers [31 , 32]. Specifically, we show that sunlight-driven MCr enables efficient solvent evaporation, with the facile achievement of supersaturation and

crystallization via heterogeneous nucleation on the surface of a membrane. Definitely, the platform of photothermal membrane crystallization (PhMCr) has a huge potential impact on the recovery of raw materials [31 , 32], as we demonstrate in the case-study example of Li, whose recuperation is strategic for the green energy transition [33].

The state-of-the-art solar evaporation process secures a preliminary concentration of Li-salts in the brine up to 6 wt%, but their direct extraction is hampered by the outstanding solubility of LiCl reaching approximately 20 $mol \cdot kg^{-1}$ (~845 $mg \cdot L^{-1}$) at 25 °C [34]. Therefore, a successive conversion of LiCl into Li_2CO_3 is necessary to facilitate the precipitation of Li-salts [34]. On the other hand, PhMCr has the capability to open new pathways for Li production, which is fully compatible with renewable energies.

To afford sustainability to the PhMCr technology, we also selected a photothermal filler able to overcome the current challenges of thermoplasmonics, i.e., (i) the use of Ag and Au, whose expensive cost strongly limits industrial scale-up [35 , 36] and (ii) the quest of materials enabling efficient light-to-heat conversion matching the energy range of solar radiation [37 , 38]. Usually, metallic or polar dielectric materials, characterized by a negative permittivity near their frequency resonance, are used for thermoplasmonics, with a light-to-heat conversion based on the excitation of surface plasmon or surface phonon polaritons, respectively. PhD thesis, we validate an alternative route, based on excitonic two-dimensional materials, based on Earth-abundant elements, able to achieve an efficient and sustainable all-dielectric platform for thermoplasmonics. Specifically, we implement PhMCr with hydrophobic microporous poly(vinylidene fluoride) (PVDF) membranes, loaded with tungsten disulfide (WS_2) nanofillers, introduced in the nanocomposite membrane by phase inversion through a high-concentration functional ink. The presence of excitonic nanofillers in the PVDF-WS_2 nanocomposite enhances the evaporative flux of water under solar irradiation by 364 %, triggering the heterogeneous nucleation and the crystallization of LiCl salt once supersaturation is achieved.

5.2 Materials and methods

5.2.1 Materials and solvents

PVDF Solef 6020 was kindly supplied by Solvay Solexis. LiCl, WS_2, 1- methyl-2-pyrrolidone (NMP), and ethanol were purchased by Sigma Aldrich.

5.2.2 Ink

A mixture of the WS_2 bulk crystal and the NMP was prepared in a predefined mass ratio [material/solvent]. A high pressure (up to 210 MPa) forces the passage of the liquid solution formed by NMP and WS_2 through a microchannel (diameter, d < 100 μm). The most relevant advantage over sonication and shear-mixing consists in the achievement of particularly high values of the velocity gradient (higher than 10^6 s^{-1}) in the entire fluid volume, not only locally. Further details on fluid dynamics methods to attain functional inks on 2D materials are reported in [39, 40]. A final concentration of 1–7 $g \cdot L^{-1}$ was achieved.

Atomic force microscopy (AFM) measurements were performed in air tapping mode with a Veeco Digital D5000 system, using tips with a spring constant of 3 $N \cdot m^{-1}$ and resonance frequencies in the 51–94 kHz range.

X-ray photoelectron spectroscopy (XPS) measurements were carried out with a PHI 1257 spectrometer, equipped with a monochromatic Al Kα source (hν = 1486.6 eV) with a resolution of 0.25 eV.

5.2.3 Membrane preparation

PVDF solutions were prepared by directly adding the polymeric powder to WS_2 ink with a concentration of the photothermal filler varying from 0 wt% to 1 wt%. The polymer concentration in the dope solution was fixed at 12.5 wt% and WS_2 concentration with respect to PVDF resulted in 0 wt% (M0), 3.5 wt% (M3.5), 5 wt% (M5) and 7 wt% (M7), respectively. The polymeric solutions were magnetically stirred overnight (100 rpm and 70 ◦C). Then, the homogeneous PVDF solutions were degassed for 2 h at 70 ◦C ensuring the removal of entrapped air. The photothermal membranes were prepared by casting the PVDF solutions on a glass plate by using a casting knife set at 0.3 mm of thickness. The nascent membranes were immersed in a coagulation bath (H_2O/ethanol 50/50 wt%/wt%) for 3 h. Then, the as-formed membranes were washed for 2 h in distilled water and dried for 8 h at 50 ◦C.

5.2.4 Membrane characterization

The morphology of the membranes was observed under a scanning electron microscope (SEM), Model QuantaFENG200, FEI Company. A thin gold layer was sputtered onto the membranes using a Quorum Q150 RS sputter (Quorum Technologies, Laughton, East Sussex, UK) to enhance their conductivity and prevent electrical charging. Membranes were submitted to freeze fracturing

the membranes in liquid nitrogen for the observation of the cross-section. Both membrane surfaces were observed. Measurements of pore size and bubble point were carried out with a PMI Capillary Flow Porometer Model CFP-1500AEXL (Porous Materials Inc., USA) under the management of the software Capwin (Porous Materials Inc., USA) by employing the wet up/dry-up method. Porewick® (surface tension 16 dyn·cm^{-1}) was used as wetting liquid and the results were processed by the software Caprep (Porous Materials Inc., USA). A CAM 200 contact angle meter (KSV Instruments, Finland) was employed to evaluate the membrane hydrophobicity according to the sessile drop method at ambient temperature. The porosity was appraised by the gravimetric method weighing the membrane before (dry) and after (wet) the immersion for 24 h in a liquid [41]. The porosity (ε) was calculated according to the following equation:

$$\varepsilon(\%) = \left\{ \frac{(W_W - W_d)/\rho_i}{\frac{W_d}{\rho_m} + (W_W - W_d)/\rho_i} \right\} \% \quad (1)$$

where W_W is the weight of the wet membrane, W_d is the weight of the dry membrane, ρ_i is the Fluorinert FC40 density (1.9 g·cm^{-3}) and ρm is the density of the membrane material estimated from the PVDF (1.78 g·cm^{-3} [42]) and WS_2 (7.5 g·cm^{-3} [43]) densities. Three measurements for each membrane were performed to calculate average values and standard deviation.

The Ultraviolet and visible (UV–Vis) absorption of the photothermal membrane was measured with a spectrophotometer analysis (Shimadzu UV-1601, Kyoto, Japan), whereas Raman spectra were collected with an NRS-5100 Confocal Raman Microscope (Jasco, Easton, USA) equipped with a laser emitting at a wavelength of 532 nm (20 mW) and objective lens of 5×, 20×, 100×.

Atomic absorption spectrometry (HR-CS AAS) was performed for the detection of WS_2 in a coagulation bath.

The photothermal efficiency of the membranes was evaluated by an Infrared (IR) camera (FLIR, model T660, USA) with a sensitivity < 0.02 ◦C and a resolution of 640 × 480 pixel.

5.2.5 Photothermal membrane crystallization (PhMCr)

Artificial Li-rich brine was prepared by dissolving LiCl in osmotized water (5.5 µS·m^{-1}; produced by PURELAB, Elga LabWater, UK) under magnetically stirring (8 h at 250 rpm, 50 ◦C). Pre-concentration experiments of saline solution of LiCl (1 M) by favoring the vaporization of the

water with M7 under the artificial solar radiation (1000 $W \cdot m^{-2}$) were performed obtaining a quasi-saturated brine ([LiCl] = 18 M) in 8 h. Experiments of Solar-driven PhMCr were carried out using distilled water and LiCl brine (with a molarity 18 M). The aqueous solutions (1 g) were displaced on the membranes (active area 3.14 cm^2) located in modules made of Polylactic acid (PLA), designed with Autodesk 123D® and printed with a 3D-printer (TEVO Tornado). In all the cases, experiments of solar-driven PhMCr were repeated 3 times after washing the membranes with distilled water. The mean values of the evaporation fluxes and the experimental errors were estimated. Experiments were conducted by exposing the PhMCr module to artificial radiation of a solar simulator (Abet Technologies, US) with an irradiance of 1 sun (1000 $W \cdot m^{-2}$) over a 35 mm diameter field, a temperature ranging from 19 to 28 ◦C, and a relative humidity of 47 ± 4 %. The evaporation rate was estimated by weighting using an analytical balance (Gilbertini, Model E 50 S/3) at intervals of 30 min. The temperature was measured by using a thermocouple (Sper Scientific 800024). The obtained crystals were collected from the PhMCr module and characterized by a Zeiss microscope, model AxioLab 1×.

5.3 Results and discussion

5.3.1 High-concentration functional ink based on WS2 nanosheets

Nanofillers of WS_2 were introduced in polymeric membranes via phase inversion. Definitely, exfoliated flakes produced with a lateral size control were uniformly dispersed by fluid-dynamics methods in a solvent compatible with the polymer, thereby yielding a homogeneous distribution of 2D crystals in a confined volumetric space. Actually, the concentration of the functional ink based on 2D crystals represents an open challenge for technology transfer. Contrary to mechanical exfoliation, unsuitable for mass production and industrial applications, liquid phase exfoliation (LPE) can be potentially scaled up to meet industrial needs in terms of both crystalline quality and quantity. The most widely used LPE process consists in exposing bulk layered material to ultrasonic waves in a solvent. The choice of the solvent is dictated by the properties of the layered material itself, i.e., the surface tension of the solvent should match the surface energy of the dispersed layered material. The LPE based on ultrasonication produces a heterogeneous mixture of single-, double-, multi-layered flakes, as well as a large amount of unexfoliated layered material. The yield (ratio in mass between the starting material and the final product) is well below 10 %. Ultrasonication requires a long processing time (e.g., from a few minutes up to a hundred hours) and a temperature control, because the material under processing is subject to strong local heating. Other drawbacks of the sonication method rely on the impracticality of producing layered materials

prone to oxidation in a closed-loop manufacturing line. Besides sonication, fluid-dynamics methods for the exfoliation of layered materials have recently emerged [39]. In the fluid-dynamics-assisted LPE, flakes of bulk crystals of layered materials can move with the liquid and, thus, they can be exfoliated repeatedly at different positions. This feature is intrinsically different from that of sonication, making it a potentially efficient technique for the scalable production of 2D materials. A LPE based on hydrodynamic forces enables the efficient transfer of energy from the liquid medium to the processed layered materials to achieve their exfoliation, while minimizing the fracture on the basal plane. Accordingly, layered crystals are exfoliated from the bulk counterpart and then dispersed into the solvent, without compromising their physicochemical and electronic properties. For the production of functionalized membranes for MCr, we produced dispersions of WS_2 nanosheets with a minimization of the turbulence, to decrease the effect of lateral force for the exfoliation, so as to obtain smaller lateral size flakes.

The adopted protocol ultimately leads to (i) a good mixing of WS_2 crystals and PVDF and (ii) a controlled thickness of flakes of WS_2 crystals, in contrast with mixed-matrix membranes produced by state-of-the-art techniques (see review in Ref. [44] and references therein) by using commercial nanoplatelets or powders of 2D crystals.

The WS_2 nanosheets in the functional ink display an average lateral size of (1.4 ± 0.1) μm (Fig. 5.1 b) and a thickness of (37 ± 6) nm (Fig. 5.1 c), based on experiments by scanning electron microscopy (Fig. 5.1 a) and atomic force microscopy (Fig. 5.1 d).

Another crucial challenge in the production of functional inks based on nanosheets of transition-metal dichalcogenides is the minimization of the inevitable oxidation of the nanosheets, due to (i) the presence of chalcogen vacancies formed during the exfoliation process and (ii) the enhanced surface-to-volume ratio in nanosheets compared to bulk crystals.

X-ray photoelectron spectroscopy (XPS) has the chemical specificity to reveal components related to WS_2, WS_2-x, WO_3, and SO_4 [45, 46, 47]. Especially, note that the WS_2-based functional ink produced by fluid-dynamics-assisted LPE has a reduced amount of surface tungsten oxide phases, as indicated by the reduced spectral weight of WO_3 in the region of W-4f (~7 %, Fig. 5.1 e). Remarkably, the SO_4-derived spectral component is <1 % of the total spectral area of the S-2p core level (Fig. 5.1 e), in contrast with values as high as 10 % reported in XPS experiments within the same experimental conditions for WS_2 nanosheets produced by sonication-assisted LPE with the same solvent [46]. Such an ideal condition was achieved, owing to the suppression of S vacancies formed in the fluid-dynamics-assisted LPE, as evident by the reduced weight of the WS_2-x spectral component, which represents just ~3 % of the total area of S-2p (Fig. 5.1 f).

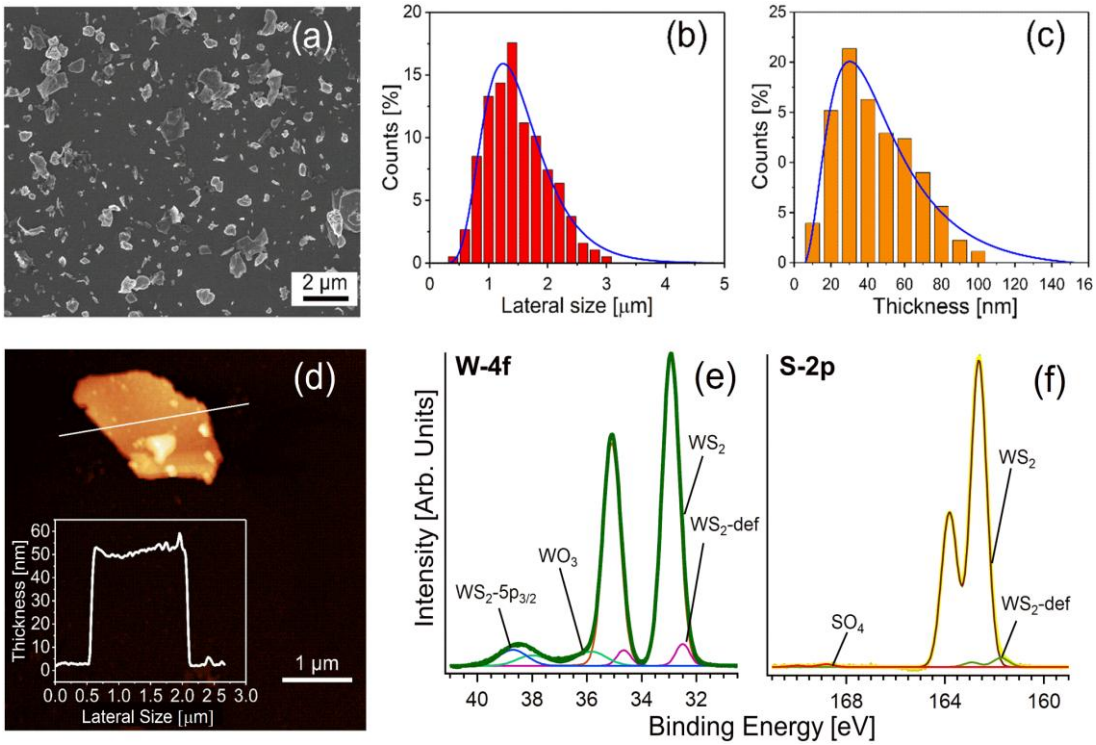


Figure 5.1. *(a) Representative SEM image of LPE-exfoliated WS_2 flakes. (b) Analysis of lateral size distribution of WS_2 flakes determined from SEM images. (c) Analysis of thickness distribution determined from AFM measurements. (d) Representative AFM image of WS_2 flakes. The height profile along the solid white line is reported in the inset. (e) W-4f and (f) S-2p core levels of WS_2 flakes.*

5.3.2 Light-to-heat conversion in WS2-based nanocomposite PVDF membranes

To assess the light-to-heat conversion of WS_2-based composite (i.e., PVDF loaded with WS_2 nanosheets), we evaluated the effective dielectric permittivity of the structure by exploiting a suitable multiscale approach [48]. We consider that the nanosheet longitudinal thickness d_z is smaller than the radiation wavelength λ, whereas its in-plane transverse sizes (d_x, d_y) are large compared to d_z and λ. In addition, we assume that the nanosheets are distant enough and are randomly dispersed in the host medium so that the effective electromagnetic response is given by a suitable average over all possible orientations [49]. Assuming these approximations, we evaluate the effective dielectric permittivity of the WS_2-based composite, i.e.

$$\epsilon_{eff} = \epsilon_h + \frac{2}{3} f\,(\epsilon_{WS2} - \epsilon_h) \qquad (2)$$

where f is the volume fraction of the inclusions, ϵ_h is the dielectric constant of the host material (ϵ_h= 2.03) [50], and ϵ_{WS2} is the WS_2 dielectric permittivity. We derive Eq. (2) for uniform

orientation distribution, so that the WS_2-based composite exhibits an average isotropic response described by the scalar dielectric function ϵeff.

In Fig. 5.2 a, we report the bulk dielectric permittivity ϵ_{WS2} (λ) in the optical range, retrieved by a Kramers-Kronig analysis of the experimental reflectivity spectra at room temperature [51]. WS_2, being a van der Waals semiconductor, displays an excitation spectrum exhibiting high-permittivity excitonic resonances in the visible region [52]. More precisely, three prominent resonances are evident (Fig. 5.2 a) at a wavelength of 0.64, 0.53, and 0.47 μm (corresponding to energies of 1.94, 2.34, and 2.64 eV, respectively), assigned to A, B, and C excitons, respectively [53, 54].

Notably, excitonic materials have been recently suggested to support the mimicking of surface plasmons [55], thus paving their use for all dielectric thermos-nanophotonics based on Mie resonances [56].

Here, we estimate the light-to-heat conversion by describing the electromagnetic response of the considered nanocomposite with the dielectric permittivity reported in Eq. (2). By using the dielectric function reported in Fig. 5.2 a, we get the effective dielectric permittivity as a function of the WS_2 volume fraction (see Fig. 5.2 b–c). Similarly to the WS_2 dielectric function ϵ_{WS2}, the effective permittivity Ɛeff exhibits three positive-dielectric resonances at about 0.47, 0.53, 0.64 μm (2.64, 2.34, and 1.94 eV, respectively). Considering a monochromatic plane wave impinging orthogonally on a slab made of the WS_2-based composite, we analytically evaluate the reflectivity R, the transmissivity T and the absorptivity A (with A = 1-T-R, according to the energy conservation law). In Fig. 5.2 d–e, we report the reflectivity and the absorptivity spectra, respectively, as a function of f for a finite slab thickness. It is worth noting that the absorption and, hence, the light-heat conversion is very high at any optical frequency ($A > 0.8$ for $f > 0.05$ and the considered optical frequency range) as shown in Fig. 5.2 e. In addition, the absorption efficiency of the WS_2– based nanocomposite can be comparable with those of the standard photothermal.

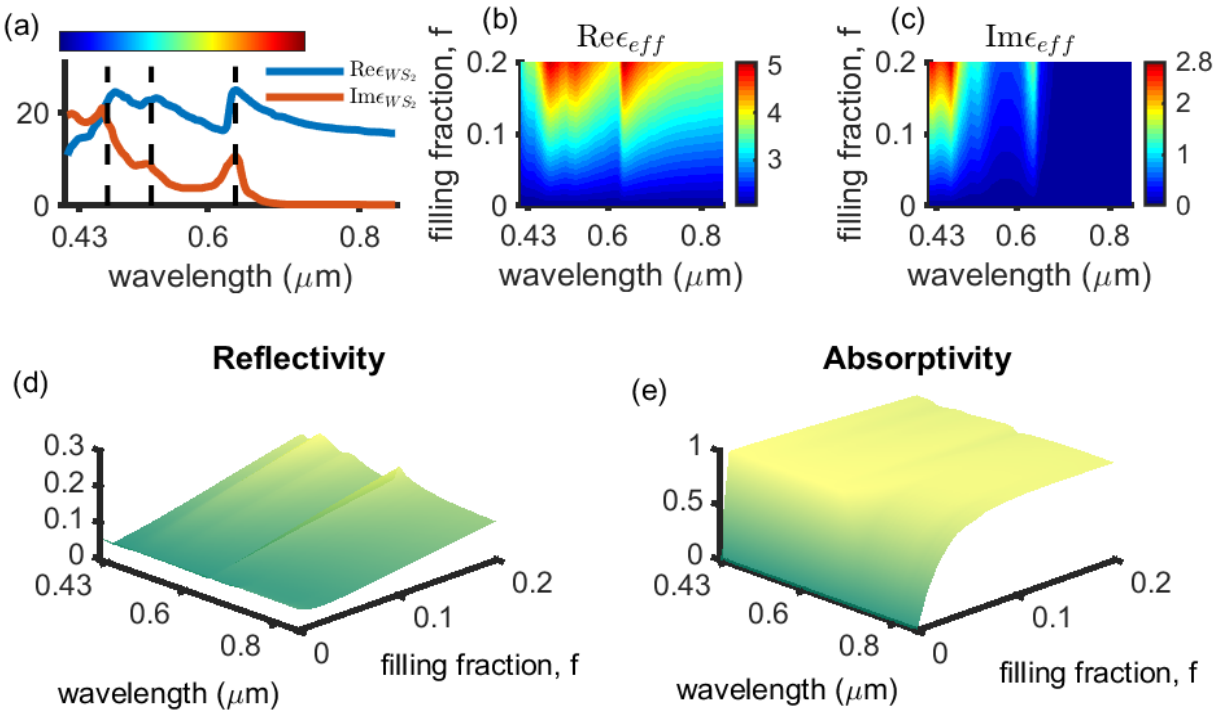


Figure 5.2. *(a) The relative dielectric function of WS_2 versus the wavelength λ in the optical range, with the top axis visualizing the corresponding zone of the electromagnetic spectrum in the visible. The real and the imaginary components of the dielectric function of WS_2 are depicted in blue and red, respectively. (b-c) The effective dielectric function of the WS_2 -based composite (PVDF loaded with WS_2 nanosheets) as a function of λ and the WS_2 volume fraction f. (d) Reflectivity and (e) absorptivity of a nanocomposite slab (with a finite thickness, here taken as 55 μm) as a function of λ and f. (For interpretation of the references to color in this figure legend, the reader is referred to the web version of this article.)*

Therefore, according to our theoretical modeling, WS_2 could represent a suitable platform for solar-driven PhMCr technology, for which the progressive evaporation of water would bring the aqueous LiCl solution towards supersaturation, which is the driving force to crystallization (Fig. 5.3 b). According to the Classical Nucleation Theory (CNT), crystallization is a thermally activated process, and an Arrhenius-like correlation exists between the nucleation rate (N) and the Gibbs energy barrier (ΔG*) corresponding to the formation of the critical nucleus size (i.e. a cluster having the same probability to growth or dissolve):

$$N = \Gamma \cdot e^{-\frac{\Delta G^*}{k \cdot T}} \qquad (3)$$

where Γ is a pre-exponential kinetic parameter and k is the Boltzmann's constant. Homogeneous nucleation takes place in the bulk of the supersaturated solution. The random motion minimizes the probability of effective interactions between the solutes, resulting in a high ΔG* [57]. Conversely, the presence of a foreign solid surface – i.e., a membrane - locally decreases the energy required to

generate a critical nucleus (i.e., heterogeneous nucleation) as a result of (i) the porous and rough surface morphology, which offers sub-micrometric cavities facilitating an ordered assembly of solute molecules [57], and (ii) weak and reversible chemical interactions between membrane - solute interactions [58]. For a porous membrane, the ratio of the Gibbs energy barrier for heterogeneous nucleation occurring at the membrane interface (ΔG_{het}*) to the one for homogeneous nucleation occurring in the bulk of the solution (ΔG_{hom}*) is estimated as [23].

$$\frac{\Delta G^*_{het}}{\Delta G^*_{hom}} = \frac{1}{4}(2 + cos\theta)(1 - cos\theta)^2 \left[1 - \epsilon \frac{(1+cos\theta)^2}{(1-cos\theta)^2}\right]^3 \quad (4)$$

where θ is the contact angle and ϵ the porosity, both of them tunable by acting on the morphology of the membrane surface [41].

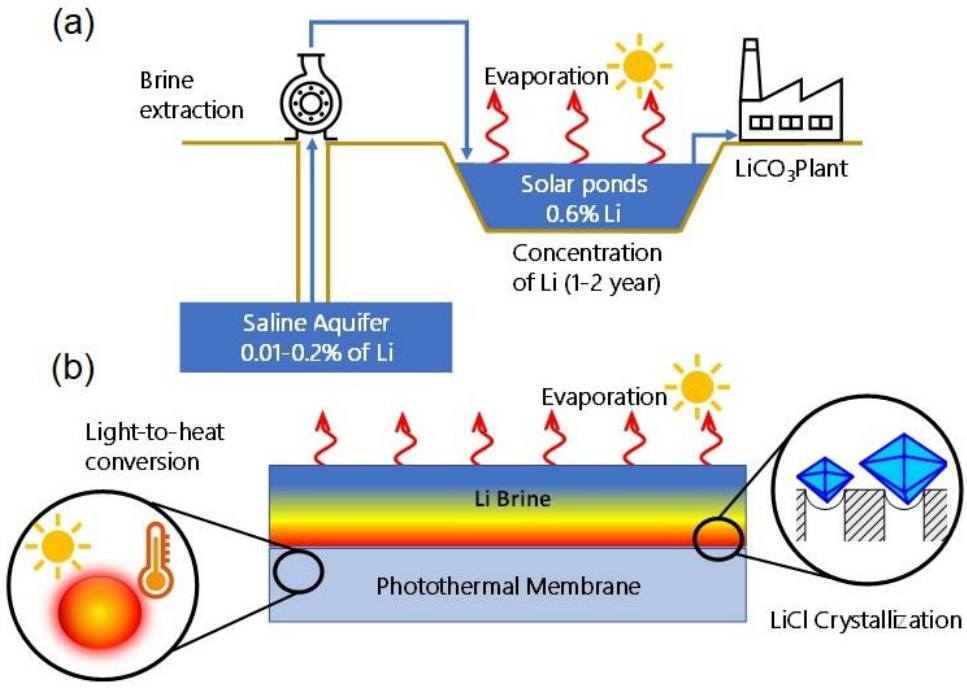


Figure 5.3. *(a) Conventional process of Li extraction; (b) Solar-driven Photothermal Membrane Crystallization (PhMCr).*

5.3.3 Nanocomposite membranes

Microporous hydrophobic nanocomposite membranes were produced by non-solvent induced phase separation (NIPS, see Materials and methods). Morphological analyses of the cross-section of bare PVDF and PVDF-WS_2 membranes revealed a homogeneous spherulitic morphology with thicknesses of 55 ± 3 µm (see SEM images in Fig. 5.4 a–b).

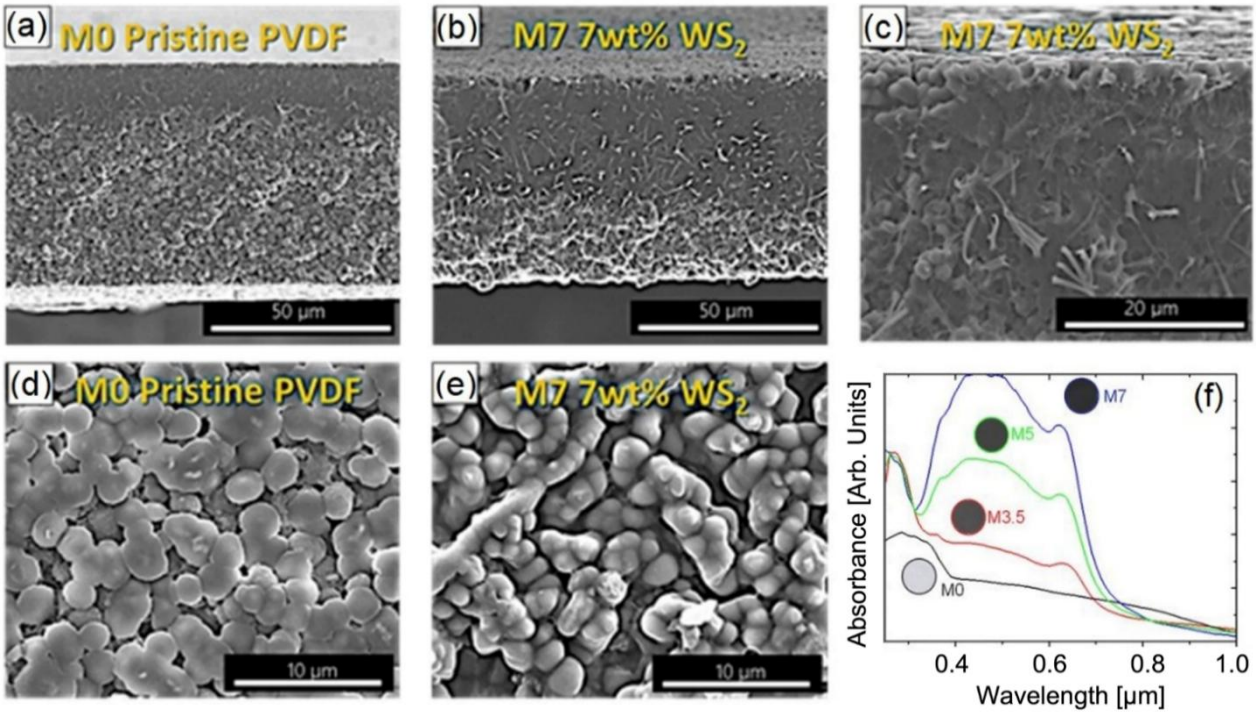


Figure 5.4. *(a–b) SEM image of the cross-sections of pristine PVDF membrane (M0) and PVDF-7 wt% WS_2 (M7). Magnification: 2500×. (c) Detailed microstructure of PVDF-7 wt% WS_2 (M7). Magnification: 6000. (d–e) Top surface of pristine PVDF membrane (M0) and PVDF-7 wt% WS_2 (M7) (Magnification 10,000×). (f) UV–Vis and appearance of the membranes at different WS_2 loading.*

The formation of the spherulitic structures is attributed to the semi-crystalline behavior of the fluoropolymer [59] and the employment of hydroalcoholic solution as a coagulation bath [60], which is responsible for delayed demixing. In fact, the phase inversion of glassy polymers is usually governed by liquid/liquid (L/L) demixing; whereas in the case of a semi-crystalline polymer, such as PVDF, the phase inversion is undertaken by solid/liquid (S/L) delayed demixing leading to particulate morphologies consisting of interlinked semicrystalline spherulites [60]. Moreover, it is known that the presence of alcohols in the coagulation bath can modulate the supramolecular architectures by delaying L/L demixing and favoring the PVDF crystallization shifting the morphology of the membrane from cellular to globular [61]. Furthermore, both the

membrane surfaces displayed a spherulitic morphology made up of globules of size in the range of 1–4 μm (Fig. 5.4 d–e). Interestingly, bare PVDF (denoted as "M0") presented nuclei of a mean size of about 2.4 μm, reduced to ca. 1.5 μm by increasing the WS_2 concentration to 7 wt% (denoted as "M7"). Tendentially, the size of spherulites is strongly dependent on the time of crystallization, whereas the WS_2 nanofillers act as nucleating agents reducing the activation energy for nucleus formation resulting in a facilitated crystallization and a higher number of globules with lower size [62]. Analogously, carbon nanotubes were previously found to be beneficial in engineering the microstructure of PVDF nanocomposite with an ultimate improvement of the crystallization conditions [63].

The cross sections revealed the presence of laminar structures proportional to the concentration of flakes, particularly evident in the membrane prepared with 7 wt% of WS_2 (M7), due to an entanglement of the polymeric chains strongly interacting with the filler (Fig. 5.4 c), in analogy with previous results for poly(vinylidene fluoride cohexafluoropropylene) (PVDF–HFP) electrospun nanofibers loaded with WS_2 nanotubes [64].

The optimal immobilization of the filler into the polymeric matrices was confirmed by the elemental mapping of the membranes, whereas analytical analysis of the coagulation and washing baths (Atomic Absorption and UV–Vis spectroscopy) revealing the absence of signal raising from released WS_2. Nevertheless, the embodiment of WS_2 into PVDF did not affect the structural properties of the membranes. As a matter of fact, in all cases the membranes presented a porosity in the range of 68.2–70.8 % with a mean pore of 0.15–0.16 μm and a contact angle of 103–108◦ for the surface in contact with the air during the NIPS process (airside) and 109–110◦ for the opposite surface (glass surface).

Tendentially, PVDF membranes prepared by conventional NIPS protocol are characterized by smooth surfaces with a contact angle of ca. 90◦ [65], whereas the occurrence of crystallization in delayed demixing favoured the formation of micro-scale spherulites responsible for high roughness [66], resulting in an improvement to the contact angle [67]. Therefore, the hierarchical spherulitic-based morphology of the membrane surface is suitable for improving the hydrophobicity of PVDF, making the membrane ideal for treating hypersaline aqueous solutions estimated following by avoiding pore wetting. Moreover, the porosity and the interconnected pores of the fabricated PVDF-WS_2 nanocomposite allowed the vapor generated at the membrane-water interface to permeate through the membranes, ultimately improving the evaporation rate, also considering another contribution from the stream generated at the air-water interface.

In our case, $\frac{\Delta G^*_{het}}{\Delta G^*_{hom}}$ estimated from Eq. (4), was 0.4 ± 0.3, revealing the role of the membrane in reducing the free energy of nucleation barrier thanks to the heterogeneous [57]. Thus, the energy required for the nucleation of salts is expected to be decreased by the membranes, enabling the heterogeneous nucleation of crystals at a lower supersaturation level with respect to homogeneous conditions (without the membranes), resulting in a facilitated crystallization of LiCl [58].

By increasing the loading of WS_2 nanofillers, the colour of nanocomposite membranes progressively turned from white to black (inset of Fig. 5.4 f). Correspondingly, the WS_2-derived enhancement of absorption in the visible region of the electromagnetic spectrum is evident in UV–Vis spectra (Fig. 5.4 f). In agreement with the effective model, UV–Vis spectra display multiple resonance peaks associated with exciton transition energies of WS2 discussed above.

5.3.4 Photothermal membrane crystallization

To implement PhMCr, the WS_2-PVDF nanocomposites were irradiated with natural solar radiation in order to estimate the photothermal efficiency. Thermal imaging in the infrared indicates that sunlight irradiation of WS_2-loaded membranes (M3.5, M5, and M7) induced a clear temperature increase, due to photothermal conversion of the absorbed radiation into heat (Fig. 5.5 a), whereas irradiated virgin PVDF (M0) did not display a significant deviation from room temperature. The evolution of the temperature of the membranes as a function of the irradiation time disclosed a sharp improvement whenever WS_2 nanofillers were embodied into PVDF membranes, achieving the steady state in 10 min (Fig. 5.5 b). The maximum heating rate observed was 1.44 $K \cdot min^{-1}$ at the highest nanofiller loading (M7), corresponding to a maximum temperature increase of ca. 15 ◦C.

Similarly to metal nanoparticles, WS_2 nanofillers acted as in-situ nano-heaters, owing to efficient absorption of the solar radiation and a homogeneous spatial distribution of heat arising from absorbed energy, with an ultimate increase of the temperature of the nanocomposite membrane (M3.5, M5, and M7). Generally, the enhancement of light heat conversion arises from an efficient light confinement, due to the excitation of localized surface plasmons on metal nanoparticles. Instead, here the enhanced absorption is driven by the high refractive index of WS_2 nanosheets, allowing a confinement factor comparable to that of the localized surface plasmons. It is worth noting that the multilayer WS_2 nanofillers used here have an intrinsically superior photothermal efficacy with respect to WS_2 monolayers, since the absorption cross section increases for higher

thickness. Explicitly, we incorporated WS_2 nanofillers, with an average thickness of about 37 nm (see Fig. 5.1 c), which results to be smaller than the effective wavelength of a WS_2 nanosheet $\lambda_{WS2} = \lambda/n_{WS2}$, where $n_{WS2}$is the WS_2 refractive index (e.g., λ_{WS2}= 105 nm at λ = 500 nm). Thus, the adopted thickness of WS_2 nanofillers assures that the electric field is constant inside the nanosheet, resulting in an efficient light-heat conversion.

Photothermal effects promoted by sunlight-activated nano-heaters have direct implications on the efficiency of water vaporization. The rate of water vaporization increases with temperature due to the exponential rise in vapor pressure with temperature, as described by the Clausius–Clapeyron relation. At a temperature of 28 ◦C, the evaporation rates ranged from 0.46 $kg \cdot m^{-2} \cdot h^{-1}$ for pristine PVDF (M0) up to 0.94 $kg \cdot m^{-2} \cdot h^{-1}$ (+94 %) in the case of the membrane loaded with the 7 wt% of WS_2 (M7) (Fig. 5.5 c). It is worth noticing the irrelevant impact of pristine PVDF (M0) on the evaporation rate, comparable to the one observed from water in the absence of membrane (denoted as “control” in Fig. 5.5 c).

Even if the temperature of PhMCr did not directly depend on the environmental temperature, the vaporization rate increased with the temperature, because of the higher heat of vaporization required at a lower temperature. In fact, the temperature of the environment and water significantly alter both latent heat (λ_v) and sensible heat (Q), affecting the vaporization efficiency (η_v).

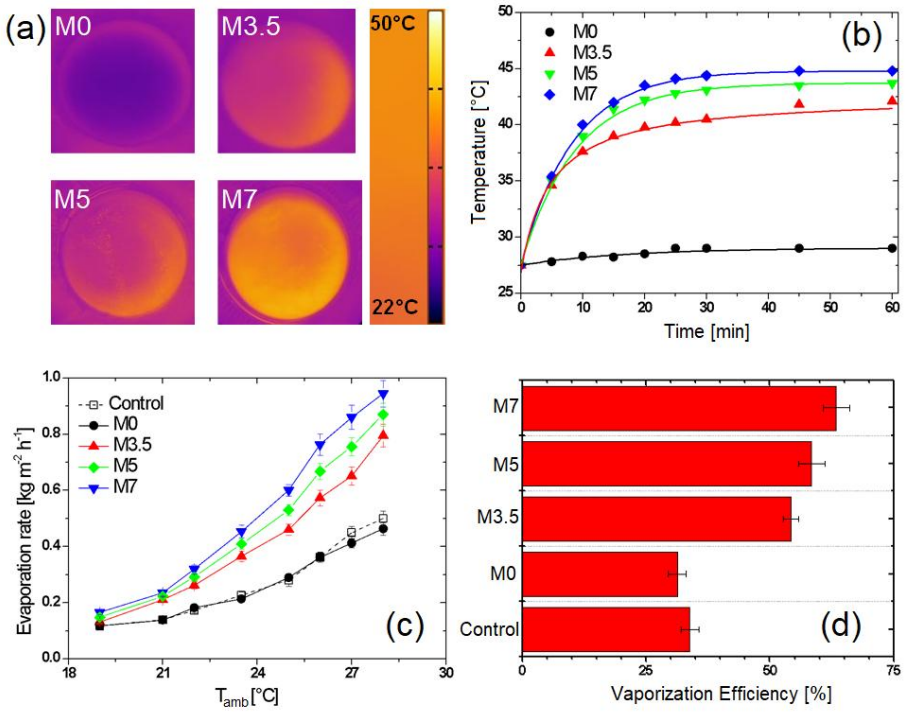


Figure 5.5. *(a) Infrared thermography acquired with a thermal camera for M0, M3.5, M5, and M7 membranes irradiated for 60 min with sunlight and (b) measured temperature of the same membranes as a function of irradiation time. (c) Evaporation rate of distilled water from PhMCr under solar radiation at different ambient temperatures. (d) Vaporization efficiency of distilled water under solar radiation (T = 28 ◦C).*

At 28 ◦C under solar irradiation, the vaporization efficiency η_v for distilled water increased from 31.1 % for virgin PVDF (M0) up to 63.4 % for PVDF loaded with the highest concentration of WS_2 nanofiller (M7), with a two-fold net improvement.

Once validated the efficiency of the photothermal effects, we irradiated PVDF-WS_2 nanocomposites with sunlight to promote Li recovery from the hypersaline LiCl solution, in order to assess the suitability of solar PhMCr. Interestingly, experiments performed using LiCl brine 18 M revealed a negative value of the evaporation rate for a temperature than 26 ◦C, due to the highly hydrophilic nature of LiCl, naturally absorbing the atmospheric humidity (Fig. 5.6 a). Note that this issue makes its extraction from salars rather challenging. In fact, LiCl was widely explored as a desiccant at room temperature, because of its outstanding water vapor absorption capacity of about 10 g H_2O per gram of [68, 69] and its low temperature of regeneration (40 °C) [70]. Moreover, the water vapor pressure is proportional to the water activity (a_w) and significantly affected by the concentration of the solutes [71]. Roughly, a_w dropped from 1 for the distilled water to 0.17 for Li solution (18 M). Likewise, the performance of the PhMCr was considerably influenced by the high concentration of LiCl. Explicitly, the evaporation rate exploiting the light-to-heat conversion of M7 (T = 28 ◦C) decreased from 0.945 $kg \cdot m^{-2} \cdot h^{-1}$ for pure water to 0.067 $kg \cdot m^{-2} \cdot h^{-1}$ for the brine (18 M LiCl). Therefore, the combination of the hydrophilic nature of LiCl and its high solubility in water provoked a decrease in the water evaporation rate by 94.1 ± 1.5 % for the three PhMCrs, close to the value reduction of the evaporation rate of 96.3 % observed for the control (T = 28 ◦C).

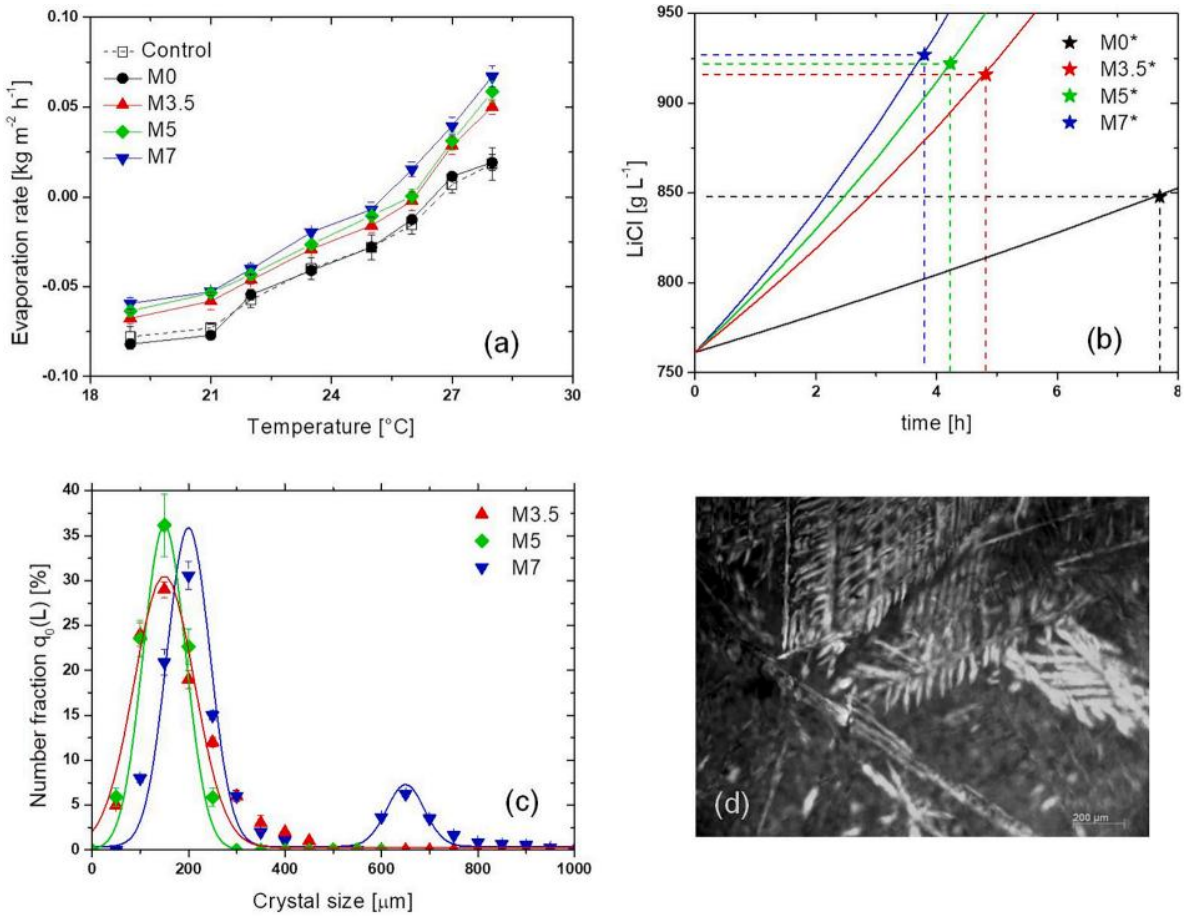


Figure 5.6. *(a) Evaporation rate from LiCl brine (18 M) in PhMCr under the solar radiation at different temperatures; (b) Evolution of LiCl concentration in PhMCr experiments (T = 28 ◦C) and theoretical supersaturation point (stars); (c) LiCl crystal size distribution; (d) Microscopic image of LiCl crystal achieved on the M7 surface after the experiments of PhMCr.*

Obviously, the evaporation rate is the key parameter for an efficient gradual concentration of the LiCl in the brine and the consequent crystallization of the solutes in a supersaturated environment. LiCl crystals were firstly observed in the PhMCr equipped with M7, followed by the one based on M5 and, lastly, M3.5; whereas the poor evaporation rates from the control and M0 were inadequate to induce the LiCl crystallization in 300 min (T = 28 ◦C). Moreover, the precipitation of the hydrophilic LiCl over the membrane surface provoked a drastic reduction of the evaporation rate. The modelling of the temporal evolution of the LiCl based on the evaporation rates of the different PhMCrs elucidated the advantages of the employment of membrane with higher photothermal efficiency (Fig. 5.6 b). Despite the efficient light-to-heat conversion acted by M7 raised the temperature of the brine to 44.8 ◦C with a subsequent superior solubility of LiCl (ca. 928 $g \cdot L^{-1}$) [72, 73],the achievement of the supersaturation was predicted in 228 min. In the case of the M3.5 membrane, the supersaturation was expected after about 289 min at a LiCl concentration of around

917 $g \cdot L^{-1}$, whereas the overcoming of the solubility limit for the PhMCr for bare PVDF (M0) was forecast after 462 min (>2-fold with respect to M7).

The observation of the surface of the PhMCr under the optical microscope (Fig. 5.6 d) confirmed the advantages arising from the inclusion of WS_2 nanofillers in PVDF membrane on the crystallization of LiCl. Unquestionably, the inspection of the surface of M0 revealed the absence of crystals, while their population and size increased with the concentration of the photothermal WS_2 nanofillers embodied in the membrane. Crystals presented an orthorhombic structure, which is the morphology of LiCl monohydrate [74]. In particular, crystals grown on M3.5 exhibited a needle-like morphology of aspect ratio 10:1 (Fig. 5.6 c) with a Gaussian distribution of its characteristic length with an average value of (150 ± 60) μm (Fig. 5.6 c). On the other hand, LiCl crystals growth on M7 showed a bimodal distribution (Fig. 5.6 c) with a major Gaussian peak centered at 200 μm and another maximum at 650 μm representing ca. the 17 % of LiCl crystals. Moreover, the population density of LiCl crystals on M7 was 4-fold higher with respect to M3.5 (~2000 crystals·cm^{-2} on M3.5 versus ~8000 crystals·cm^{-2} on M7).

The ultimate results of the accelerated evaporation rate on M7 induced by an efficient light-to-heat acted by WS_2 are a facilitated crystallization of LiCl in terms of quantity of crystals and size. Therefore, the percentage of recovered LiCl acted by PhMCr equipped with M7 resulted to be 8.4 %, much higher than the value of 0.2 % observed in the case of M3.5. These achievements are related to the mechanism of crystallization taking place in two simultaneous and competitive steps: nucleation and growth. Especially, M7 guaranteed a higher evaporation rate (0.067 $kg \cdot m^{-2} \cdot h^{-1}$) enabling a faster achievement of the supersaturation (228 min), resulting into expedited nucleation. This led to the formation of a higher number of nuclei with a lower critical size with respect to the case of M3.5, where supersaturation conditions are generated ca. 1 h later, as depicted in Fig. 5.6 b. However, the shorter nucleation time in PhMCr equipped with M7 offered to the nascent LiCl a larger resilience time in a supersaturated environment where the formed nuclei might grow and the presence of dislocations might drive the structural transformation and long-range order formation [75].

5.4 Conclusions

The clean energy transition involves efforts for innovation, investment, and deployment strategies for emerging energy storage technologies, such as Li-ion batteries. Therefore, lithium is a crucial

element for the ecological transition and the path to net-zero emissions. However, Li mining from ores has been considered prohibitive and it is usually extracted from brine via a time-consuming process based on the evaporation of the water under the effect of solar radiation and wind.

In this chapter, we devised a novel nanotechnology-enabled strategy to intensify the Li extraction from brine by boosting the evaporation rates of water, exploiting PhMCr based on light-to-heat conversion in WS_2 nanosheets. The use of the NIPS protocol in the fabrication of nanocomposite membranes enabled the homogenous dispersion of nanofillers from high-concentration WS_2-based functional inks obtained by fluid-dynamics-assisted LPE into microporous hydrophobic nanocomposite membranes able to convert sunlight into heat. Explicitly owing to the excitons-based photothermal effects in WS_2-loaded membranes, the water evaporation rate improved up to 94 % for the highest loading of WS_2 nanofillers (M7) compared to the unloaded membranes (M0). Definitely, solar-driven PhMCr activated a fast crystallization by accelerating the vaporization of the water, obtaining the crystallization of LiCl in 228 min (for M7 WS_2-loaded membranes) with a recovery of 8.4 %, whereas even prolonged tests were insufficient to reach the supersaturation in the unloaded membrane (M0).

Overall, this innovative and sustainable nanotechnology-enabled platform based on photothermal effects originating from excitons in nanosheets of van der Waals semiconductors demonstrates the possibility to combine renewable energy sources (such as sunlight) with membrane technologies to intensify the extraction of Li from salars, with the possibility to extend the use of PhMCr also for the recovery of other minerals. Notably, the implementation of PhMCr further expands the breadth of the application fields of van der Waals semiconductors and their nanocomposites to include (i) the crystallization and (ii) the recovery of economically strategic minerals at reduced operating costs, in excellent matching with the principles of circular blue economy. The future advent of the PhMCr technology, here validated for the case-study example of lithium (with obvious implications for batteries), could potentially enable the efficient and sustainable recovery at industrial scale of critical raw materials to address the global challenges of ecological transition, decarbonization, and clean energy.

References

[1]J.Guo, D. Dong, J. Wang, D. Liu, X. Yu, Y. Zheng, Z. Wen, W. Lei, Y. Deng, J. Wang, G. Hong, H. Shao. Silicon-based lithium ion battery systems: state-of-the-art from half and full cell viewpoint, Adv. Funct. Mater., 31 (2021), Article 2102546, 10.1002/adfm.202102546

[2] S. Chen, R. Tao, J. Tu, P. Guo, G. Yang, W. Wang, J. Liang, S.-Y. Lu. High performance flexible lithium-ion

battery electrodes: ion exchange assisted fabrication of carbon coated nickel oxide nanosheet arrays on carbon cloth, Adv. Funct. Mater., 31 (2021), Article 2101199, 10.1002/adfm.202101199

[3] X. Zeng, M. Li, D. Abd El-Hady, W. Alshitari, A.S. Al-Bogami, J. Lu, K. Amine. Commercialization of lithium battery technologies for electric vehicles, Adv. Energy Mater., 9 (2019), Article 1900161, 10.1002/aenm.201900161

[4] G. Zubi, R. Dufo-López, M. Carvalho, G. Pasaoglu. The lithium-ion battery: state of the art and future perspectives, Renew. Sust. Energ. Rev., 89 (2018), pp. 292-308, 10.1016/j.rser.2018.03.002

[5] P. Greim, A.A. Solomon, C. Breyer. Assessment of lithium criticality in the global energy transition and addressing policy gaps in transportation, Nat. Commun., 11 (2020), p. 4570, 10.1038/s41467-020-18402-y

[6] Report on Critical Raw Materials for the EU. Report of the Ad hoc Working Group on Defining Critical Raw Materials (2014)

[7] Critical Raw Materials Resilience: Charting a Path Towards Greater Security and Sustainability
(2020)

[8] N. Supanchaiyamat, A.J. Hunt. Conservation of critical elements of the periodic table, ChemSusChem., 12 (2019), pp. 397-403, 10.1002/cssc.201802556

[9] P. Meshram, B.D. Pandey, T.R. Mankhand. Extraction of lithium from primary and secondary sources by pre-treatment, leaching and separation: a comprehensive review, Hydrometallurgy, 150 (2014), pp. 192-208, 10.1016/j.hydromet.2014.10.012

[10] P.K. Choubey, M. Kim, R.R. Srivastava, J. Lee, J.-Y. Lee. Advance review on the exploitation of the prominent energy-storage element: lithium. Part I: from mineral and brine resources, Miner. Eng., 89 (2016), pp. 119-137, 10.1016/j.mineng.2016.01.010

[11] V.T. Luong, D.J. Kang, J.W. An, M.J. Kim, T. Tran. Factors affecting the extraction of lithium from lepidolite, Hydrometallurgy, 134–135 (2013), pp. 54-61, 10.1016/j.hydromet.2013.01.015

[12]S. Santoro, H. Estay, A.H. Avci, L. Pugliese, R. RubyFigueroa, A. Garcia, M. Aquino, S. Nasirov, S. Straface, E . Curcio. Membrane technology for a sustainable copper mining industry: the Chilean paradigm, Clean. Eng. Technol., 2 (2021), Article 100091, 10.1016/j.clet.2021.100091

[13] H. Vikström, S. Davidsson, M. Höök. Lithium availability and future production outlooks
Appl. Energy, 110 (2013), pp. 252-266, 10.1016/j.apenergy.2013.04.005

[14] J.W. An, D.J. Kang, K.T. Tran, M.J. Kim, T. Lim, T. Tran. Recovery of lithium from Uyuni salar brine, Hydrometallurgy, 117–118 (2012), pp. 64-70, 10.1016/j.hydromet.2012.02.008

[15] V. Flexer, C.F. Baspineiro, C.I. Galli. Lithium recovery from brines: a vital raw material for green energies with a potential environmental impact in its mining and processing, Sci. Total Environ., 639 (2018), pp. 1188-1204, 10.1016/j.scitotenv.2018.05.223

[16] Z. Li, J. Mercken, X. Li, S. Riaño, K. Binnemans. Efficient and sustainable removal of magnesium from brines for lithium/magnesium separation using binary extractants, ACS Sustain. Chem. Eng., 7 (2019), pp. 19225-19234, 10.1021/acssuschemeng.9b05436

[17] Y. Sun, Q. Wang, Y. Wang, R. Yun, X. Xiang. Recent advances in magnesium/lithium separation and lithium extraction technologies from salt lake brine, Sep. Purif. Technol., 256 (2021), Article 117807, 10.1016/j.seppur.2020.117807

[18] Y. Guo, F. Li, H. Zhu, G. Li, J. Huang, W. He. Leaching lithium from the anode electrode materials of spent lithium-ion batteries by hydrochloric acid (HCl), Waste Manag., 51 (2016), pp. 227-233, 10.1016/j.wasman.2015.11.036

[19] C. Chen, Y. Kuang, L. Hu. Challenges and opportunities for solar evaporation, Joule, 3 (2019), pp. 683-718, 10.1016/j.joule.2018.12.023

[20] G. Liu, Z. Zhao, A. Ghahreman. Novel approaches for lithium extraction from salt-lake brines: a review, Hydrometallurgy, 187 (2019), pp. 81-100, 10.1016/j.hydromet.2019.05.005

[21] E. Drioli, E. Curcio. Membrane engineering for process intensification: a perspective, J. Chem. Technol. Biotechnol., 82 (2007), pp. 223-227, 10.1002/jctb.1650

[22] E. Drioli, G. Di Profio, E. Curcio. Progress in membrane crystallization, Curr. Opin. Chem. Eng., 1 (2012), pp. 178-182, 10.1016/j.coche.2012.03.005

[23] E. Curcio, E. Fontananova, G. Di Profio, E. Drioli. Influence of the structural properties of Poly(vinylidene fluoride) membranes on the heterogeneous nucleation rate of protein crystals, J. Phys. Chem. B, 110 (2006), pp. 12438-12445, 10.1021/jp061531y

[24] G. Di Profio, S. Tucci, E. Curcio, E. Drioli. Controlling polymorphism with membrane-based crystallizers: application to form I and II of paracetamol, Chem. Mater., 19 (2007), pp. 2386-2388, 10.1021/cm0701005

[25] M.-C. Sparenberg, S. Chergaoui, V. Sang Sefidi, P. Luis. Crystallization control via membrane distillation-crystallization: a review, Desalination, 519 (2021), Article 115315, 10.1016/j.desal.2021.115315

[26] E. Drioli, A. Criscuoli, E. Curcio. Integrated membrane operations for seawater desalination, Desalination, 147 (2002), pp. 77-81, 10.1016/S0011-9164(02)00579-9

[27] X. Jiang, Y. Shao, L. Sheng, P. Li, G. He. Membrane crystallization for process intensification and control: a review, Engineering, 7 (2021), pp. 50-62, 10.1016/j.eng.2020.06.024

[28] C.A. Quist-Jensen, A. Ali, S. Mondal, F. Macedonio, E. Drioli. A study of membrane distillation and crystallization for lithium recovery from high-concentrated aqueous solutions, J. Membr. Sci., 505 (2016), pp. 167-173, 10.1016/j.memsci.2016.01.033

[29]S.H. Park, J.H. Kim, S.J. Moon, J.T. Jung, H.H. Wang, A. Ali, C.A. Quist-Jensen, F. Macedonio, E. Drioli, Y.M. Lee. Lithium recovery from artificial brine using energy-efficient membrane distillation and nanofiltration, J. Membr. Sci., 598 (2020), Article 117683, 10.1016/j.memsci.2019.117683

[30]A. Cerda, M. Quilaqueo, L. Barros, G. Seriche, M. Gim-Krumm, S. Santoro, A.H. Avci, J. Romero, E. Curcio, H. Estay. Recovering water from lithium-rich brines by a fractionation process based on membrane distillation-crystallization, J. Water Process Eng., 41 (2021), Article 102063, 10.1016/j.jwpe.2021.102063

[31] S. Santoro, M. Aquino, D. Han Seo, T. Van Der Laan, M. Lee, J. Sung Yun, M. Jun Park, A. Bendavid, H. Kyong Shon, A. Halil Avci, E. Curcio. Dimensionally controlled graphene-based surfaces for photothermal membrane crystallization, J. Colloid Interface Sci. (2022), 10.1016/j.jcis.2022.05.062

[32] S. Santoro, A.H. Avci, A. Politano, E. Curcio. The advent of thermoplasmonic membrane distillation, Chem. Soc. Rev., 51 (2022), pp. 6087-6125, 10.1039/D0CS00097C

[33] J. Sterba, A. Krzemień, P.R. Fernández, C.E. García-Miranda, G.F. Valverde. Lithium mining: Accelerating the transition to sustainable energy, Res. Pol., 62 (2019), p. 416, 10.1016/j.resourpol.2019.05.002

[34] Y. Zhang, Y. Hu, L. Wang, W. Sun. Systematic review of lithium extraction from salt-lake brines via precipitation approaches, Miner. Eng., 139 (2019), Article 105868, 10.1016/j.mineng.2019.105868

[35]A. Politano, P. Argurio, G. DiProfio, V. Sanna, A. Cupolillo, S. Chakraborty, H.A. Arafat, E. Curcio. Photothermal membrane distillation for seawater desalination, Adv. Mater., 29 (2017), Article 1603504, 10.1002/adma.201603504

[36] A. Politano, G. Di Profio, E. Fontananova, V. Sanna, A. Cupolillo, E. Curcio. Overcoming temperature polarization in membrane distillation by thermoplasmonic effects activated by ag nanofillers in polymeric membranes, Desalination, 451 (2019), pp. 192-199, 10.1016/j.desal.2018.03.006

[37]K.V. Sreekanth, R. Medwal, C.M. Das, M. Gupta, M. Mishra, K.T. Yong, R.S. Rawat, R. Singh. Electrically tunable all-PCM visible plasmonics, Nano Lett., 21 (2021), pp. 4044-4050, 10.1021/acs.nanolett.1c00941

[38] H. Gao, W. Peng, Y. Liang, S. Chu, L. Yu, Z. Liu, Y. Zhang. Plasmonic broadband perfect absorber for visible light solar cells application, Plasmonics, 15 (2020), pp. 573-580, 10.1007/s11468-019-01087-5

[39]P.G. Karagiannidis, S.A. Hodge, L. Lombardi, F. Tomarchio, N. Decorde, S. Milana, I. Goykhman, Y. Su, S.V. Mesite, D.N. Johnstone, R.K. Leary, P.A. Midgley, N.M. Pugno, F. Torrisi, A.C. Ferrari. Microfluidization of graphite and formulation of graphene-based conductive inks, ACS Nano, 11 (2017), pp. 2742-2755, 10.1021/ACSNANO.6B07735

[40] Y. Imai, D. Shimamoto, Y. Hotta. Effect of wet jet milling of carbon nanotube on electrical properties of polymer nanocomposites, Mater. Chem. Phys., 148 (2014), pp. 1178-1183, 10.1016/J.MATCHEMPHYS.2014.09.044

[41] S. Santoro, E. Drioli, A. Figoli. Development of novel ECTFE coated PP composite hollow-fiber membranes, Coatings, 6 (2016), 10.3390/coatings6030040

[42] E. Drioli, S. Santoro, S. Simone, G. Barbieri, A. Brunetti, F. Macedonio, A. Figoli. ECTFE membrane preparation for recovery of humidified gas streams using membrane condenser, React. Funct. Polym., 79 (2014), 10.1016/j.reactfunctpolym.2014.03.003

[43]S. Santoro, V. Sebastian, A.J. Moro, C.A.M. Portugal, J.C. Lima, I.M. Coelhoso, J.G. Crespo, R. Mallada. Development of fluorescent thermoresponsive nanoparticles for temperature monitoring on membrane surfaces, J. Colloid Interface Sci., 486 (2017), pp. 144-152, 10.1016/j.jcis.2016.09.059

[44] A. Gugliuzza, A. Politano, E. Drioli. The advent of graphene and other two-dimensional materials in membrane science and technology, Curr. Opin. Chem. Eng., 16 (2017), pp. 78-85, 10.1016/J.COCHE.2017.03.003

[45] F. Perrozzi, S.M. Emamjomeh, V. Paolucci, G. Taglieri, L. Ottaviano, C. Cantalini. Thermal stability of WS2 flakes and gas sensing properties of WS2/WO3 composite to H2, NH3 and NO2, Sensors Actuators B Chem., 243 (2017), pp. 812-822, 10.1016/J.SNB.2016.12.069

[46]V. Paolucci, G. D'Olimpio, L. Lozzi, A.M. Mio, L. Ottaviano, M. Nardone, G. Nicotra, P. Le-Cornec, C. Cantalini, A. Politano. Sustainable liquid-phase exfoliation of layered materials with nontoxic polarclean solvent, ACS Sustain. Chem. Eng., 8 (2020), pp. 18830-18840, 10.1021/acssuschemeng.0c04191

[47] K.C. Wong, X. Lu, J. Cotter, D.T. Eadie, P.C. Wong, K.A.R. Mitchell. Surface and friction characterization of MoS2 and WS2 third body thin films under simulated wheel/rail rolling-sliding contact, Wear, 264 (2008), pp. 526-534, 10.1016/j.wear.2007.04.004

[48] A. Ciattoni, C. Rizza. Nonlocal homogenization theory in metamaterials: effective electromagnetic spatial dispersion and artificial chirality, Phys. Rev. B - Condens. Matter Mater. Phys., 91 (2015), Article 184207, 10.1103/PHYSREVB.91.184207/FIGURES/4/MEDIUM

[49] O. Levy, D. Stroud. Maxwell Garnett theory for mixtures of anisotropic inclusions: application to conducting polymers, Phys. Rev. B, 56 (1997), p. 8035, 10.1103/PhysRevB.56.8035

[50] C.G. Duan, W.N. Mei, W.G. Yin, J. Liu, J.R. Hardy, M. Bai, S. Ducharme. Theoretical study on the optical properties of polyvinylidene fluoridecrystal, J. Phys. Condens. Matter., 15 (2003), p. 3805, 10.1088/0953-8984/15/22/314

[51] A.R. Beal, W.Y. Liang, H.P. Hughes. Kramers-kronig analysis of the reflectivity spectra of 3R-WS2 and 2H-

WSe2, J. Phys. C Solid State Phys., 9 (1976), p. 2449, 10.1088/0022-3719/9/12/027

[52]Y. Li, A. Chernikov, X. Zhang, A. Rigosi, H.M. Hill, A.M. VanDerZande, D.A. Chenet, E.M. Shih, J. Hone, T. F. Heinz. Measurement of the optical dielectric function of monolayer transition-metal dichalcogenides: MoS2, Mo S e2, WS2, and WS e2, Phys. Rev. B - Condens. Matter Mater. Phys., 90 (2014), Article 205422, 10.1103/PHYSREVB.90.205422/FIGURES/6/MEDIUM

[53]H.M. Hill, A.F. Rigosi, C. Roquelet, A. Chernikov, T.C. Berkelbach, D.R. Reichman, M.S. Hybertsen, L.E. Bru s, T.F. Heinz. Observation of excitonic rydberg states in monolayer MoS2 and WS2 by photoluminescence excitation spectroscopy, Nano Lett., 15 (2015), pp. 2992-2997, 10.1021/NL504868P/SUPPL_FILE/NL504868P_SI_001.PDF

[54] S. Sharma, S. Bhagat, J. Singh, R.C. Singh, S. Sharma. Excitation-dependent photoluminescence from WS2 nanostructures synthesized via top-down approach, J. Mater. Sci., 52 (2017), pp. 11326-11336, 10.1007/s10853-017-1303-3

[55] G.T. Papadakis, A. Davoyan, P. Yeh, H.A. Atwater. Mimicking surface polaritons for unpolarized light with high-permittivity materials, Phys. Rev. Mater., 3 (2019),
Article 015202, 10.1103/PHYSREVMATERIALS.3.015202/FIGURES/7/MEDIUM

[56] G.P. Zograf, M.I. Petrov, S.V. Makarov, Y.S. Kivshar. All-dielectric thermonanophotonics
Adv. Opt. Photon., 13 (2021), p. 643, 10.1364/AOP.426047

[57] G. Di Profio, E. Curcio, E. Drioli. Supersaturation control and heterogeneous nucleation in membrane crystallizers: facts and perspectives, Ind. Eng. Chem. Res., 49 (2010), pp. 11878-11889, 10.1021/ie100418z

[58]E. Curcio, V. LópezMejías, G. DiProfio, E. Fontananova, E. Drioli, B.L. Trout, A.S.
Myerson. Regulating nucleation kinetics through molecular interactions at the polymer-solute interface, Cryst. Growth Des., 14 (2014), pp. 678-686, 10.1021/cg4015543

[59]C. Ursino, S. Simone, L. Donato, S. Santoro, M.P. DeSanto, E. Drioli, E. Di Nicolò, A. Figoli. ECTFE membranes produced by non-toxic diluents for organic solvent filtration separation, RSC Adv., 6 (2016), 10.1039/c6ra13343f

[60]M. Drobek, A. Figoli, S. Santoro, N. Navascués, J. Motuzas, S. Simone, C. Algieri, N. Gaeta, L. Querze, A. Trot ta, G. Barbieri, R. Mallada, A. Julbe, E. Drioli. PVDF-MFI mixed matrix membranes as VOCs adsorbers, Microporous Mesoporous Mater., 207 (2015), pp. 126-133, 10.1016/j.micromeso.2015.01.005

[61] P. Sukitpaneenit, T.-S. Chung. Molecular elucidation of morphology and mechanical properties of PVDF hollow fiber membranes from aspects of phase inversion, crystallization and rheology, J. Membr. Sci., 340 (2009), pp. 192-205, 10.1016/j.memsci.2009.05.029

[62] K.-J. Lu, J. Zuo, T.-S. Chung. Novel PVDF membranes comprising n-butylamine functionalized graphene oxide for direct contact membrane distillation, J. Membr. Sci., 539 (2017), pp. 34-42, 10.1016/j.memsci.2017.05.064

[63] G. Mago, D.M. Kalyon, F.T. Fisher. Membranes of polyvinylidene fluoride and PVDF nanocomposites with carbon nanotubes via immersion precipitation, J. Nanomater., 2008 (2008), Article 759825, 10.1155/2008/759825

[64] O. Grinberg, S. Deng, E. Zussman, T. Livneh, A. Zak. Raman scattering from single WS2 nanotubes in stretched PVDF electrospun fibers, Phys. Chem. Chem. Phys., 19 (2017), pp. 18443-18451, 10.1039/C7CP00934H

[65] F. Russo, C. Ursino, E. Avruscio, G. Desiderio, A. Perrone, S. Santoro, F. Galiano, A. Figoli
Innovative poly (vinylidene fluoride) (PVDF) electrospun nanofiber membrane preparation using DMSO as a low toxicity solvent, Membranes (Basel), 10 (2020), p. 36, 10.3390/membranes10030036

[66] F.A. AlMarzooqi, M.R. Bilad, H.A. Arafat. Development of PVDF membranes for membrane distillation via vapour induced crystallization, Eur. Polym. J., 77 (2016), pp. 164-173, 10.1016/j.eurpolymj.2016.01.031

[67] R.N. Wenzel. Resistance of solid surfaces to wetting by water, Ind. Eng. Chem., 28 (1936), pp. 988-994, 10.1021/ie50320a024

[68] Y. Yang, D. Rana, C.Q. Lan. Development of solid super desiccants based on a polymeric superabsorbent hydrogel composite, RSC Adv., 5 (2015), pp. 59583-59590, 10.1039/C5RA04346H

[69] S.K. Chaudhari, K.R. Patil. Thermodynamic properties of aqueous solutions of lithium chloride, Phys. Chem. Liq., 40 (2002), pp. 317-325, 10.1080/0031910021000004883

[70] G.A. Longo, A. Gasparella. Experimental and theoretical analysis of heat and mass transfer in a packed column dehumidifier/regenerator with liquid desiccant, Int. J. Heat Mass Transf., 48 (2005), pp. 5240-5254, 10.1016/j.ijheatmasstransfer.2005.07.011

[71] K.W. Lawson, D.R. Lloyd. Membrane distillation, J. Membr. Sci., 124 (1997), pp. 1-25, 10.1016/S0376-7388(96)00236-0

[72] J.A.N. Friend, A.T.W. Colley. CCCCXXXIV.—The solubility of lithium chloride in water, J. Chem. Soc. (1931), pp. 3148-3149, 10.1039/JR9310003148

[73] M. Arabi, M.R. Dehghani. Measurement of solubility and density of water + lithium bromide + lithium chloride and water + lithium bromide + sodium formate systems, Int. J. Refrig., 56 (2015), pp. 99-104, 10.1016/j.ijrefrig.2015.04.002

[74] A. Hönnerscheid, J. Nuss, C. Mühle, M. Jansen. Die Kristallstrukturen der Monohydrate von Lithiumchlorid und Lithiumbromid, Z. Anorg. Und Allg. Chem., 629 (2003), pp. 312-316, 10.1002/zaac.200390049

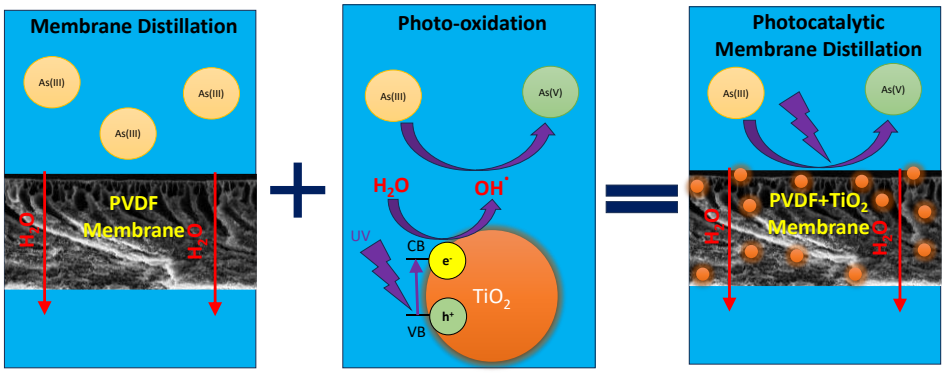
[75] B. der Bruggen. Nucleation stage crystal growth, E. Drioli, L. Giorno (Eds.), Encycl. Membr, SpringerBerlin Heidelberg, Berlin, Heidelberg (2015), pp. 1-2, 10.1007/978-3-642-40872-4_417-1

Chapter 6

Green photocatalytic mixed matrix membranes for simultaneous arsenic photo-oxidation and water recovery via membrane distillation

Keywords: Arsenic; Green Solvent; Membrane Distillation; Photocatalytic Membranes; Photo-oxidation

GRAPHICAL ABSTRACT



Contents

Abstract

6.1. Introduction

6.2. Materials and methods

6.2.1 Materials

6.2.2 Analytical methods

6.2.3 Membrane preparation

6.2.4 Membrane characterization

6.2.5 Photocatalytic membrane distillation reactor

6.3. Results

6.3.1 Membrane characterization

6.3.2 VMD performance

6.3.3 Photocatalytic membranes for As (III) oxidation in As(V)

6.3.4 PC-VMD for as remediation

6.4. Conclusions

References

This chapter has been published as:

Santoro S., Occhiuzzi J., Aquino M., Politano A., Straface S., D'Andrea G., Carillo C., Mallada R., Garcia A., Estay H., Xevgenos D., Argurio P.,Curcio E., Green photocatalytic mixed matrix membranes for simultaneous arsenic photo-oxidation

and water recovery via membrane distillation, Separation and Purification Technology 2024, 342, 127042; https://doi.org/10.1016/j.seppur.2024.127042

Abstract

This section of my PhD work proposes an innovative integration of Membrane Distillation (MD) and photo-oxidation for a continuous recovery of water from arsenic (As) contaminated solutions coupled with the oxidation of arsenite (As (III)) into arsenate (As(V)). Polyvinylidene fluoride (PVDF) mixed matrix membranes (MMMs) containing titanium dioxide nanoparticles (TiO_2 NPs) as photocatalyst were developed. A systematic study elucidated the effect of TiO_2 NPs on membranes' morphology prepared via non-solvent-induced phase separation (NIPS) using triethyl phosphate (TEP) as a green solvent for PVDF solubilization. Vacuum membrane distillation (VMD) tests carried out by irradiating the MMMs with ultraviolet (UV) radiation demonstrated the possibility of recovering up to 80 % of the water from As-contaminated synthetic and real multi-ions aqueous solutions from Sila Massif (Italy). The distillate was recovered at a rate of 6.9–7.2 $kg \cdot m^{-2} \cdot h^{-1}$ (feed inlet temperature of 60 °C), while the presence of 7 wt% of TiO_2 in PVDF membranes enabled the photo-oxidation of 95 % of the As(III) to As(V) at a first order kinetic constant of 0.0106 min^{-1}. After 5 cycles of As-remediation experiments, post-hoc mechanical testing on the membrane suggested the emergence of polymer embrittlement induced by UV radiation (total irradiation time of 7.5 h), highlighting the urgent need for developing photocatalytic membranes with long-term stability. Overall, this study elucidates at laboratory scale the performance of a coupled and continuous Membrane Distillation (MD) and photo-oxidation system for arsenic (As) remediation, employing microporous hydrophobic green membranes doped with a photocatalyst.

6.1 Introduction

Arsenic (As) is a toxic and carcinogenic metalloid [1] and the World Health Organization (WHO) fixed at 10 $\mu g \cdot L^{-1}$ its threshold concentration in drinking-water [2]. The presence of As in the earth's crust [3, 4] and its high mobility in aquifers [5] have been for centuries the major causes of As contamination of waterbodies, recently exacerbated by anthropic activities [6, 7, 8]. Currently, the global pattern has revealed an alarming presence of As in freshwater in at least seven countries, and more than 100 million people are daily exposed to As-contaminated water [9].

A wide variety of technologies have been explored for As remediation to attain the stringent threshold fixed by the WHO, including coagulation–flocculation, adsorption, ion exchange, and oxidation [10]. The abovementioned strategies are characterized by numerous critical issues such as expensive, time-demanding, and elaborate pre-treatment steps, chemical regeneration stages for

adsorbent materials or ion exchange reactions, and the formation of byproducts such as hazardous sludge in coagulation and flocculation processes [10, 11, 12].

Moreover, these techniques effectively remove arsenate (H_3AsO_4, As(V)) being dissociated in mild conditions; while they fail in the remediation of arsenite (H_3AsO_3, As (III)), characterized by higher toxicity and mobility, because uncharged for pH below than 9.2 [13]. In fact, zero-valent iron is the most studied As-absorbent material showing an absorption capacity of 36.9 $mg \cdot g^{-1}$ for As(V) reduced to 14.3 $mg \cdot g^{-1}$ for As(III) [14]. Also popular coagulation-agents such as ferric chloride and chitosan decrease their efficiency in the removal of As(III) in comparison to As(V) from 90 % to 60 % and from 100 % to 80 % respectively [15].

Definitively, the oxidation of As(III) into As(V) is a crucial step before downstream processing. Accordingly, titanium dioxide (TiO_2) has been extensively recognized as an effective photocatalyst for the oxidation of As(III) to As(V) because of the strong oxidation potential of the photogenerated valence band (VB) holes generated upon the absorption of ultraviolet (UV) radiation [13, 16].

In recent years, membrane processes have gained increasing success because of their efficiency, inherent modularity, operational simplicity, small footprint, reliability, and environmental friendliness [17, 18, 19]v. Therefore, membrane technologies are suitable for different approaches aimed at energy-saving and efficient water treatments [20, 21, 22], including metal remediation [23, 24]. On the basis of the size exclusion mechanism, pressure-driven membrane processes, especially Reverse Osmosis (pore size < 0.5 nm) and Nanofiltration (0.5 nm < pore size < 2 nm), present the tremendous advantage to ensure high As rejection rates independently form the oxidation state [25]. Likewise, the membrane distillation (MD) provides the opportunity to produce high-quality freshwater under a moderate temperature gradient by microporous hydrophobic membranes, enabling the diffusional transport of volatile compounds in the vapor phase into the pores and the theoretical 100 % rejection of non-volatile components [26, 27]. In contrast to pressure-driven operations, MD is not limited by osmotic pressure and concentration polarization, thus achieving a high water recovery factor from aqueous solutions (such as up to 90 % from seawater) [28, 29]. Other strengths of MD, useful in the remediation of As-contaminated waterbodies, are the negligible impact of feed composition (including the As concentration), presence of other solutes, and pH on the performance of the process [30, 31, 32]. Accordingly, different studies have demonstrated the potential of MD operations in the remediation of As-contaminated aqueous solutions, showing rejection rates in the range of 95–100 % [33]. Moreover, recent works have highlighted the prospects of hybridization with renewable energies or waste heat [30] or the exploitation of photothermal nanomaterials [34, 35] to sustainably harvest the heat required to vaporize water. In addition, the protraction of MD operation up to a high recovery factor

enables the generation of minimal volumes of highly concentrated retentate suitable for a post-treatment process [36].

In previous work from my same group, we demonstrated the effectiveness of MD in recovering up to 98.8 % of high-quality distilled water from As-contaminated solution, while the 83-fold concentrated retentate was subjected to a batch treatment of photocatalysis to convert As(III) to As(V) easily removed by polymer-enhanced ultrafiltration (PEUF) [37].

In the present study, the photocatalyst was directly embodied into hydrophobic microporous membranes prepared according to green routes with the aim to couple for the first time photocatalytic arsenic oxidation technology and membrane distillation together implementing the pioneering concept of photocatalytic MD (PC-MD) for a simultaneous arsenic photo-oxidation and water recovery in the logic of process intensification.

The photocatalytic mixed matrix membranes (MMMs) were prepared via non-solvent-induced phase separation (NIPS) upon the solubilization of polyvinylidene fluoride (PVDF) in a dispersion of TiO_2 in triethyl phosphate (TEP), a green solvent. We systematically elucidated the effects of (i) the influence of the embodiment of the TiO_2 on the physicochemical properties of the photocatalytic membranes, (ii) the feed temperature on the MD performance, and (iii) the TiO_2 loading on the photo-oxidation rate of As(III) to As(V), subsequently removed by an aluminosilicate adsorbent. To assess the feasibility of the process in treating real groundwater, experiments were also conducted using a multi-ion solution contaminated by As(III).

Overall, this work opens new perspectives in implementing an integrated approach that can synergistically combine MD and photocatalytic membrane technologies for continuous As remediation of waterbodies.

6.2 Materials and methods

6.2.1 Materials

Polyvinylidene fluoride Grade Solef® 6010 (PVDF, M_w = 322 kg·mol^{-1}) was supplied by Solvay Specialty Polymers (Italy). Triethyl phosphate (TEP) from Sigma-Aldrich (Italy) was used as the solvent without further purification. Polyvinylpyrrolidone (PVP K17, BASF, Ludwigshafen, Germany, Mw = 9 kg·mol^{-1}) and polyethylene glycol (PEG, Sigma Aldrich, Milan, Italy, Mw = 200 g·mol^{-1}) were selected as pore-former agents. TiO_2 nanoparticles (NPs) type P25 purchased from Evonic-Degussa (Germany) with a size of 20 nm, a specific surface area of 44 $m^2 \cdot g^{-1}$, a band gap of 3.2 eV and containing anatase and rutile phases in a ratio of 4:1 was used as photocatalyst [38].

Sodium metaarsenite $NaAsO_2$ (Mw = 129.91 g·mol^{-1}, purity of ≥ 98 %) and sodium arsenate dibasic hepta-hydrate $Na_2HAsO_4 \cdot 7H_2O$ (M_w = 312.01 g·mol^{-1}, purity of ≥ 98 %), both purchased from Sigma-Aldrich (Italy), were used as As(III) and As(V) based salts and solubilized in ultrapure Milli-Q water for the preparation of artificial As-contaminated solution. As(III) (0.06 mg·L^{-1}) was solubilized into a real water sample from Calabria (Italy) to mimic the As contamination recently observed in the groundwater of Sila Massif (Calabria, Italy) [39].

6.2.2 Analytical methods

The As concentration was determined by high-resolution continuum source atomic absorption spectrometry (HR-CS AAS). As(III) and As(V) concentrations were quantified by analytical kits MQuant (Merck, Italy) operating in the ranges 0.005–0.5 mg·L^{-1} and 0.02–3.0 mg·L^{-1} obtaining comparable values with respect to HR-CS AAS measurements (difference < 4 %). Cartridges containing 0.8 g of aluminosilicate purchased from Metalsoft Center (USA) were employed as speciation media able to selectively adsorb As(V) [40].

The ionic composition of real water samples was determined by ion chromatography (Metrohm 861 Advanced Compact IC, Switzerland) using 3.2 mM Na_2CO_3 + 1 mM $NaHCO_3$ solution as the eluent for the anion column Metrosep A Supp 5–250/4.0 and 2 mM nitric acid + 0.25 mM oxalic acid solution for the cation column Metrosep C4–250/4.0.

6.2.3 Membrane preparation

The polymeric solution was prepared by dissolving 15 wt% of PVDF in TEP at a temperature of 100 ◦C under magnetic stirring (100 rpm for 8 h); moreover, 5 wt% of PVP and 20 % of PEG were added to the polymeric solution as pore-forming agents.

For the preparation of the photocatalytic MMMs, TiO_2 NPs were previously dispersed in TEP via sonication (Sonica2200ETH, Soltec, Italy) for 30 min. The PVDF powder and the additives were then solubilized in the colloidal solution by magnetic stirring (100 rpm for 8 h). The concentration of TiO_2 catalyst was 0 wt% (M0), 2.5 wt% (M2.5), 5 wt% (M5), and 7 wt% (M7) with respect to PVDF. Table 1 summarizes the polymeric solutions used for membrane preparation.

Before the casting procedure, the solutions were degassed at room temperature (25 ◦C) for 2 h. The PVDF solutions were cast onto a glass plate using a casting knife (Automatic Film Applicator 4340 by Elcometer, UK) set at 300 µm of thickness. The nascent membranes were subsequently immersed in a coagulation bath of water for 2 h.

The obtained flat membranes were washed with distilled water at 50 ◦C for 2 h and subsequently with ethanol (2 h) to remove eventual traces of TEP, PVP or PEG. Finally, the membranes were dried overnight at room temperature and 60 ◦C for 2 h before characterization.

Table 1. *PVDF membranes prepared via NIPS by varying the concentration of TiO_2 in the polymeric solutions.*

Membrane	PVDF (wt.%)	TiO_2 (wt.%)	PVP (wt.%)	PEG (wt.%)	TEP (wt.%)
M0	15	0	5	20	60
M2.5	15	1.05	5	20	58.95
M5	15	0.75	5	20	59,25
M7	15	0,375	5	20	59,625

6.2.4 Membrane characterization

Membrane porosity (ε) was determined according to the gravimetric method consisting of measuring the mass of the membranes in dry and wet circumstances after immersion for 24 h in kerosene and applying the following formula [41]:

$$\varepsilon(\%) = \left\{ \frac{(W_w - W_d)/\rho_i}{(W_w - W_d)/\rho_i + \frac{W_d}{\rho_m}} \right\} \cdot 100 \qquad (1)$$

where W_w is the weight of the wet membrane, W_d is the weight of the dry membrane, ρi is the kerosene density (0.82 $g \cdot cm^{-3}$) and ρm is the density of the membrane material estimated from the PVDF (1.78 $g \cdot cm^{-3}$) and TiO_2 (4.23 $g \cdot cm^{-3}$) densities. Three measurements for each membrane were performed to calculate the average values and standard deviations.

The mean pore size (d_{mean}) and the largest pore size (d_{max}) were assessed using a PMI Capillary Flow Porometer (Model CFP-1500AEXL, Porous Materials Inc., USA) operating via Capwin software (Porous Materials Inc., USA) according to the wet up/dry-up method and using Porewick® (surface tension 16 $dyn \cdot cm^{-1}$) as the wetting liquid. The experimental data were computed using

Caprep software (Porous Materials Inc., USA) to obtain the values of the mean pore diameter (d_{mean}) and the largest pore diameter (d_{max}).

The morphology of the membranes was revealed by a scanning electron microscope (SEM) QUANTA INSPECT F50 (FEI Company, The Netherlands).

Membrane hydrophobicity was estimated by water contact angle (WCA) measurements (Model CAM 200, KSV Instruments, Finland) according to the sessile drop method at ambient temperature.

The Ultraviolet–Visible (UV–Vis) absorption of the photocatalytic membranes was measured using a spectrophotometer (Shimadzu UV1601, Kyoto, Japan).

The mechanical properties of the membranes were evaluated according to the tensile tests carried out with a single column Universal Testing Machine (Zwick/Roell, model Z2.5, Germany) equipped with a 200 N load cell. Samples of 2.5 cm of length (distance between the clamps of the instruments) and of 1 cm of width were stretched until the breakage at a rate of 25 $mm \cdot min^{-1}$. The mean values and the standard deviations of the Young's modulus (E_{mod}), the break elongation (ε_{break}) and the tensile strength (R_m) were evaluated on a series of five samples.

6.2.5 Photocatalytic membrane distillation reactor

The experimental setup for PC-MD is shown in Fig. 6.1. To explore the synergistic effect of MD and PC, the membranes (active area of 85 cm^2) were allocated in a module equipped with a quartz window to irradiate the membrane surface. The irradiation was provided by a high-pressure UV mercury lamp installed 20 cm above the membrane module. The lamp was characterized by an emission spectrum between 240 nm and 440 nm, a maximum emission at a wavelength of 366 nm and a viewing angle of 90◦, which was connected to a 500 W power generator.

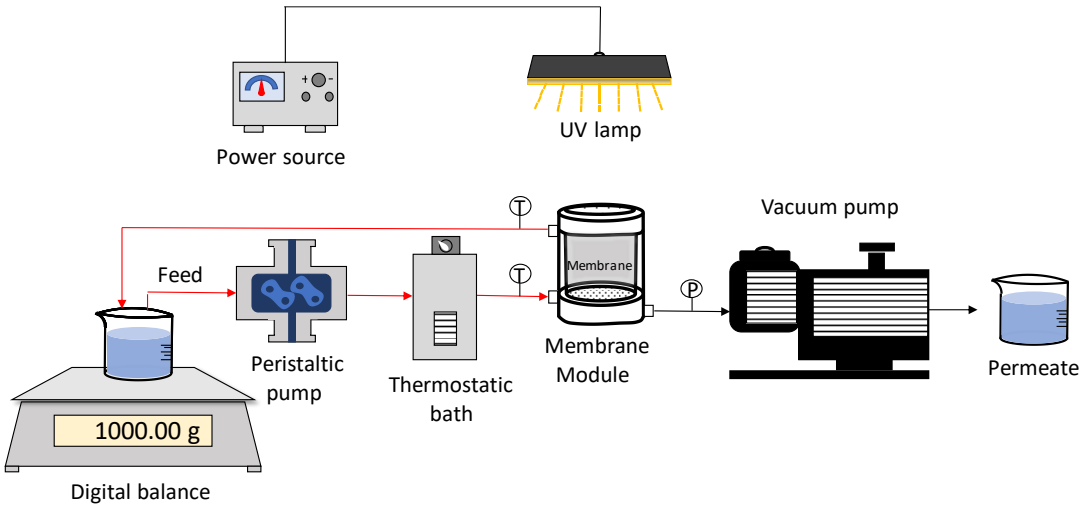


Figure 6.1. *Schematic representation of the setup for hybridization of VMD with photocatalysis for As remediation.*

The feed solution (0.4 L), thermostated at 40, 50, or 60 ◦C (±0.5 ◦C) by a Digital Plus Neslab RTE201 thermostatic bath (Thermo Scientific, Italy), was recirculated through the membrane module at a flow rate of 6 $L \cdot h^{-1}$ with a Masterflex L/S digital peristaltic pump (Cole-Palmer, USA). The initial concentration of As(III) in the feed was 0.06 $mg \cdot L^{-1}$ according to the amount of As revealed in the contaminated groundwater of the Sila Massif (Calabria, Italy) [39].

Experiments were also conducted with As-concentrated solutions (1.00 $mg \cdot L^{-1}$) to study the kinetic of PC. Thermocouples (Sper Scientific 8000024) were installed at the outlet and inlet of the membrane module to monitor the temperature. Experiments were conducted in a Vacuum Membrane Distillation (VMD) configuration, with the vaporized distillate stripped by a vacuum pump VWR VP 820 (VWR International, US) maintaining the pressure to 2 kPa.

The quality of the permeate was estimated by: i) measuring the conductivity using a YSI Model 3200 conductivity meter at 20 ◦C (range: 0–4999 µS m^{-1} , accuracy: ±0.50 % full scale); ii) detecting the eventual leakage of TiO_2 NPs from the membrane by Dynamic Light Scattering (DLS) 90Plus Particle Size Analyzer (Brookhaven Instruments Corporation, USA); and iii) estimating the As concentration with HR-CS AAS and analytical kits.

The transmembrane flux was evaluated by recording the weight variations of the feed tank over time using an analytical balance REFLEX HP 8200 (US) with a precision of ± 0.1 g.

6.3 Results

6.3.1 Membrane characterization

Table 2 summarizes the physical– chemical properties of the lab-made PVDF-based membranes. The membranes presented thicknesses (l) of 105–116 µm and mean pore size (d_{mean}) from 0.123 µm to 0.129 µm, failing in the range of 0.05–0.5 µm typical for MD applications [42]. The largest pore size (d_{max}) ranged from 0.272 µm to 0.288 µm, thus meeting the requirement of MD membranes for a narrow pore size below than 0.5 µm to mitigate the risk of pore wetting [42]. In all cases, the PVDF membranes showed porosities (ε) above 80 % securing minimal resistance to mass transport and modest heat conductivity, both desired in MD to ensure high transmembrane flux and to reduce the impact of temperature polarization [43, 44]. These interesting features are attributed to the use of PVP and PEG as additives able to increase the pore size and porosity of the membrane without affecting their homogeneity [45]. With respect to this, several studies reported that the solubilization of appropriate amounts of PVP and PEG in PVDF solutions balances the enhancement of thermodynamic instability of the dope solution (responsible for a high demixing rate with a subsequent increase of the porosity) and the increase of viscosity (slowing the diffusion of the nonsolvent into the polymeric solution and mitigating the formation of heterogeneities) [45, 46, 47]. Moreover, both PVP and PEG are soluble in water and easily removed from the membrane during the NIPS and washing phases [45, 46, 47]. Interestingly, while the presence of TiO_2 NPs in MMMs poorly affected the values of the pore size, the photocatalyst slightly improved the membrane porosity: the value of ε progressively increased from 80.5 ± 1.3 % for bare PVDF membranes (M0) to 83.4 ± 1.4 % for the membrane load with 7 % TiO_2 (M7). This trend could be attributed to the hydrophilic nature of the TiO_2 [48] that facilitates the solvent and non-solvent de-mixing during the NIPS process, leading to superior porosity [49], as clearly observed for PVDF hollow fiber showing an enhancement of the porosity from 35.5 % to 81.4 % with the loading of TiO_2 NPs from 0 wt% to 3 wt% [50].

Table 2. *Summary of membrane characterizations.*

Membrane	l (µm)	d_{mean} (µm)	d_{max} (µm)	ε (%)	WCA_{Air} (°)	WCA_{Glass} (°)
M0	116±2	0.127±0.006	0.272±0.002	80.5±1.3	93±2	122±2
M2.5	105±3	0.129±0.004	0.278±0.004	81.9±1.0	93±2	120±4
M5	109±2	0.124±0.005	0.288±0.008	83.1±1.5	93±2	118±5
M7	108±3	0.123±0.006	0.284±0.008	83.4 ±1.4	91±2	119±4

On the other hand, the presence of the hydrophilic TiO_2 NPs did not compromise the hydrophobicity of the membrane surface; the measurements of the contact angle of the surfaces of the membranes exposed to the atmosphere during the casting process (WCA_{air}) showed values in the range of 93-91◦. Furthermore, the surfaces obtained from the cast polymeric solution in contact with the glass in the NIPS process presented a contact angle (WCA_{glass}) of 120 ± 2◦.

SEM inspections clarified that the discrepancies in the measurements of the contact angles of the two surfaces are related to differences in terms of morphology (Fig. 6.2 a and b). In general, during the membrane casting, the solvent partially evaporates from the surface of the polymeric solution developing a polymer concentration gradient along the cross section of the nascent membrane resulting in asymmetric structures [51]. According to Smolders et al. [52], finger-like macrovoids are generated by the nuclei of the polymeric lean phase formed below a dense skin top-layer. Strathmann et al. [53] also suggested that the immersion of the cast polymeric solution into the coagulation bath provoked a rapid non-solvent/solvent exchange from the surface in direct contact with the coagulation bath (air surface), inducing the formation of a finger-like morphology (Fig. 6.2 c) [54]. On the other hand, the slow permeation (i.e., diffusion) of the non-solvent (i.e., water of the coagulation bath) into the nascent membrane delayed the demixing on the opposite surface (glass surface), resulting in a sponge-like morphology (Fig. 6.2 d) [55].

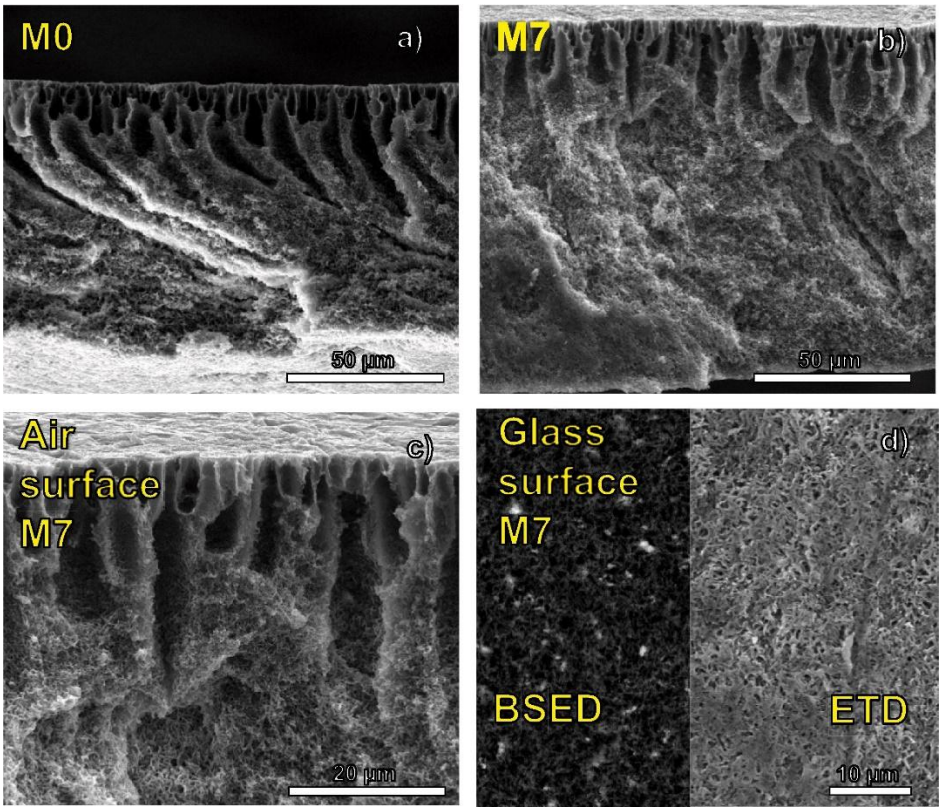


Figure 6.2. *a) Cross section of bare PVDF membrane (M0) at a magnification of 2,000; b) cross section of PVDF membrane doped with 7 wt% of TiO_2 NPs (M7) at a magnification of 2,000; c) zoom of the cross section of the air surface of M7 at a magnification of 5,000; d) glass surface of M7 observed with backscattered electron detector (left) and Everhart– Thornley detector (ETD).*

The latter morphology is usually characterized by superior roughness, which increases the apparent contact angle, as predicted by Wenzel [56, 57]. Based on this superior hydrophobic behaviour, the bottom surface is more appropriate to be in contact with the feed solution in VMD experiments, thus limiting the wetting phenomena [58]. Moreover, TiO_2 NPs did not affect the membrane morphologies, and the NPs were clearly embedded into the polymeric network, especially visible with the backscattered electron detector (BSED) in Fig. 6.2 d and detected with SEM-EDX. Additionally, analytical analysis proved the absence of leaked TiO_2 NPs in the coagulation and washing baths, confirming their proper embodiment.

UV–Vis spectra of photocatalytic membranes reported in Fig. 6.3 showed that the embodiment of TiO_2 NPs notably increased the absorbance intensities in the UV region. While PVDF membranes did not absorb radiation for wavelengths above 250 nm, the presence of the semiconductor photocatalyst conferred to the polymer a wide absorption band in the range from 250 nm to 400 nm with a maximum at ca. 320 nm, coherently with the electronic transitions associated with the energy gap of TiO_2 [59]. Interestingly, the intensity of the band progressively increased with the concentration of the TiO_2 NPs up to 5 wt%, whereas a minimal improvement was observed by

increasing the con centration of the photocatalyst from 5 wt% (M5) to 7 wt% (M7). This is probably related to the fact that a high concentration of the photo catalytic fillers promoted the formation of aggregates (insert of Fig. 6.3) with a successive reduction of the active surface available for light absorption.

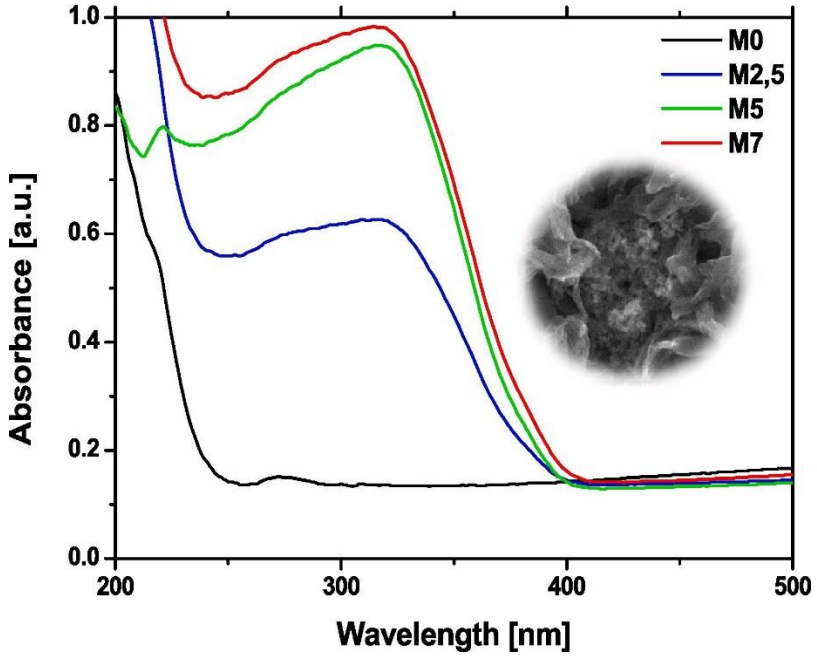


Figure 6.3. *UV–Vis spectra and details of an aggregate of TiO_2 NPs in a PVDF membrane doped with 7 wt% of TiO_2 NPs (M7) observed by SEM at a magnification of 100,000 (insert).*

6.3.2 VMD performance

VMD tests using As-contaminated distilled water ([As(III)] = 0.06 mg·L^{-1}) as feed (flow rate = 6 L·h^{-1}) were performed at different temperatures. The values reported in Fig. 6.4 a and b are the mean values of the flux observed over 6 h of experiments. The transmembrane flux measured for the MMM embedding 7 wt% of the photocatalyst (M7) increased from 1.3 ± 0.1 kg·m^{-2}·h^{-1} to 6.3 ± 0.3 kg·m^{-2}·h^{-1} by raising the feed temperature from 40 ◦C to 60 ◦C in the absence of UV irradiation (Lamp off). This behavior is a consequence of the exponential increase of the vapor pressure at the feed interface (p^{feed}) with the temperature (T^{feed}) [60], positively affecting the transmembrane flux (J) expressed as:

$$J = K\,(p^{feed} - p^{vacuum}) \qquad (2)$$

where p^{vacuum} is the vacuum pressure in the distillate compartment (2 kPa) and K is an empirical constant. In fact, the value of p_{feed} increased from 7.38 kPa at 40 ◦C to 19.95 kPa at 60 ◦C, as determined by the Antonie equation [61].

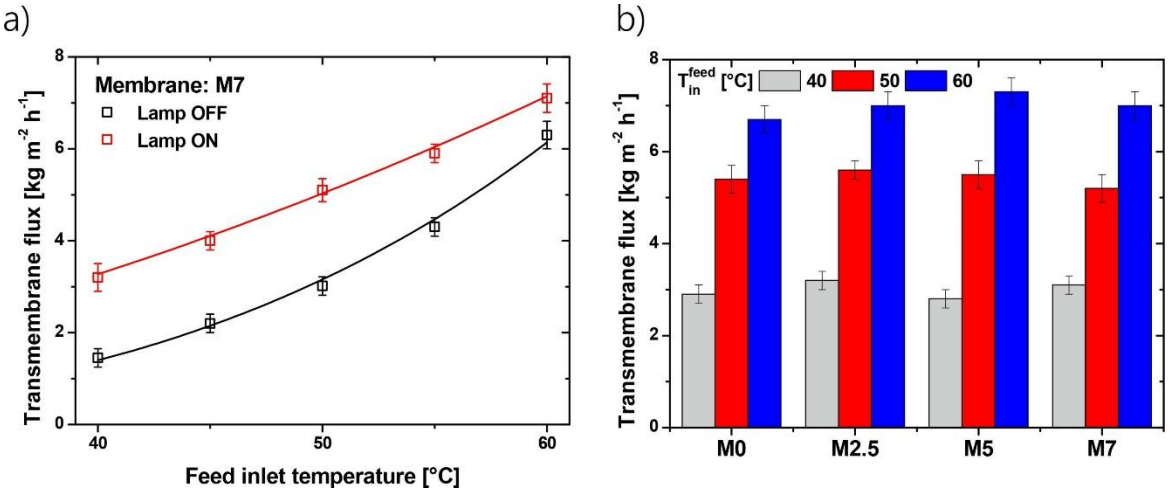


Figure 6.4. *a) Average transmembrane fluxes of MMM loaded with 7 wt% of TiO_2 NPs (M7) in VMD experiments in the presence (Lamp ON) or absence (Lamp OFF) of UV irradiation at different feed temperatures; b) Transmembrane fluxes of PVDF membranes with different loadings of TiO_2 NPs in the presence (Lamp ON) of UV irradiation at different feed temperature.*

According to Fig. 6.4 a, the presence of UV irradiation (Lamp on), employed to activate the photocatalyst, boosted the water vaporization rate over the entire range of the investigated temperatures. This behavior is due to the radiant heating power of the UV radiation absorbed by the VMD cell, estimated to be about 104 $W \cdot m^{-2}$. Feeding water at 60 ◦C in the absence of UV irradiation, the temperature of the retentate at the outlet of the membrane module was 57.9 ◦C as a consequence of heat losses by conduction across the membrane and by latent heat of vaporization associated with the transmembrane flux [62]. On the other hand, when the UV lamp was turned on, the additional radiative heat raised the outlet temperature of the retentate stream to 61.4 ◦C, leading to a transmembrane flux enhancement of ca. 12.7 %. Analogous impacts were observed for all the developed membranes.

Likewise, the experiments under UV irradiation were completed (6 h) without flux deterioration, confirming the stability of the photocatalytic MMMs even in the case of high TiO_2 loading (M7). In all cases, the concentration of As(III) in the distillate after 6 h of VMD practice was below to detection limit of analytical methodologies (0.005 $mg \cdot L^{-1}$) confirming the potentialities of VMD in producing high-quality distilled water from contaminated As aqueous solutions, even below the rigorous WHO drinking water standard.

Interestingly, the presence of the TiO_2 NPs had a poor impact on the VMD performance of the PVDF-based membranes (Fig. 6.4 b): the impact of the variation of the TiO_2 NP content from 0 wt% (M0) to 7 wt% (M7) on the transmembrane flux was below 10%; this was due to the modest impact of the photocatalyst on the morphological and chemical-physical properties of PVDF membranes (Table 2).

Although the presence of UV irradiation increased the VMD productivity (transmembrane flux raised of the 12.7 % at an inlet feed temperature of 60 ◦C), the employment of the highly energy intensive lamp drastically increased the specific energy consumption of the process (in the order of 104 $KWh \cdot m^{-3}$). This suggested that the treatment of diluted As-contaminated solutions with UV radiation is not feasible from an energetic point of view, highlighting the need for the use of an up stream process for the dehydration of the feed before As remediation. From this perspective, the developed photocatalytic MMMs could be used in two consecutive stages: i) a preliminary VMD step in the absence of UV irradiation aimed at recovering large amounts of water while concentrating As; and ii) a second PC-VMD step under UV irradiation to convert As(III) into As(V), which can be subsequently removed by filtration through absorbent media.

Fig. 6.5 clarifies the capabilities of VMD in the recovery of water from the As-contaminated aqueous solution. The lowest performance was recorded at a feed inlet temperature of 40 ◦C when only 17.8 % (Fig. 6.5 a) of the water was recovered after 6 h due to the relatively low trans membrane flux (1.3 $kg \cdot m^{-2} \cdot h^{-1}$); this provoked a minimal improvement of the concentration of As in the retentate from 0.06 $mg \cdot L^{-1}$ to 0.07 $mg \cdot L^{-1}$ (Fig. 6.5 b). The enhancement of the transmembrane flux to 6.3 $kg \cdot m^{-2} \cdot h^{-1}$ by raising the feed inlet temperature to 60 ◦C improved the water recovery factor up to 80.5 % (Fig. 6.5 a), with a consequent increase in the As concentration from 0.06 $mg \cdot L^{-1}$ to 0.31 $mg \cdot L^{-1}$(Fig. 6.5 b).

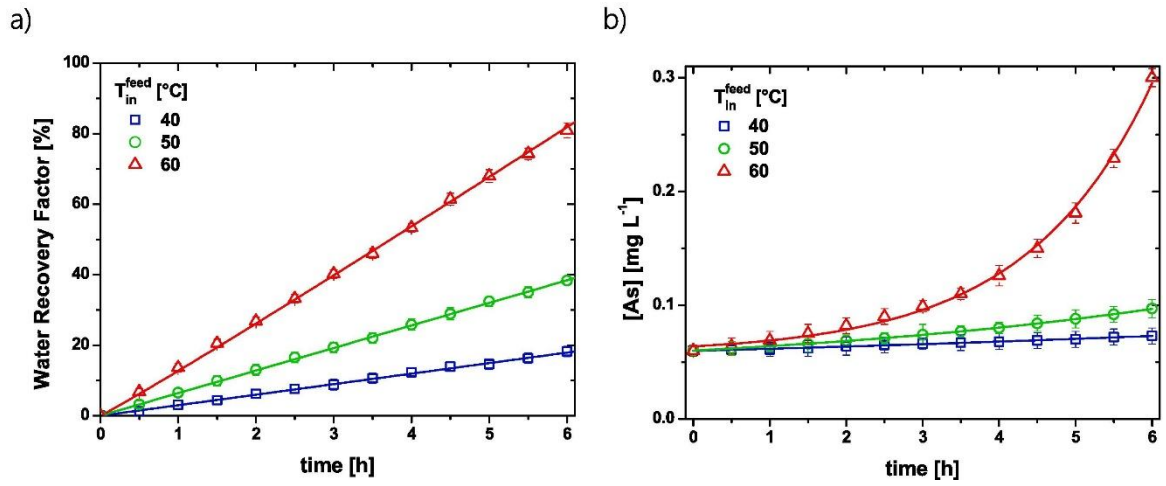


Figure 6.5. *a) water recovery factor and b) evolution of as concentration in the retentate stream during 6 h of VMD experiments carried out with M7 membrane at different feed temperatures in the absence of UV irradiation.*

The transmembrane flux was not dependent on the As(III) concentration; for instance, the transmembrane flux of M7 exhibited a modest variation of 6 % despite the As concentration being raised 5-folds. This is due to the low sensitivity of the MD process to the solute concentration in the diluted solution. As per Raoult's equation, the vapor pressure of the feed solution (p^{feed}) depends on the vapor pressure of pure water (p_0 ^{feed}), the molar fraction (x_w), and the activity coefficient (γ_w) of water:

$$p^{feed} = p_0^{feed} \cdot x_w \cdot \gamma_w \qquad (3)$$

In the case of the diluted solution, both x_w and γ_w tend toward 1 making p^{feed} close to p_0^{feed}.
DLS and HR-CS AAS analysis of both permeate and retentate confirmed the absence of leakage phenomenon of the TiO_2 NPs from the membranes to the aqueous phases.

6.3.3 Photocatalytic membranes for As (III) oxidation in As (V)

To assess the photocatalytic performance of the lab-made MMMs, an aqueous solution of As (III) of 1.00 mg·L^{-1} was recirculated for 3 h to the membrane module in the presence of UV radiation at different inlet temperatures. As expected, the bare PVDF membrane (M0) was found to be ineffective in the photo-oxidation of As leading to an improvement of the As (III) concentration coherent with the dehydration of the solution (Fig. 6.6 a). On the other hand, a substantial reduction

in As (III) concentration was observed for the PVDF membranes doped with TiO_2 NPs. Using M2.5, the arsenite concentration decreased to 0.71 mg·L^{-1} at 40 ◦C, whereas almost 50 % of As (III) was converted into arsenate at 60 ◦C (Fig. 6.6 b). The increase of the TiO_2 content incorporated into the PVDF matrix to 5 wt% (M5) increased the photocatalytic performance, leading to a reduction of As (III) concentration to 0.28 mg·L^{-1} at 60 ◦C. The best performance was observed for the membrane with the highest loading of the catalyst: M7 decreased the concentration of arsenite to 0.44 mg·L^{-1} at 40 ◦C and further decreased it to 0.09 mg·L^{-1} when the temperature was increased to 60 ◦C.

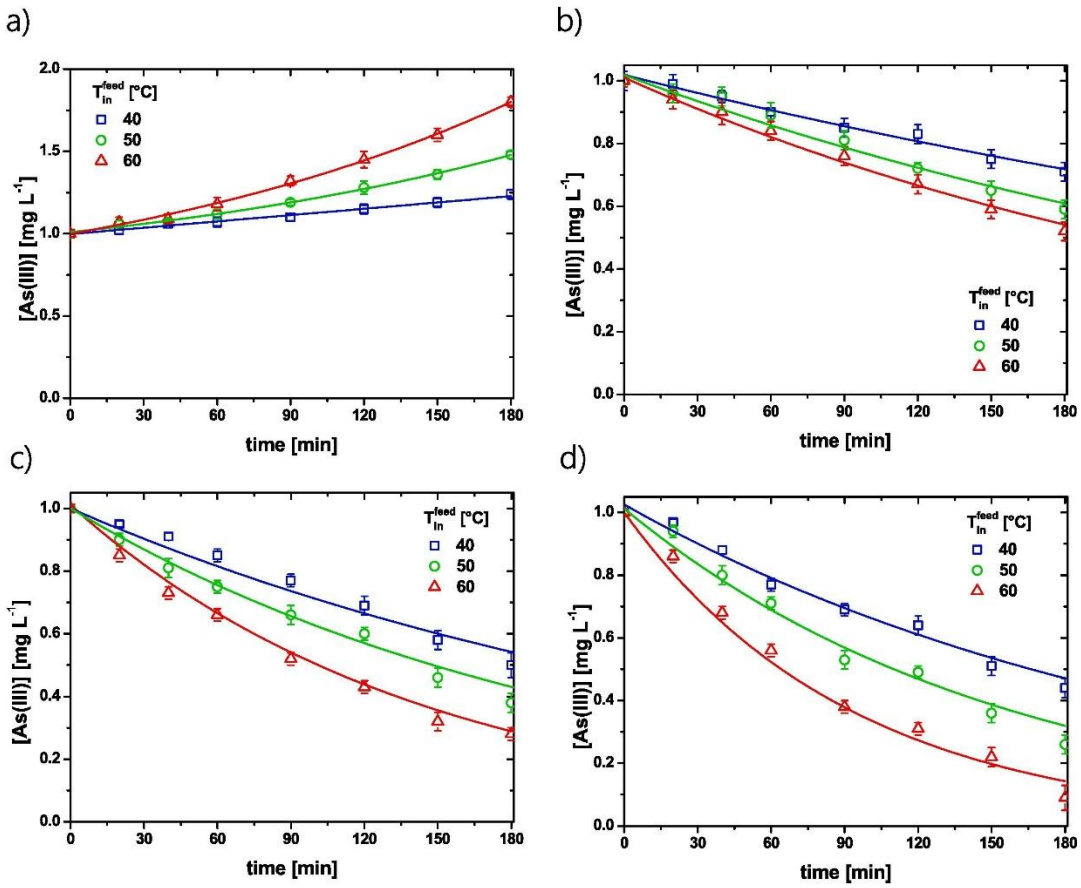


Figure 6.6. *Time evolution of the As(III) concentration in PC-VMD tests at different temperatures carried out with: a) M0, b) M2.5, c) M5, and d) M7 membranes.*

In general, higher feed temperatures increase the rate of the photocatalytic reaction. When TiO_2 NPs are irradiated with radiation matching their band gap, electron– hole (e^- -h^+) pairs are generated in the conduction and valence bands [63]. In an aqueous system, h^+ easily reacts with H_2O, leading to the generation of $OH^•$ radicals consisting of highly oxidizing species [64]. Higher temperatures of the reaction system (aqueous medium where the reaction occurs) improve the mobility of the e^- -h^+ pairs photogenerated by the semiconductor materials. In fact, several studies have demonstrated that temperatures above 80 ◦C limit the photo-oxidation activity of TiO_2 NPs by favoring the

recombination of the e^- -h^+ pairs [65], while in the range of 20–70 ◦C, the photocatalytic activity increases with temperature [65, 66], which is consistent with our observations. These materials being photothermal photocatalytic are also capable of absorbing photons and simultaneously generate heat by dissipating it to the environment, which would lead to the acceleration of the photocatalytic reaction by increasing the mobility of charge carriers in the material [67].

In all cases, the concentration of arsenite during the experiment exponentially decreased according to a first-order kinetics ($R^2 > 0.96$) [68, 69]:

$$[As(III)]_t = [As(III)]_0 \cdot \exp(-kt) \qquad (4)$$

where $[As(III)]_0$ is the initial arsenite concentration (1 mg·L^{-1}), $[As(III)]_t$ is the concentration of As(III) at the generic irradiation time t, and k is the experimentally observed first-order kinetic constant. The value of k increased with the concentration of the photocatalyst from 0.0019 min^{-1} for M2.5 to 0.0034 min^{-1} for M5 achieving 0.0044 min^{-1} for M7 (feed inlet temperature of 40 ◦C). As expected in view of the UV–Vis spectra (Fig. 6.3) and the aggregates observed for M7, the value of k does not increase proportionally to the amount of TiO_2 loaded in the membrane. The value of k also raised with feed temperature, reaching a maximum value of 0.0106 min^{-1} for M7 at 60 ◦C; one order of magnitude lower than the one (k = 0.123 min^{-1}) observed for a colloidal dispersion of 0.05 g·L^{-1} of TiO_2 NPs in water containing an initial con centration of arsenate of 0.5 mg·L^{-1} [37]. This is due to the direct contact of the photocatalyst with the contaminant solubilized in water, facilitating photo-oxidation. Although the superior effectiveness of the suspension of the TiO_2 NPs in the As-contaminated aqueous solution with respect to their embodiment into the membrane, the submicrometric sizes of the photocatalyst imposes sophisticated and expensive strategies for its separation and recovery from the treated water, hindering the feasibility at large scale [70].

The benefits of the photo-oxidation were corroborated by the filtration of the treated solutions with aluminosilicate-based absorbent media able to effectively remove the oxidized state of As, while As(III) was not absorbed.

6.3.4 PC - VMD for as remediation

The efficiency of the photocatalytic membranes for treating As-contaminated solutions was evaluated by performing a first stage of VMD (lasting 4.5 h) followed by a second stage of PC-VMD (lasting 1.5 h) employing the membrane loaded with 7 wt% of TiO_2 (M7). To evaluate the eventual interference of other ions, experiments were conducted by feeding a sample of real water to the membrane module (feed inlet temperature of 60 °C) with the composition reported in Table 3.

Table 3. *Ionic composition of a real water sample (major ions are reported).*

Ion	HCO_3^-	Cl^-	Na^+	Ca^{2+}	SO_4^{2-}	Mg^{2+}	K^+	NO_3^-	F^-	As(III)
$mg \cdot L^{-1}$	30.9	10.1	9.7	30.9	10.1	1.4	0.6	0.1	0.1	0.06

The transmembrane flux in the absence of UV irradiation was 6.1 ± 0.2 $kg \cdot m^{-2} \cdot h^{-1}$. As predicted by Equation (3), the presence of ions poorly affected the evaporation rate: a reduction of less than 3 % was observed in the VMD experiments with respect to the experiments conducted with distilled water contaminated by As (0.06 $mg \cdot L^{-1}$). The conventional VMD operation allowed the recovery of 58.3 % of water, raising the concentration of As(III) in the retentate to 0.15 $mg \cdot L^{-1}$, while As(V) was absent in the retentate stream (Fig. 6.7).

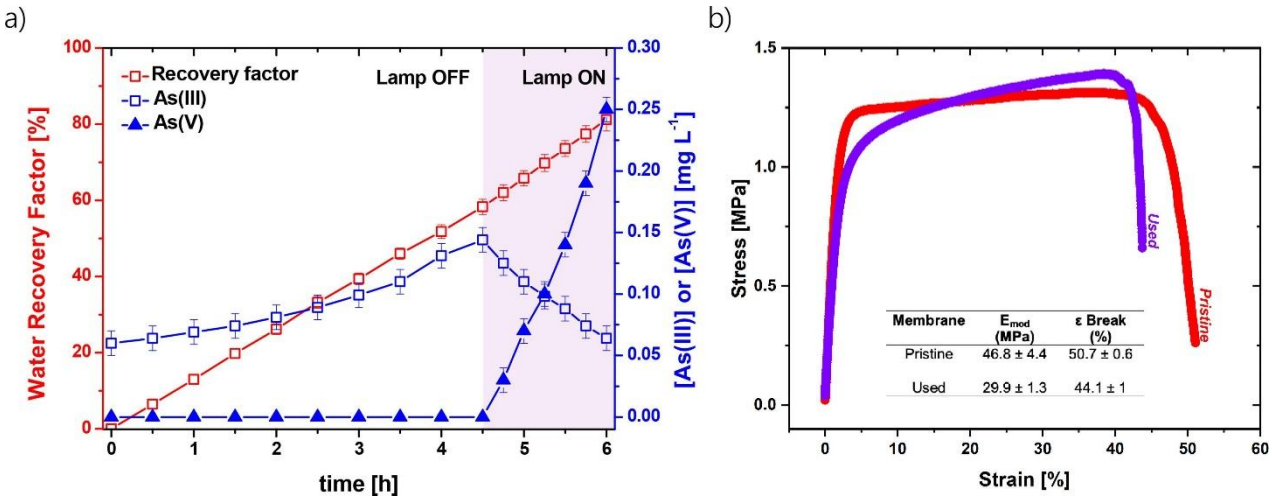


Figure 6.7. *a) Evolution of the recovery factor and As(III) and As(V) concentrations in experiments of conventional VMD followed by PC-VMD (Lamp ON) carried out at 60 °C with M7 using multi-ion solution contaminated by As (0.06 mg·L^{-1}) as feed. b) Mechanical properties of M7 before (pristine) and after five cycles of PC-VMD (used).*

In the subsequent 1.5 h of PC-VMD (Lamp ON), the heat transferred by the irradiation to the membrane module resulted in an improvement of the transmembrane flux to 7.1 ± 0.2 kg·m^{-2}·h^{-1} increasing the water recovery factor up to 80.9 %.

On the other hand, the exposure of M7 to UV light activated the photocatalyst embedded in the PVDF microporous membrane. Therefore, despite the dehydration of the feed concentrated the As species to 0.31 mg·L^{-1}, the concentration of As(III) progressively reduced from 0.15 mg·L^{-1} to 0.06 mg·L^{-1} coupled with an improvement of As(V) concentration to 0.25 mg·L^{-1}.

The photo-oxidation of As(III) to As(V) was in agreement with the first-order kinetics reported in Equation (4), but the value of k reduced from 0.0106 min^{-1} to 0.0071 min^{-1}. This effect is mostly related to the presence of bicarbonate ions interfering with the photo-oxidation process. In fact, HCO_3^- ions compete with As(III), especially with hydroxyl radicals [71]. Thus, the treatment of a real solution could require an early stage treatment to remove the HCO_3^- ions [72].

After five cycles of PC-VMD experiments, a *post-hoc* characterization was conducted to assess the impact of the long-term exposure to the UV irradiation on the mechanical stability of M7. As reported in Fig. 6.7 b, PC-VMD experiments poorly impacted on the mechanical resistance of the membranes since both pristine and used membranes demonstrated tensile strengths (R_m) failing in the range of 1.3–1.4 MPa. Nevertheless, the used membranes showed a minor reduction of elastic properties visible by the decrease with respect to the pristine membrane of both the Young Modulus (E_{mod}) from 46.8 MPa to 29.9 MPa and the elongation at break (ε_{break}) from 50.7 % to 44.6 %. The moderate temperature of MD process was insufficient to induce any detrimental thermal effect on the membrane compromising its mechanical stability (PVDF melting point occurs at temperature above 160 °C [73]). Thus, the observed embrittlement of the membrane was caused by UV radiation able to promote oxidation reactions, chain-scissions and decompositions of PVDF [74, 75, 76]. The embrittlement phenomenon highlights the inherent challenges associated with the limited long-term stability of polymeric membranes when exposed to UV irradiation. Moving forward, future studies will focus on exploring novel approaches such as employing UV-resistant supports and utilizing solar-activated photocatalysts to address the stability issues encountered in UV-activated PVDF-based photocatalytic membranes.

6.4 Conclusions

This work proposed a novel integrated MD and photo-oxidation process by doping microporous hydrophobic PVDF membranes with TiO_2 NPs, enabling the simultaneous recovery of high-quality freshwater and the conversion of As(III) into As(V), the latter being less toxic and easily removed with well-established technologies.

MMMs were prepared according to the NIPS protocol using TEP as the green solvent in a dispersion of TiO_2 NPs where PVDF was solubilized. Additives (PEG and PVDF) ensured the fabrication of highly porous membranes ($\varepsilon > 80$ %) with a narrow pore size (dmean in the range of 0.123–0.129 μm and largest pore below to 0.288 μm). Likewise, the membranes presented an asymmetric structure with a finger-like top layer on a spherulitic structure. This caused an asymmetry in hydrophobicity because the superior roughness of the spherulitic structure raised the contact angles to 120 ± 2°, whereas a contact angle of 92 ± 1° was observed for the smoother surface with a finger-like morphology.

Notably, the increase in the TiO_2 NP concentration from 0 wt% (M0) to 7 wt% (M7) did not affect the morphological properties of the membrane, despite the aggregates observed for the MMMs with the highest loading of the photocatalyst (M7). On the other hand, the enhancement of the TiO_2 content increased the absorbance in the UV region of the spectrum.

VMD experiments demonstrated the ability of the lab-made photocatalytic MMMs to recover more than 80 % of water from As contaminates solution, enhancing the concentration of As(III) 5-folds. Moreover, the transmembrane flux raised from 1.2 ± 0.1 $kg \cdot m^{-2} \cdot h^{-1}$ to 6.3 ± 0.3 $kg \cdot m^{-2} \cdot h^{-1}$ when increasing the feed temperature from 40 °C to 60 °C in the absence of UV irradiation. By switching on the UV lamp, the flux further increased to 7.1 ± 0.2 $kg \cdot m^{-2} \cdot h^{-1}$ (inlet feed temperature of 60 °C) due to the radiant heating power of the UV radiation. Likewise, M7 membranes were able to photo-oxidize As(III) to As(V) under UV irradiation with a first-order kinetic constant of 0.0106 min^{-1} at 60 °C. However, because of the higher energy consumption of the UV lamp, it is convenient to exploit the photocatalytic properties of the membranes to treat As concentrated solutions.

The potential of the novel membrane technology was assessed by treating real water in two consecutive stages: i) VMD (4.5 h) to recover 58.3 % of the water concentrating As(III) up to 0.15 $mg \cdot L^{-1}$; and ii) PC-VMD under UV light (1.5 h) to intensify the recovery of water up to 80 % and to ensure the abatement of the concentration of As(III) to 0.06 $mg \cdot L^{-1}$ via its photo-oxidation into As(V), the latter effortlessly removed by filtration with alluminosilicates.

Post-hoc mechanical test on M7 employed in 5 cycles of PC-VMD (total irradiation time: 7.5 h) revealed the emergence of polymer embrittlement induced by the UV radiation. These findings

underscore the pressing need for the development of photocatalytic membranes with long-term stability.

Overall, this work demonstrated the advantages of combining MD and photo-oxidation in a single process by employing green hydrophobic microporous membranes with photocatalytic properties that are exploitable for continuous and intensified remediation of As -contaminated waterbodies.

References

[1] Agency for Toxic Substances and Disease Registry (ATSDR), Priority list of hazardous substances, (n.d.). https://www.atsdr.cdc.gov/spl/index.html#2022spl (accessed April 1, 2023).

[2] World Health Organization's (WHO), World Health Organization. Guidelines for Drinking-Water Quality, 2017.

[3] K. Khanna, S.K. Kohli, P. Kumar, P. Ohri, R. Bhardwaj, P. Alam, P. Ahmad. Arsenic as hazardous pollutant: perspectives on engineering remediation tools, Sci. Total Environ., 838 (2022), Article 155870, 10.1016/j.scitotenv.2022.155870

[4]P. Bhattacharya, A.H. Welch, K.G. Stollenwerk, M.J. McLaughlin, J. Bundschuh, G. Panaullah Arsenic in the environment: biology and chemistry, Sci. Total Environ., 379 (2007), pp. 109-120, 10.1016/j.scitotenv.2007.02.037

[5]S. Bhowmick, B. Nath, D. Halder, A. Biswas, S. Majumder, P. Mondal, S. Chakraborty, J. Nriagu, P. Bhattachary a, M. Iglesias, G. Roman-Ross, D.G. Mazumder, J. Bundschuh, D. Chatterjee. Arsenic mobilization in the aquifers of three physiographic settings of West Bengal, India: understanding geogenic and anthropogenic influences, J. Hazard. Mater., 262 (2013), pp. 915-923, 10.1016/j.jhazmat.2012.07.014

[6] S. Quazi, D. Sarkar, R. Datta. Human health risk from arsenical pesticide contaminated soils: a long-term greenhouse study, J. Hazard. Mater., 262 (2013), pp. 1031-1038, 10.1016/j.jhazmat.2012.10.027

[7] J.O. Nriagu, P. Bhattacharya, A.B. Mukherjee, J. Bundschuh, R. Zevenhoven, R.H. Loeppert, Arsenic in soil and groundwater: an overview, in: Arsen. Soil Groundw. Environ., Elsevier, 2007: pp. 3–60. 10.1016/S1875-1121(06)09001-8

[8]S. Santoro, H. Estay, A.H. Avci, L. Pugliese, R. RubyFigueroa, A. Garcia, M. Aquino, S. Nasirov, S. Straface, E. Curcio. Membrane technology for a sustainable copper mining industry: the chilean paradigm, Clean. Eng. Technol., 2 (2021), Article 100091, 10.1016/j.clet.2021.100091

[9] A.K. Sharma, J.C. Tjell, J.J. Sloth, P.E. Holm. Review of arsenic contamination, exposure through water and food and low cost mitigation options for rural areas, Appl. Geochemistry., 41 (2014), pp. 11-33, 10.1016/j.apgeochem.2013.11.012

[10] R. Singh, S. Singh, P. Parihar, V.P. Singh, S.M. Prasad. Arsenic contamination, consequences and remediation techniques: a review, Ecotoxicol. Environ. Saf., 112 (2015), pp. 247-270, 10.1016/j.ecoenv.2014.10.009

[11] S. Santoro, A.H. Avci, M. Aquino, L. Pugliese, S. Straface, E. Curcio, Towards the Global Rise of Zero Liquid Discharge for Wastewater Management: The Mining Industry Case in Chile, in: Springer Berlin Heidelberg, Berlin, Heidelberg, 2021: pp. 1–14. 10.1007/698_2021_785

[12]S. Radić, H. Crnojević, V. Vujčić, G. Gajski, M. Gerić, Ž. Cvetković, C. Petra, V. Garaj-Vrhovac, V. Oreščanin. Toxicological and chemical assessment of arsenic-contaminated groundwater after electrochemical and advanced

oxidation treatments, Sci. Total Environ., 543 (2016), pp. 147-154, 10.1016/j.scitotenv.2015.10.158

[13] R. Molinari, P. Argurio. Arsenic removal from water by coupling photocatalysis and complexation-ultrafiltration processes: a preliminary study, Water Res., 109 (2017), pp. 327-336, 10.1016/j.watres.2016.11.054

[14] L. Yin, L. Liu, S. Lin, G. Owens, Z. Chen. Synthesis and characterization of nanoscale zero-valent iron (nZVI) as an adsorbent for the simultaneous removal of AS(III) and as(v) from groundwater, J. Water Process Eng., 47 (2022), Article 102677, 10.1016/j.jwpe.2022.102677

[15] B.S. Rathi, P.S. Kumar. A review on sources, identification and treatment strategies for the removal of toxic arsenic from water system, J. Hazard. Mater., 418 (2021), Article 126299, 10.1016/j.jhazmat.2021.126299

[16] J. Ryu, W. Choi. Effects of TiO2 surface modifications on photocatalytic oxidation of arsenite: the role of superoxides, Environ. Sci. Technol., 38 (2004), pp. 2928-2933, 10.1021/es034725p

[17] K.K. Sirkar, A.G. Fane, R. Wang, S.R. Wickramasinghe. Process intensification with selected membrane processes, Chem. Eng. Process. Process Intensif., 87 (2015), pp. 16-25, 10.1016/j.cep.2014.10.018

[18] T. Guo, J. Englehardt, T. Wu. Review of cost versus scale: water and wastewater treatment and reuse processes, Water Sci. Technol., 69 (2013), pp. 223-234, 10.2166/wst.2013.734

[19] S. Mondal, M. Malankowska, A.H. Avci, U.T. Syed, L. Upadhyaya, S. Santoro. Chapter 10 - membrane sensors for pollution problems, A. Basile, M. Gensini, I. Allegrini, A. Figoli (Eds.), Curr. Trends Futur, Dev. Membr., Elsevier (2023), pp. 335-361, 10.1016/B978-0-12-824103-5.00004-8

[20] F.E. Ahmed, R. Hashaikeh, N. Hilal. Hybrid technologies: the future of energy efficient desalination – a review, Desalination, 495 (2020), Article 114659, 10.1016/j.desal.2020.114659

[21] M. Bassyouni, M.H. Abdel-Aziz, M.S. Zoromba, S.M.S. Abdel-Hamid, E. Drioli. A review of polymeric nanocomposite membranes for water purification, J. Ind. Eng. Chem., 73 (2019), pp. 19-46, 10.1016/j.jiec.2019.01.045

[22]S. Santoro, M. Aquino, C. Rizza, J. Occhiuzzi, D. Mastrippolito, G. D'Olimpio, A.H. Avci, J. De Santis, V. Paolucci, L. Ottaviano, L. Lozzi, A. Ronen, M. Bar-Sadan, D.S. Han, A. Politano, E. Curcio. Lithium recovery through WS2 nanofillers-promoted solar photothermal membrane crystallization of LiCl, Desalination, 546 (2023), Article 116186, 10.1016/j.desal.2022.116186

[23] I. Ounifi, Y. Guesmi, C. Ursino, S. Santoro, S. Mahfoudhi, A. Figoli, E. Ferjanie, A. Hafiane, Antifouling membranes based on cellulose acetate (CA) blended with poly(acrylic acid) for heavy metal remediation, Appl. Sci., 11 (2021), 10.3390/app11104354

[24] N. Abdullah, N. Yusof, W.J. Lau, J. Jaafar, A.F. Ismail. Recent trends of heavy metal removal from water/wastewater by membrane technologies, J. Ind. Eng. Chem., 76 (2019), pp. 17-38, 10.1016/j.jiec.2019.03.029

[25] C. Algieri, V. Pugliese, G. Coppola, S. Curcio, V. Calabro, S. Chakraborty. Arsenic removal from groundwater by membrane technology: advantages, disadvantages, and effect on human health, Groundw. Sustain. Dev., 19 (2022), Article 100815, 10.1016/j.gsd.2022.100815

[26] L. Eykens, K. De Sitter, C. Dotremont, L. Pinoy, B. Van Der Bruggen. How to optimize the membrane properties for membrane distillation: a review, Ind. Eng. Chem. Res., 55 (2016), pp. 9333-9343, 10.1021/acs.iecr.6b02226

[27]A.H. Avci, S. Santoro, A. Politano, M. Propato, M. Micieli, M. Aquino, Z. Wenjuan, E. Curcio. Photothermal sweeping gas membrane distillation and reverse electrodialysis for light-to-heat-to-power conversion, Chem. Eng. Process. - Process Intensif., 164 (2021), Article 108382, 10.1016/j.cep.2021.108382

[28]S. Abramovich, D. Dutta, C. Rizza, S. Santoro, M. Aquino, A. Cupolillo, J. Occhiuzzi, M.F. La

Russa, B. Ghosh, D. Farias, A. Locatelli, D.W. Boukhvalov, A. Agarwal, E. Curcio, M. Bar Sadan, A. Politano. NiSe and CoSe topological nodal-line semimetals: a sustainable platform for efficient thermoplasmonics and solar-driven photothermal membrane distillation, Small, 18 (2022), p. 2201473, 10.1002/smll.202201473

[29] N. Thomas, M.O. Mavukkandy, S. Loutatidou, H.A. Arafat. Membrane distillation research & implementation: lessons from the past five decades, Sep. Purif. Technol., 189 (2017), pp. 108-127, 10.1016/j.seppur.2017.07.069

[30] A.E. Kabeel, M. Abdelgaied, E.M.S. El-Said. Study of a solar-driven membrane distillation system: evaporative cooling effect on performance enhancement, Renew. Energy., 106 (2017), pp. 192-200, 10.1016/j.renene.2017.01.030

[31] F. Macedonio, E. Curcio, E. Drioli. Integrated membrane systems for seawater desalination: energetic and exergetic analysis, economic evaluation, experimental study, Desalination, 203 (2007), pp. 260-276, 10.1016/j.desal.2006.02.021

[32] M.M. Damtie, R.H. Hailemariam, Y.C. Woo, K.-D. Park, J.-S. Choi. Membrane-based technologies for zero liquid discharge and fluoride removal from industrial wastewater, Chemosphere, 236 (2019), Article 124288, 10.1016/j.chemosphere.2019.07.019

[33]N.M.A. Omar, M.H.D. Othman, Z.S. Tai, A.O.A. Amhamed, T.A. Kurniawan, M.H. Puteh, M.N.M. Sokri. Recent progress, bottlenecks, improvement strategies and the way forward of membrane distillation technology for arsenic removal from water: a review, J. Water Process Eng., 52 (2023), Article 103504, 10.1016/j.jwpe.2023.103504

[34]S. Santoro, M. Aquino, C. Rizza, A. Cupolillo, D.W. Boukhvalov, G. D'Olimpio, S. Abramovich, A. Agarwal, M.B. Sadan, A. Politano, E. Curcio. Plasmonic nanofillers-enabled solar membrane crystallization for mineral recovery, Desalination, 563 (2023), Article 116730, 10.1016/j.desal.2023.116730

[35] S. Santoro, A.H. Avci, A. Politano, E. Curcio. The advent of thermoplasmonic membrane distillation, Chem. Soc. Rev., 51 (2022), pp. 6087-6125, 10.1039/D0CS00097C

[36] Y. Choi, G. Naidu, L.D. Nghiem, S. Lee, S. Vigneswaran. Membrane distillation crystallization for brine mining and zero liquid discharge: opportunities{,} challenges{,} and recent progress, Environ. Sci. Water Res. Technol., 5 (2019), pp. 1202-1221, 10.1039/C9EW00157C

[37]S. Santoro, P. Timpano, A.H. Avci, P. Argurio, F. Chidichimo, M. DeBiase, S. Straface, E. Curcio. An integrated membrane distillation, photocatalysis and polyelectrolyte-enhanced ultrafiltration process for arsenic remediation at point-of-use, Desalination, 520 (2021), Article 115378, 10.1016/j.desal.2021.115378

[38] H. Yang, W.-Y. Lin, K. Rajeshwar. Homogeneous and heterogeneous photocatalytic reactions involving AS(III) and as(v) species in aqueous media, J. Photochem. Photobiol. A Chem., 123 (1999), pp. 137-143, 10.1016/S1010-6030(99)00052-0

[39]A. Figoli, I. Fuoco, C. Apollaro, M. Chabane, R. Mancuso, B. Gabriele, R. DeRosa, G. Vespasiano, D. Barca, A . Criscuoli. Arsenic-contaminated groundwaters remediation by nanofiltration, Sep. Purif. Technol., 238 (2020), Article 116461, 10.1016/j.seppur.2019.116461

[40] X.C. Le, S. Yalcin, M. Ma. Speciation of submicrogram per liter levels of arsenic in water: on-site species separation integrated with sample collection, Environ. Sci. Technol., 34 (2000), pp. 2342-2347, 10.1021/es991203u

[41]S. Santoro, V. Sebastian, A.J. Moro, C.A.M. Portugal, J.C. Lima, I.M. Coelhoso, J.G. Crespo, R. Mallada. Development of fluorescent thermoresponsive nanoparticles for temperature monitoring on membrane surfaces, J. Colloid Interface Sci., 486 (2017), pp. 144-152, 10.1016/j.jcis.2016.09.059

[42] L. Eykens, K. De Sitter, C. Dotremont, L. Pinoy, B. Van der Bruggen. Membrane synthesis for membrane distillation: a review, Sep. Purif. Technol., 182 (2017), pp. 36-51, 10.1016/j.seppur.2017.03.035

[43] L. Li, K.K. Sirkar. Influence of microporous membrane properties on the desalination performance in direct contact membrane distillation, J. Memb. Sci., 513 (2016), pp. 280-293, 10.1016/j.memsci.2016.04.015

[44] M.S. El-Bourawi, Z. Ding, R. Ma, M. Khayet. A framework for better understanding membrane distillation separation process, J. Memb. Sci., 285 (2006), pp. 4-29, 10.1016/j.memsci.2006.08.002

[45] T. Marino, F. Russo, A. Figoli. The formation of polyvinylidene fluoride membranes with tailored properties via vapour/non-solvent induced phase separation, Membranes (basel)., 8 (2018), p. 71, 10.3390/membranes8030071

[46] G. Ji, W. Wang, H. Chen, S. Yang, J. Sun, W. Fu, B. Yang, Z. Huang. Sustainable potassium chloride production from concentrated KCl brine via a membrane-promoted crystallization process, Desalination, 521 (2022), Article 115389, 10.1016/j.desal.2021.115389

[47] S. Simone, A. Figoli, A. Criscuoli, M.C. Carnevale, A. Rosselli, E. Drioli. Preparation of hollow fibre membranes from PVDF/PVP blends and their application in VMD, J. Memb. Sci., 364 (2010), pp. 219-232, 10.1016/j.memsci.2010.08.013

[48] S. Banerjee, D.D. Dionysiou, S.C. Pillai. Self-cleaning applications of TiO2 by photo-induced hydrophilicity and photocatalysis, Appl. Catal. B Environ., 176–177 (2015), pp. 396-428, 10.1016/j.apcatb.2015.03.058

[49] Q. Wang, Z. Wang, J. Zhang, J. Wang, Z. Wu. Antifouling behaviours of PVDF/NANO-TiO2 composite membranes revealed by surface energetics and quartz crystal microbalance monitoring, RSC Adv., 4 (2014), pp. 43590-43598, 10.1039/C4RA07274J

[50] H. Rawindran, J.-W. Lim, P.-S. Goh, M.N. Subramaniam, A.F. Ismail, N.M. Radi bin Nik, M. Daud, M. Rezaei-Dasht Arzhandi. Simultaneous separation and degradation of surfactants laden in produced water using PVDF/TiO2 photocatalytic membrane, J. Clean. Prod., 221 (2019), pp. 490-501, 10.1016/j.jclepro.2019.02.230

[51] D.-M. Wang, J.-Y. Lai. Recent advances in preparation and morphology control of polymeric membranes formed by nonsolvent induced phase separation, Curr. Opin. Chem. Eng., 2 (2013), pp. 229-237, 10.1016/j.coche.2013.04.003

[52] C.A. Smolders, A.J. Reuvers, R.M. Boom, I.M. Wienk. Microstructures in phase-inversion membranes. part 1. formation of macrovoids, J. Memb. Sci., 73 (1992), pp. 259-275, 10.1016/0376-7388(92)80134-6

[53] H. Strathmann, K. Kock, P. Amar, R.W. Baker. The formation mechanism of asymmetric membranes, Desalination, 16 (1975), pp. 179-203, 10.1016/S0011-9164(00)82092-5

[54]M. Drobek, A. Figoli, S. Santoro, N. Navascués, J. Motuzas, S. Simone, C. Algieri, N. Gaeta, L. Querze, A. Trot ta, G. Barbieri, R. Mallada, A. Julbe, E. Drioli. PVDF-MFI mixed matrix membranes as VOCs adsorbers, Microporous Mesoporous Mater., 207 (2015), pp. 126-133, 10.1016/j.micromeso.2015.01.005

[55]E. Drioli, A. Ali, S. Simone, F. Macedonio, S.A. AL-Jlil, F.S. Al Shabonah, H.S. Al-Romaih, O. Al-Harbi, A. Figoli, A. Criscuoli. Novel PVDF hollow fiber membranes for vacuum and direct contact membrane distillation applications, Sep. Purif. Technol., 115 (2013), pp. 27-38, 10.1016/j.seppur.2013.04.040

[56] R.N. Wenzel. Resistance of solid surfaces to wetting by water, Ind. Eng. Chem., 28 (1936), pp. 988-994, 10.1021/ie50320a024

[57] S. Santoro, E. Drioli, A. Figoli. Development of novel ECTFE coated PP composite hollow-fiber membranes, Coatings, 6 (2016), p. 40

[58] E. Guillen-Burrieza, M.O. Mavukkandy, M.R. Bilad, H.A. Arafat. Understanding wetting phenomena in membrane distillation and how operational parameters can affect it, J. Memb. Sci., 515 (2016), pp. 163-174, 10.1016/j.memsci.2016.05.051

[59]P. Allende, L. Barrientos, A. Orera, M.A. LagunaBercero, N. Salazar, M.L. Valenzuela, C. Diaz. TiO2/SiO2 composite for efficient protection of UVA and UVB rays through of a solvent-less synthesis, J. Clust. Sci., 30 (2019), pp. 1511-1517, 10.1007/s10876-019-01594-9

[60]S. Santoro, I. Vidorreta, I. Coelhoso, J.C. Lima, G. Desiderio, G. Lombardo, E. Drioli, R. Mallada, J. Crespo, A. Criscuoli, A. Figoli. Experimental evaluation of the thermal polarization in direct contact membrane distillation using electrospun nanofiber membranes doped with molecular probes, Molecules, 24 (2019), p. 638, 10.3390/molecules24030638

[61] E. Curcio, E. Drioli. Membrane distillation and related operations—A review, Sep. Purif. Rev., 34 (2005), pp. 35-86, 10.1081/SPM-200054951

[62]F. Russo, S. Santoro, F. Galiano, C. Ursino, E. Avruscio, E. DiNicolò, G. Desiderio, G. Lombardo, A. Criscuoli, A. Figoli. A luminescent thermosensitive coating for a non-invasive and in-situ study of thermal polarization in hollow fiber membranes, J. Memb. Sci., 685 (2023), Article 121928, 10.1016/j.memsci.2023.121928

[63]M. Rosales, J. Orive, R. EspinozaGonzález, R. FernándezdeLuis, R. Gauvin, N. Brodusch, B. Rodríguez, F. Gracia, A. García. Evaluating the bi-functional capacity for arsenic photo-oxidation and adsorption on anatase TiO2 nanostructures with tunable morphology, Chem. Eng. J., 415 (2021), Article 128906, 10.1016/j.cej.2021.128906

[64] N. Barka, S. Qourzal, A. Assabbane, A. Nounah, Y. Ait-Ichou. Photocatalytic degradation of an azo reactive dye, reactive yellow 84, in water using an industrial titanium dioxide coated media, Arab. J. Chem., 3 (2010), pp. 279-283, 10.1016/j.arabjc.2010.06.016

[65] N. Daneshvar, M. Rabbani, N. Modirshahla, M.A. Behnajady. Kinetic modeling of photocatalytic degradation of acid red 27 in UV/TiO2 process, J. Photochem. Photobiol. A Chem., 168 (2004), pp. 39-45, 10.1016/j.jphotochem.2004.05.011

[66] Y.-W. Chen, Y.-H. Hsu. Effects of reaction temperature on the photocatalytic activity of TiO2 with pd and cu cocatalysts, Catalysts, 11 (2021), 10.3390/catal11080966

[67] X. Wang, Y. He, Y. Hu, G. Jin, B. Jiang, Y. Huang. Photothermal-conversion-enhanced photocatalytic activity of flower-like CuS superparticles under solar light irradiation, Sol. Energy., 170 (2018), pp. 586-593, 10.1016/j.solener.2018.06.022.

[68] M. Bissen, M.M. Vieillard-Baron, A.J. Schindelin, F.H. Frimmel. TiO2-catalyzed photooxidation of arsenite to arsenate in aqueous samples, Chemosphere, 44 (2001), pp. 751-757, 10.1016/S0045-6535(00)00489-6

[69] A. García, M. Rosales, M. Thomas, G. Golemme. Arsenic photocatalytic oxidation over TiO2-loaded SBA-15, J. Environ. Chem. Eng., 9 (2021), Article 106443, 10.1016/j.jece.2021.106443

[70] S. Leong, A. Razmjou, K. Wang, K. Hapgood, X. Zhang, H. Wang. TiO2 based photocatalytic membranes: a review, J. Memb. Sci., 472 (2014), pp. 167-184, 10.1016/j.memsci.2014.08.016

[71] X. Guan, J. Du, X. Meng, Y. Sun, B. Sun, Q. Hu. Application of titanium dioxide in arsenic removal from water: a review, J. Hazard. Mater., 215–216 (2012), pp. 1-16, 10.1016/j.jhazmat.2012.02.069

[72] R. Molinari, A.H. Avci, P. Argurio, E. Curcio, S. Meca, M. Plà-Castellana, J.L. Cortina. Selective precipitation of calcium ion from seawater desalination reverse osmosis brine, J. Clean. Prod., 328 (2021), Article 129645, 10.1016/j.jclepro.2021.129645

[73] Y. Tang, Y. Lin, W. Ma, X. Wang. A review on microporous polyvinylidene fluoride membranes fabricated via thermally induced phase separation for MF/UF application, J. Memb. Sci., 639 (2021), Article 119759, 10.1016/j.memsci.2021.119759

[74] H. Dzinun, M.H.D. Othman, A.F. Ismail, T. Matsuura, M.H. Puteh, M.A. Rahman, J. Jaafar. Stability study of extruded dual layer hollow fibre membranes in a long operation photocatalysis process, Polym. Test., 68 (2018), pp. 53-60, 10.1016/j.polymertesting.2018.03.048

[75] S. Li, X. Zhao, H. Zhang. Aging retardation strategy of PVDF membranes: evaluation of free radical scavenging effect of nano-particles, New J. Chem., 45 (2021), pp. 6108-6119, 10.1039/D0NJ05980C

[76]E. Roubaud, W. Maréchal, O. Lorain, L. Lamaa, L. Peruchon, C. Brochier, J. Mendret, J.-P. Mericq, S. Brosillon, C. Faur, C. Causserand. Understanding aging mechanisms in the context of UV irradiation of a low fouling and self-cleaning PVDF-PVP-TiO2 hollow-fiber membrane, Membranes (basel)., 12 (2022), 10.3390/membranes12050538

Conclusions

Photothermal membranes integrated with advanced nanomaterials represent a groundbreaking solution to address some of the most pressing global challenges related to water resource management and energy sustainability. The research conducted has demonstrated that the incorporation of two-dimensional nanomaterials such as WS_2, NiSe, CoSe, TiO_2, In_2Se_3, and InS can significantly enhance the performance of membrane distillation (MD) and membrane crystallization (MCr) processes. This integration overcomes the limitations of traditional technologies, introducing a new paradigm for water treatment and the recovery of critical resources.

A fundamental aspect of this work has been the improvement of energy efficiency in MD processes through the photothermal nanomaterials' ability to convert solar radiation into heat. Materials such as NiSe and CoSe have proven particularly effective, enabling a significant enhancement in energy performance while simultaneously reducing thermal polarization, one of the principal limitations of existing technologies. These results are particularly relevant for applications in environmentally sensitive contexts, where solar energy can be leveraged as a primary resource.

In the context of strategic resource recovery, membrane crystallization enhanced with WS_2 as a nanofiller has emerged as a highly valuable technology. This material has enabled precise control over the nucleation process, improving selectivity and efficiency in lithium recovery from highly concentrated brines. These findings not only demonstrate the potential of these technologies to meet the demands of the global energy transition but also highlight their contribution to a circular economy model, where resource recovery and valorization are central objectives.

Another noteworthy element of this research is the focus on the sustainability of nanomaterial synthesis. The use of Iris (dimethyl 2-methylglutarate) as a green solvent has represented a significant advancement over traditional methods, enabling the production of high-quality nanosheets with a reduced environmental footprint. This innovative approach aligns with regulatory and environmental requirements and ensures greater compatibility with future industrial applications. The sustainable synthesis of two-dimensional materials thus represents not only a technological opportunity but also a necessity for promoting the transition towards more responsible industrial processes.

In the field of wastewater treatment, photocatalytic membranes enriched with TiO_2 have shown great efficacy in removing complex contaminants such as arsenic and other toxic substances. This outcome underscores the versatility of photothermal membranes, which extend beyond desalination and resource recovery to find applications in more complex environmental contexts,

contributing to the improvement of available water quality.

Overall, this work demonstrates that photothermal membranes constitute a scalable, sustainable, and highly efficient solution to address challenges related to water and energy resource management. The proposed solutions not only overcome the limitations of existing technologies but also open new perspectives for future applications in emerging sectors such as brine management and critical material recovery.

Looking ahead, it will be essential to focus on optimizing membrane fabrication processes to ensure sustainable industrial scalability. Further studies will be necessary to expand the application field of these technologies, exploring new sectors such as energy generation from salinity gradients or advanced treatment of complex industrial effluents. The possibility of combining technological efficiency with environmental sustainability represents a promising pathway for the future of research in this field.

List of publications

- Abramovich S., Dutta D, Rizza C., Santoro S., Aquino M., Cupolillo A., **Occhiuzzi J.**, La Russa M. F., Ghosh B., Farias D., Locatelli A., Boukhvalov D.W., Agarwal A., Curcio E., Bar Sadan M., Politano A. "N*iSe and CoSe Topological Nodal-Line Semimetals: A Sustainable Platform for Efficient Thermoplasmonics and Solar- Driven Photothermal Membrane Distillation*" Small 18(31) - 2201473 (2022) (https://doi.org/10.1002/smll.202201473)

- D'Olimpio G., **Occhiuzzi J. (contributo uguale al primo autore)**, Lozzi L., Ottaviano L., Politano A. "*Dimethyl 2-Methylglutarate (Iris): A Green Platform for Efficient Liquid-Phase Exfoliation of 2D Materials*" Advanced Sustainable Systems 6(11) - 2200277 (2022) (https://doi.org/10.1002/adsu.202200277)

- Santoro S., Aquino M., Rizza C., **Occhiuzzi J.**, Mastrippolito D., D'Olimpio G., Avci A. H., De Santis J.,Paolucci V., Ottaviano L., Lozzi L., Ronen A., Bar-Sadan M., Han D. S., Politano A., Curcio E. "*Lithium recovery through WS2 nanofillers-promoted solar photothermal membrane crystallization of LiCl*" Desalination 546- 116186 (2023) (https://doi.org/10.1016/j.desal.2022.116186)

- **Occhiuzzi J.**, Politano G.G., D'Olimpio G., Politano A. "*The Quest for Green Solvents for the Sustainable Production of Nanosheets of Two-Dimensional (2D) Materials, a Key Issue in the Roadmap for the Ecology Transition in the Flatland*" Molecules, (2023) ,28 (3), 1484 (https://doi.org/10.3390/molecules28031484)

- Santoro S., **Occhiuzzi J.,** Aquino M., Politano A., Straface S., D'Andrea G., Carrillo C., Mallada R., Garcia A., Estay H., Xevgenos D., Argurio P., Curcio E. "*Green photocatalytic mixed matrix membranes for simultaneous arsenic photo-oxidation and water recovery via membrane distillation*" Separation and Purification Technology, (2024) ,342, 127042 (https://doi.org/10.1016/j.seppur.2024.127042)

- Politano A., Al-Juboori R. A., Alnajdi S., Alsaati A., Athanassiou A., Bar-Sadan M., Naderi Beni A., Campi D., Cupolillo A., D'Olimpio G., D'Andrea G., Estay H., Fragouli D., Gurreri L., Ghaffour N., Gilron J., Hilal N., **Occhiuzzi J.**, Roldan Carvajal M., Ronen A., Santoro S., Tedesco M., Tufa R.A., Ulbricht M., Warsinger D.M., Xevgenos D., Zaragoza G., Zhang Y., Zhou M., Curcio E." 2024 roadmap on membrane desalination technology at the water-energy nexus" *J. Phys. Energy,* (2024), **6** 021502 (https://doi.org/10.1088/2515-7655/ad2cf2)

- D'Olimpio G., Boukhvalov D. W., Galstyan V., **Occhiuzzi J.**, Vorochta M., Amati M., Milosz Z., Gregoratti L., Istrate M. C., Kuo C.N., Lue C. S., Ghica C., Comini E., Politano A. "*Unlocking superior NO 2 sensitivity and selectivity: the role of sulfur abstraction in indium sulfide (InS) nanosheet-based sensors*" *J. Mater. Chem. A,* (2024), ***12****, 10329-10340* (https://doi.org/10.1039/d4ta01287a)

Acknowledgements

Tesi redatta con il sostegno finanziario del programma
FSE-REACT-EU, PON "Ricerca e Innovazione" 2014-2020 (D.M. 1061/2021)
Asse IV "Istruzione e ricerca per il recupero – REACT-EU"
Azione IV.5 "Dottorati e Contratti di ricerca su tematiche green"

